

AD-A020 693

SEISMIC WAVE PROPAGATION AND EARTHQUAKE
CHARACTERISTICS IN ASIA

Carl Kisslinger, et al

Cooperative Institute for Research in
Environmental Science

Prepared for:

Air Force Office of Scientific Research

31 October 1975

DISTRIBUTED BY:

NTIS

National Technical Information Service
U. S. DEPARTMENT OF COMMERCE

055025

AFOSR - TR - 76 - 0122

ADA020693

Sponsored by
Advanced Research Projects Agency
ARPA Order No. 1827

Reproduced by
**NATIONAL TECHNICAL
INFORMATION SERVICE**
US Department of Commerce
Springfield, VA. 22151

ARPA Order 1827
Program Code 5F10
Name of Grantee: University of Colorado
Effective Date of Grant: 1 November 1974
Grant Expiration Date: 31 October 1975
Amount of Grant: \$87,486
Grant Number: AFOSR-75-2775
Principal Investigator: Carl Kisslinger (303) 492-7943
Program Manager: William J. Best
Title of Work: Seismic Wave Propagation and Earthquake
Characteristics in Asia

Semi-Annual Technical Report No. 2
1 May 1975 - 31 October 1975
C. Kisslinger, E.R. Engdahl, Ming-te Lin
R. Herrmann, T. Hewitt, G. Lundquist
31 October 1975

DDC
REFORMED
FEB 19 1976
D

AIR FORCE OFFICE OF SCIENTIFIC RESEARCH (AFSC)
DIVISION OF TRANSMITTAL TO DDC
This document has been reviewed and is
being submitted to the AFSC for AFSC 190-12 (7b).
Distribution is unlimited.
A. H. BROWN
Technical Information Officer

UNCLASSIFIED

SECURITY CLASSIFICATION OF THIS PAGE (When Data Entered)

REPORT DOCUMENTATION PAGE		READ INSTRUCTIONS BEFORE COMPLETING FORM
1. REPORT NUMBER AFOSR - TR - 76 - 0122	2. GOVT ACCESSION NO.	3. RECIPIENT'S CATALOG NUMBER
4. TITLE (and Subtitle) SEISMIC WAVE PROPAGATION AND EARTHQUAKE CHARACTERISTICS IN ASIA		5. TYPE OF REPORT & PERIOD COVERED Semi-annual technical report 1 May - 31 October 1975
		6. PERFORMING ORG. REPORT NUMBER
7. AUTHOR(s) C. Kisslinger, E. R. Engdahl, Ming-te Lin, R. Herrmann, T. Hewitt, G. Lundquist		8. CONTRACT OR GRANT NUMBER(s) AFOSR-75-2775
9. PERFORMING ORGANIZATION NAME AND ADDRESS CIRES University of Colorado Boulder, Colorado 80309		10. PROGRAM ELEMENT, PROJECT, TASK AREA & WORK UNIT NUMBERS ARPA Order 1827 Program Code 5F10 Program Element 62701E
11. CONTROLLING OFFICE NAME AND ADDRESS Advanced Research Projects Agency/NMR 1400 Wilson Boulevard Arlington, Virginia 22209		12. REPORT DATE 31 October 1975
14. MONITORING AGENCY NAME & ADDRESS (if different from Controlling Office) Air Force Office of Scientific Research/NP Bolling Air Force Base, Bldg. 410 Washington, D. C. 20332		13. NUMBER OF PAGES 120 126
		15. SECURITY CLASS. (of this report) UNCLASSIFIED
		15a. DECLASSIFICATION/DOWNGRADING SCHEDULE
16. DISTRIBUTION STATEMENT (of this Report) Approved for public release; distribution unlimited		
17. DISTRIBUTION STATEMENT (of the abstract entered in Block 20, if different from Report)		
18. SUPPLEMENTARY NOTES		
19. KEY WORDS (Continue on reverse side if necessary and identify by block number) Plate effects Body-wave synthesis Plate structure Spectral estimation Focal depth Focal mechanisms		
20. ABSTRACT (Continue on reverse side if necessary and identify by block number) The effects of subduction zones on local and teleseismic network data for earthquakes in the North Pacific have been determined. Hypocenter location, focal mechanisms and slip vectors are all perturbed in ways that can be corrected by tracing seismic rays through appropriate models of the upper mantle. The matching of synthetic seismograms for the first 30 seconds of the long period P signal with observations at several azimuths yields depths of crustal events to within 10 km and reliable		

DD FORM 1 JAN 73 1473

EDITION OF 1 NOV 65 IS OBSOLETE

UNCLASSIFIED

SECURITY CLASSIFICATION OF THIS PAGE (When Data Entered)

UNCLASSIFIED

SECURITY CLASSIFICATION OF THIS PAGE (When Data Entered)

20.

estimates of focal mechanisms and source time functions. Spectral estimates for body waves based on the autocorrelation function, with a Hanning window, are more reliable than those by the FFT algorithm. Station spectra can be corrected reasonably well for source crust and receiver crust effects, but the proper way to model attenuation remains a difficult problem. The use of a frequency-dependent modulation of T/Q has been tested and seems promising.

ia

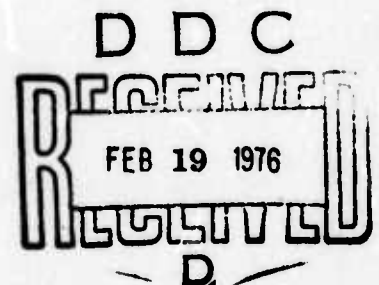
SECURITY CLASSIFICATION OF THIS PAGE (When Data Entered)

TABLE OF CONTENTS

Technical Report Summary	1
1. Plate Effects in North Pacific Subduction Zones	3
2. Focal Depth Determination from the Signal	
Character of Long Period P Waves	40
3. Source Characteristics from Long Period P Wave	
Observations	65
4. Computation of the Source Spectrum from a	
Crustal Earthquake	83
5. Rupture Velocity and Radiation Efficiency	120

ACCESSION for	
NTIS	White Section <input checked="" type="checkbox"/>
DDC	Buff Section <input type="checkbox"/>
UNANNOUNCED	<input type="checkbox"/>
JUSTIFICATION	
BY	
DISTRIBUTION/AVAILABILITY CODES	
Dist.	AVAIL. and/or SPECIAL
A	

ib



Technical Report Summary

1. Seismic ray tracing has been applied to teleseismic and local network data from the North Pacific as a way of examining the effects of subduction zones on seismic waves. The positions of subducting plates can be fixed on the basis of travel-times and amplitudes. Deeper than normal hypocenters fall in the colder, more brittle parts of the plate. The dip and azimuth of focal angles determined with plate effects taken into account are different by large amounts from symmetric earth values. For some distributions of stations with respect to the source, slip vectors derived from focal mechanism solutions may be in error by significant amounts. Solutions for instantaneous relative plate motions based on such data will be adversely affected. Only small changes in the apparent surface velocity and azimuth of the wavefront are predicted for arrays at teleseismic distances.

2. The waveform of long-period teleseismic P waves is shaped by numerous factors, including focal depth, focal mechanism, the source time function, and the earth structure at the source and receiver. The sensitivity to focal depth is so great that it is possible to fix the depth of crustal events to at least 10 km by matching computed and observed waveforms at a number of stations. This resolution capability has been demonstrated for events in continental and oceanic crust in the 30° - 80° range of epicentral distances.

3. In addition to fixing focal depth, the technique of matching long-period P waveforms also yields a best-fitting focal mechanism and a source time function. The technique has been tested on 12 earthquakes. Agreement with focal mechanisms based on standard techniques is very good in almost every case. A source time function shaped as an isocales

triangle gives the best solutions. The method holds promise for discrimination of explosions on the basis of focal mechanism, but the available long-period P signals from moderate explosions in central Asia are insufficient to permit a thorough test.

4. Further studies of the methodology of computing source spectra from digital seismic data have led to the development of a program based on the autocorrelation function that produces more reliable estimates of the spectra than those yielded by the Fast Fourier Transform. Experiments with various data windows have been completed and the Hanning window has been demonstrated to be the best. The way to treat inelastic attenuation, or the proper choice of a Q-model, remains the least understood of the various corrections to observed spectra required by the properties of the real Earth. A modification of the standard practice of taking the ratio of travel-time-to-Q (T/Q) to be a constant is achieved by applying a relaxation mechanism for attenuation, proposed by Solomon. A frequency-dependent modulation of T/Q , with a characteristic relaxation time as a parameter, has been used.

5. A paper, "Rupture Velocity and Indication Efficiency", reporting work partly supported under this grant, has been submitted to the Bulletin of the Seismological Society of America. The abstract is included for part of this report.

1. Plate Effects in North Pacific Subduction Zones

E. R. Engdahl and Ming-Te Lin

Introduction

Since Davies and McKenzie (1969) first documented advances in P residuals, the existence of high-velocity plates in North Pacific subduction zones has been amply demonstrated. In view of the unrealistic assumptions of a spherically symmetric Earth, the existence of a subducted plate beneath an island arc often makes it difficult for geophysicists to study seismic sources in these regions.

Research is now centering on an improved understanding of upper mantle structure and wave propagation effects in subduction zones. The effects of pronounced lateral heterogeneity in physical properties on the seismic signal have been discussed by numerous authors (Jacob, 1972; Davies and Julian, 1972; Sleep, 1973; Toksöz et al., 1971). The spatial distribution of intermediate depth earthquakes within slabs of lithosphere which descend into the mantle is important to our understanding of the subduction process. Engdahl (1973, 1974) considered plate effects on earthquake hypocenters by allowing for plate structure in the location process rather than assuming that the Earth is laterally homogeneous. Because of refraction effects the point on the focal sphere corresponding to the ray to a seismograph station will be plotted in the wrong place if that ray has gone through a high velocity subducted slab, but a spherical Earth model is used to determine the ray path. The size of the effect may depend on the source-slab-station system.

In this paper we are concerned with effects of crust and upper mantle structure on all aspects of the interpretation of seismic data (travel times and slownesses, hypocenter locations, wave amplitudes, and focal mechanisms). We begin with thermal models and construct velocity models of North Pacific subduction zones. We apply seismic ray

tracing to study the effects of these models. To provide constraint on the analysis of focal parameters and focal mechanism solutions we only use data from regions having good local seismograph networks. Finally, we demonstrate how these new data enable us to better interpret the subduction process.

Velocity Models

Numerical thermal models of slabs (Toksöz et al., 1973) were calculated for kinematic parameters relevant to the Kuril, Aleutian and Alaska subduction zones. Velocity models were constructed from the thermal models using a linear relation between velocity and temperature perturbation (eqn. 1: Sleep, 1973) and the Herrin et al. (1968) velocities as the unperturbed base model. A thermal coefficient of seismic velocity of 9×10^{-4} km/sec°C seemed to give velocity contrasts in each region consistent with published values for the Aleutians (Jacob, 1972; Sleep, 1973) and for the Tonga-Fiji region (Mitronovas and Isacks, 1971). We purposely used a base model without a low velocity zone or gradients due to phase changes to simplify the ray tracing and because these complications were not warranted by the problem. The resulting velocity models shown in subsequent figures are characterized by high velocities in the upper half of the plate, on the average 8 - 10% higher than the surrounding mantle, corresponding to the cooler temperatures of the thermal models.

The location of each plate is given by the distance of some point on the model to the center of curvature of the subduction zone. This allows us to project a two-dimensional model into three dimensions by assuming symmetry along the arc about the center of curvature. The radius and center of curvature are determined by a least squares fit to the trench axis or to the volcanic arc. Parameters fitted to the trench axis of the Kurils and of the central Aleutians and to the volcanic arc in Alaska are given in Table I. All sections shown in this paper are projections with respect to the distance to the center of curvature. The exact location of the reference point on the plate model is not uniquely determined, however, but has to be estimated from observed travel

times and amplitudes (Jacob, 1972; Sleep, 1973). A good first guess is that the Benioff zone defined by conventional hypocenters falls in the higher velocity colder portion of the plate at a depth of 100-125 km beneath the volcanic arc (Engdahl, 1973).

Seismic Ray Tracing

The problem of ray tracing in a generally heterogeneous medium has been treated using the calculus of variations and Fermat's principle of stationary time (Julian, 1970). The solution in geocentric spherical polar coordinates is a system of first-order differential equations giving the variation with time of the position (r , θ , Q) of a point on a ray and the direction of propagation (i = incident angle, α = azimuth) from the point in terms of the wave speed (v) and its spatial derivatives in the medium. Julian has developed a computer program to treat this generalized formulation and this program forms the basis for the calculations presented in this paper. Only the size of computer core limits the detail to which v can be represented in the model. To study subduction zones it is convenient to represent the structure by a two-dimensional grid, normal to the arc, in which velocities are specified at discrete points. With this representation any degree of structural complexity may be defined subject only to the grid interval. The wave speed and its derivatives may then be determined numerically at any point within the structure using cubic spline interpolation. In practice, time steps are chosen so that, as the ray propagates, the interpolation grids along the ray overlap. The grid size is also chosen to be about the same order as the wavelength of observed data. The velocity models shown in Figures 2, 5 and 9 are represented by grids at 10 km depth intervals and 10, 12.8 and 15.07 km surface distance intervals to the centers of curvature, respectively.

The next step is to incorporate the plate model in the hypocenter determination, using seismic ray tracing in the manner described by Engdahl (1973). This method differs from the conventional formulation only in that the coefficients of the station condition equations are now

explicitly known from the ray vectors to each station from the source.

The problem of finding that particular ray that arrives at a given station is formidable, however, and is now done by iteratively shooting rays until we find one closer than 1 km to the desired end point. The wavefront of that ray is then propagated the small distance remaining.

Data

To reduce computational expense the events studied in each subduction zone were relocated using local stations and a fixed teleseismic network of WWSSN and selected Russian and Canadian stations. P onsets, first motions and amplitudes were read from 70 mm film copies of the records of WWSSN stations. Data for local stations in the Kurils were taken from bulletins; data from the Amchitka network (Engdahl, 1973) were read from Develocorder film and tape playbacks; and data from the USGS Alaskan network were kindly provided by John Lahr.

Station corrections developed by Sengupta and Julian (1976) from a world-wide distribution of deep focus events were applied to those arrivals beyond 30° distance. Focal mechanisms were determined from long period P-wave first motions on WWSSN records whenever possible and from short-period first motions at other key stations.

Kuril Islands

Eleven earthquakes, large enough to be well recorded on long-period WWSSN instruments, were chosen for special study in the Kuril Islands (Table II). These events are distributed along the arc and with depth (Figures 1 and 2) to insure a good sampling of the structure. Several closely-located very deep events were used in the hope of determining station corrections appropriate to the Kurils. This was not possible with so few events because the residuals did not appear to be slowly varying functions of the spatial coordinates. This phenomena has also been reported by Engdahl (1975) for deep focus Fiji-Tonga events.

Nine of the events were relocated, in the manner previously described, using seismic ray tracing, and a long slab model of the Kurils (Figure 2). The position of the model was fixed by locating the volcanic arc at C. The two shallow events in the left hand corner of Figure 2 were not relocated but were selected for a special study of plate effects on slip vector determinations to be discussed in a later section.

The model is undoubtedly a gross oversimplification of the overall arc structure but is useful in examining plate effects on P-wave residuals, slownesses, focal mechanism determinations and long-period amplitudes. In addition, seismic ray tracing allows local, regional and teleseismic data to be used jointly without the disadvantage of huge biases produced by ray paths travelling primarily in the high velocity plate, especially to local stations (Mitronovas and Isacks, 1971).

For the deepest events in this set, travel time advances of up to 7 sec to stations along the arc are observed. Travel times to teleseismic stations from intermediate depth events were commonly decreased by up to 3 sec. The joint effect on location, compared to symmetric earth calculations is to shift the hypocenters to the northwest and deeper.

Only small changes of up to 0.05 sec/deg in slowness and 0.5° in azimuth of the wavefront are predicted for arrays at teleseismic distances ($> 30^\circ$).

Plate structure may also severely effect the apparent location of a ray leaving the focus and, hence, in some instances produce significant changes in focal mechanism determinations. Focal angles for the nine relocated events were found to differ from symmetric earth values by up to 20° in take-off angle and 35° in azimuth for teleseisms. Focal mechanisms were determined for all the relocated hypocenters using only traced rays. All but two of these events were also studied by Stauder and Mualchin (1975) using long-period P waves and S wave polarization angles with a symmetric earth model. The traced solutions have nodal planes that generally conform to those of Stauder and Mualchin but with small departures in dip and strike of up to 5° and 10° , respectively.

Although we have calculated the details of the velocity distribution from thermal contours, the plate is still not uniquely located in the Earth. Sleep (1973) has shown that in the case of the LONGSHOT explosion in the Central Aleutians the amplitudes are particularly sensitive to plate position. We have chosen position C in Figure 2 for our starting model since this gives a depth to the Benioff zone beneath the volcanic arc of roughly 125 km as suggested by Engdahl (1973). We use essentially the same technique as Sleep (1973) to examine the amplitude of the first peak-to-peak motion recorded on long-period WWSSN instruments from nine of the Kuril events. This technique requires correcting observed amplitudes for the source mechanism determined from traced rays and for epicentral distance. Source corrections for rays near nodal planes were restricted to a maximum factor of 20. A combined station and distance correction was

obtained by using the deepest event on 30 Aug 1970 to correct the relative amplitudes of other events. In this way we hoped to isolate the purely plate effects. Periods of first arrivals were also measured and the amplitudes corrected for instrument response.

Station corrected relative long-period amplitudes given on a \log_2 scale for a Kuril event at a depth of 114 km are plotted on an equidistant azimuthal projection about the focus in Figure 3. To demonstrate the distortion of ray paths for plate positions A-D, rays corresponding to 10° distance and 30° azimuth increments on a symmetric earth were traced through the plate model and also plotted in the same projection about the focus. For a symmetric earth or a very deep earthquake, this ray density pattern would be equi-spaced concentric circles and radial. This plot is useful in a qualitative way since closely spaced lines suggest higher amplitudes while large open areas suggest shadow zones.

A large shadow zone to the northwest is predicted for this event for all plate positions. An analytical solution for wave propagation in a one-dimensional slab predicts that long-period seismograms in the ray-theoretical shadow zone will typically have amplitudes 50% (or greater) of the direct P-wave amplitude and exhibit wave form broadening (Ward and Aki, 1975). The results plotted in Figure 3 suggest a long-period amplitude reduction by at least a factor of 2. There also appeared to be no consistent pattern of wave form broadening in the period measurements, due in part to the fact that there are unknown frequency dependent effects beneath stations. A disappointing result in this study is that for all these events the long-period amplitude ray density pattern is not sensitive enough to plate position for intermediate depth events.

Central Aleutians

Thirty-nine intermediate depth earthquakes of magnitude 4 or greater were selected for special study in the Central Aleutians. The distribution of these earthquakes and the local seismograph network are shown in Figure 4. Events less than about 125 km in depth are uniformly distributed along the arc. Deeper earthquakes are clustered behind an active volcano (Gemisopohnoi) along an extension of Bowers Ridge, a large arcuate aseismic structure extending into the Bering Sea.

The seven events indicated by the solid circles in Figure 4 and listed in Table II were also detected teleseismically. In Figure 5 is shown a velocity model of the Aleutian slab constructed from thermal contours. The position of this model is well constrained by numerous seismic travel-time residuals from the LONGSHOT explosion (Jacob, 1972; Sleep, 1973) and by associated amplitude anomalies (Sleep, 1973). This slab model was used to relocate six of the teleseismic events, shown in section in Figure 5, using seismic ray tracing. The shallow event was not relocated, but is the location of the 1965 Rat Islands mainshock. The result confirms an earlier conclusion by Engdahl (1973), using a more simplified slab model, that the Benioff zone at depth is comparatively thin and corresponds closely to the colder, more brittle region of the slab suggested by thermal models.

Figure 6 is a section showing 39 events that have been relocated using the same model and seismic ray tracing but only with data from the local network. The solid circles are the new locations of the same teleseismic events shown in Figure 5. The relocated hypocenters define a thin zone in the upper half of the plate corresponding to the region of largest velocity (or thermal) gradient. The thinness of this seismic

zone we believe to be model independent. The relative location within the model, however, is probably not well determined since little is known about the details of upper mantle structure in the wedge traversed by rays to the local network.

With these the best estimates of our local Aleutian events we can now hope to obtain more consistent composite focal mechanisms determinations. If intermediate depth earthquakes occur in the colder more brittle region of the slab, we would expect focal mechanism solutions to suggest that the descending lithosphere acts as a stress guide that aligns the earthquake generating stresses along the dip of the slab (Isacks and Molnar, 1971). Figure 7 shows two classes of mechanisms obtained in the Central Aleutians. Intermediate events from about 70 to 127 km in depth are uniformly characterized by down-dip pressure axes or lateral extension along the strike of the arc. Among the deeper events there is a large subset that appear to have near vertical tension axes. The sense and location of this change in focal mechanism is very similar to the results of Stauder and Mualchin (1975) in the Kuril Islands. They found that intermediate depth foci separate into those which represent an axial compression with respect to the plate at depths less than 120-140 km and those which represent an axial tension at greater depths. Three previously published solutions for deeper than normal events in the Aleutians (Stauder, 1968; Isacks and Molnar, 1971) led Isacks and Molnar to conclude that axial tension was the operative stress down the Aleutian slab. These events are exceptions to the results of this paper which suggest that the slab is under compression not tension. This would occur if the subduction rate is faster than the rate at which the lithosphere is sinking (Isacks and Molnar, 1971; Smith and Toksöz, 1972).

Alaska

The USGS southern Alaska seismograph data provide excellent data for resolving the configuration of the Benioff zone in the vicinity of Cook Inlet (Figure 8). Lahr et al. (1974) find an apparent thickness of the dipping seismic zone of only about 15 km when projected for 300 km along strike. Seven large events, well recorded on the local network and teleseismically, were selected for relocation (Table II). We located the plate by placing the Benioff zone at a depth of 115 km beneath the volcanic arc. The plate model differs from those previously studied in that the seaward extension is characterized by a long gentle slope (Figure 9). The relocated hypocenters and the 1964 Alaska mainshock are shown in section with the model in Figure 9. At least two events appear to be located at the top of the slab. It is difficult to interpret these results since the relocated hypocenters may reflect the effect of upper mantle structure on the preponderance of local arrivals and the possible mislocation of the slab. Further study of these data will be necessary.

Slip Vectors

It has been shown in this paper and elsewhere (Toksöz et al., 1971) that the structure of subducted plates bends rays leaving island-arc earthquakes and distorts the fault-plane solution inferred from first motions. Hence, under certain circumstances of station geometry with respect to the seismic source, the strike of either one or both of the nodal planes determined with a symmetric Earth model may be significantly in error in the presence of a subducted plate. In some arcs a systematic error in the slip vectors may be introduced, producing some difficulty in modelling relative plate motions (Minster et al., 1974). We have chosen five North Pacific events, corresponding to overthrusting of the island block relative to the oceanic block, for a special study of this effect. This includes two Kuril events (Stauder and Bollinger, 1966b), the Rat Islands mainstock (Stauder, 1968a) and the 1964 Alaska earthquake (Stauder and Bollinger, 1966a). The focal parameters for these events are listed in Table II and their location in section shown in Figures 2, 5 and 9.

The original P-wave first motion data and nodal planes published by Stauder for these thrust earthquakes are plotted, using the Herrin et al. (1968) symmetric Earth model, on equal-area azimuthal projections of the lower hemisphere in the left hand column of Figures 10 and 11. The same rays were traced through the appropriate plate structures and the new ray projections plotted with the original nodal planes in the second column of these figures. The third column shows the ray distortion produced by the plate for each event in the manner previously described.

For the two Kurile events there is characteristically one nodal plane dipping steeply to the southeast which seems to be well determined by the first motion data and is little effected by plate structure. The

second nodal plane is not so well defined but is constrained to dip gently to the northwest by S wave polarization angles. Stauder and Maulchin (1975) found in many instances that the S polarization lines do not converge well to the T axis but seem to indicate an axis with a plunge some 5 to 10° steeper than the one which bisects the dihedral angle between the two nodal planes. This is exactly the kind of deflection we see in Figure 10 for rays to stations northwest of the source. Since the T axis of their solutions is still consistent with the nodal planes we conclude that their published estimates will not be greatly changed by plate structure and that faulting characteristic of normal depth earthquakes in the Kurils is consistent with the stated convergence of the oceanic plate in the direction N55°W with respect to the continental plate.

For the Rat Islands mainshock shown at the top of Figure 11 introduction of plate structure has produced changes in the focal angles of up to 8° in dip and 22° in azimuth to some stations. The largest changes occur for rays departing nearly along the strike of the arc. Ray projections to North America appear to have undergone a net outward shift and counter-clockwise rotation, as these rays seek the higher velocity path through the plate. Ordinarily, these changes might not affect the location of the nodal planes, as in the case of intermediate depth earthquakes in the central Aleutians (Engdahl, 1974). In this particular case, however, the strike of the auxiliary plane is highly dependent on stations to North America (NE quadrant). An auxiliary plane with a 15° change in dip direction would fit the data equally well and illustrates the potential danger. The slip vector could undergo a corresponding rotation from N39°W to N54°W. The 1964 Alaska earthquake shown in the bottom of this figure occurs too far south of the deep plate structure in Alaska for rays to sense the velocity anomaly, so that the focal mechanism remains well determined.

These results have important consequences for the modelling of relative plate motions. Because of the similarity in source-station geometry along the whole of the Aleutian arc, we could expect to have the same discrepancy in other solutions published by Stauder. Minster et al. (1974) relied entirely on North Pacific data to propose the existence of a Bering Plate, moving with respect to North America. Traditionally, the lithosphere north of the Aleutian arc has been considered part of the North American plate (McKenzie and Parker, 1967).

The Bering plate was introduced by Minster et al. because of a systematic misfit to the slip vectors of earthquakes along the Aleutian and Kurile arc for a pole (NOAM-PCFC) determined by assuming the lithosphere north of the Aleutian arc as part of the North American plate. The Alaska earthquake, the least effected by slab structure, does not agree with the BERI-PCFC pole and would agree better with the NOAM-PCFC pole. The Aleutian earthquakes had misfits to the slip vectors of the same magnitude and direction of the changes in the slip vector shown for the Rat Islands earthquake. The two Kuril earthquakes used were less than the characteristic slip vector for the Kuriles (N55°W) and in the direction of the misfit. Since the data do not overwhelmingly support the existence of a Bering plot, we must conclude that there is still considerable uncertainty in the need for a Bering plate in the modelling of relative plate motions in the North Pacific.

Discussion

The relocated hypocenters plotted in preceding figures are partly model dependent, but represent at least a first order improvement in absolute location over previous studies in which plate effects have not been accounted for. In the Aleutians, for example, source bias due to plate structure may be expected to produce serious errors, of up to 0.5 degree in teleseismic epicenter determinations (Herrin and Taggart, 1968). In Alaska, Lahr et al. (1974) found using only local data systematic shifts in epicenters of up to 25 km in distance and 10 km in depth, the location bias increasing with depth. Clearly, if we are to use seismicity to study mechanical processes within subducted plates, we must have a better understanding of where the earthquakes are actually occurring.

Conventional hypocenter locations in the Tonga Island arc (Skyes et al., 1969; Mitronovas et al., 1969) suggest an upper limit to the thickness of the seismic zone of about 25 km, but considering errors of location it could be even thinner. Wyss (1973) reports from the same dimensions of large intermediate depth earthquakes in the Tonga region, that the thickness of the seismic zone is more nearly 11 km. Lahr et al. (1974) used data from the southern Alaska seismograph network (Figure 8) to estimate an apparent thickness of the Benioff zone of about 15 km when projected for 300 km along strike. Subdivision of the zone into segments extending 50 km along strike indicates that in many areas earthquakes are concentrated within a zone less than 5 km thick. Billington and Isacks (1975) used the method of Joint Hypocenter Determination to relocate 500 to 600 depth earthquakes in the northern part of the Tonga arc. They found evidence for fault planes within the relatively thick lithospheric slab. This study lends further support to this evidence for interior

deformation in subducted plates. A remaining uncertainty is the question of lateral variation of slab properties or for tearing at depth (Isacks and Molnar, 1971; Abe, 1972). The answer to this question is being sought in a very detailed study of Central Aleutian earthquakes now in progress.

Intermediate depth foci in the Kurils are characterized by two properties (Stauder and Maulchin, 1976): 1) the principal axis system corresponding to the focal mechanisms all have the B axis nearly horizontal and lying parallel to (i.e. within) the Benioff zone, and 2) one of the other two axes, either the P or T axis is aligned down dip to the descending plate. For foci above 120 km the earthquakes are down dip compression and for foci deeper than 140 km down dip tension. From 120-140 km in depth both types of foci are found in close spatial relationship. Veith (1974) has suggested that this sharp zoning may be associated with the depth at which the olivine-spinel phase transition occurs within the interior of the descending plate. He suggests that the volume change associated with phase transition could result in down-dip tensional stress reaching a critical value within the interior of the subducted plate while down-dip compressional stress could equally reach critical values across the phase transition boundary, near the outer surface of the plate. The region of olivine-spinel phase transition is usually estimated to be 250 km (Turcotte and Schubert, 1971) to 300 km (Ringwood, 1972). One or more other phase changes, such as basalt to eclogite and pyrolite to garnet pyrolite are more likely to take place in the upper 200 km of the mantle and these phase boundaries may be marked by complications of the low velocity zone. These phase changes were not included in the thermal models calculated in this paper because the heating from this reaction was insignificant (Sleep, 1972).

References

- Abe, K., 1972. Seismological evidence for a lithospheric tearing beneath the Aleutian arc. *Earth Planet. Sci. Letters*, 14: 428-432.
- Billington, S. and Isacks, B. L., 1975. Identifications of fault planes associated with deep earthquakes. *Geophys. Res. Let.*, 2: 63-66.
- Davies, O. and Julian, B. R., 1972. A study of short period P-wave signals from Longshot. *Geophys. J. Roy. astr. Soc.*, 29: 185-202.
- Davies, D. and McKenzie, D. P., 1969. Seismic travel-time residuals and plates. *Geophys. J. Roy. astr. Soc.*, 18: 51-63.
- Engdahl, E. R., 1974. Effects of island arc plate structure on earthquake hypocenters and focal mechanisms (abstract). *Trans. Am. geophys. Un.*, 55: 348-349.
- Engdahl, E. R., 1973. Relocation of intermediate depth earthquakes in the Central Aleutians by seismic ray tracing. *Nature, Phys. Sci.*, 245: 23-25.
- Engdahl, E. R., 1975. Effects of plate structure and dilatancy on relative teleseismic P-wave residuals. *Geophys. Res. Let.*, (in press).
- Herrin, E. (ed.), Arnold, E. P., Bolt, B. A., Clawson, G. E., Engdahl, E. R., Freedman, H. W., Gordon, D. W., Hales, A. L., Lohdell, J. L., Nuttli, O., Romney, C., Taggart, J. and Tucker, W., 1968. 1968 Seismological Tables for P Phases. *Bull. seism. Soc. Am.*, 58: 1193-1352.
- Herrin, E. and Taggart, J., 1968. Source bias in epicenter determinations. *Bull. seism. Soc. Am.*, 58: 1791-1796.
- Isacks, B. and Molnar, P., 1971. Distribution of stresses in the descending lithosphere from a global survey of focal mechanism solutions of mantle earthquakes. *Rev. Geophys. Space Phys.*, 9: 103-174.

- Jacob, K. H., 1972. Global tectonic implications of anomalous seismic P travel times from the nuclear explosion Longshot. *J. Geophys. Res.*, 77: 2556-2573.
- Julian, B. R., 1970. Ray tracing in arbitrarily heterogeneous media. Lincoln Lab. Tech. Note 1970-45.
- McKenzie, D. P. and Parker, R. L., 1967. The North Pacific: An example of tectonics on a sphere. *Nature*, 216: 1276-1280.
- Lahr, J. C., Engdahl, E. R. and Page, R. A., 1974. Locations and focal mechanisms of intermediate depth earthquakes below Cook Inlet (abstract). *Trans. Am. geophys. Un.*, 55: 349.
- Minster, J. B., Jordan, T. H., Molnar, P. and Haines, E., 1974. Numerical modelling of instantaneous plate tectonics. *Geophys. J. Roy. astr. Soc.*, 36: 541-576.
- Mitronovas, W. and Isacks, B., 1971. Seismic velocity anomalies in the upper mantle beneath the Tonga-Kermadec island arc. *J. Geophys. Res.*, 76: 7154-7180.
- Mitronovas, W., Isacks, B. and Seeber, L., 1969. Earthquake locations and seismic wave propagation in the upper 250 km of the Tonga Island arc. *Bull. seism. Soc. Am.*, 59: 1115-1135.
- Ringwood, A. E., 1972. Phase transformations and mantle dynamics. *Earth Planet. Sci. Letters.*, 14: 233-241.
- Sengupta, M. K. and Julian, B. R., 1976. P wave travel times from deep earthquakes. *Bull. seism. Soc. Am.*, submitted for publication.
- Sleep, N. H., 1975. Stress and flow beneath island arcs. *Geophys. J. Roy. astr. Soc.*, 43:
- Sleep, N. H., 1973. Teleseismic P-wave transmission through slabs. *Bull. seism. Soc. Am.*, 63: 1349-1373.

- Sleep, N., 1972. Deep structure and geophysical processes beneath island arcs. *Ph.D. Thesis*, Massachusetts Institute of Technology, Cambridge, Massachusetts, 274 pp.
- Smith, A. and Toksöz, M., 1972. Stress distribution beneath island arcs. *Geophys. J. Roy. astr. Soc.*, 29: 289-318.
- Stauder, W. and Mualchin, L., 1975. Fault motion in the larger earthquakes of the Kurile-Kamchatka arc and of the Kurile-Hokkaido corner. *J. Geophys. Res.*, (in press).
- Stauder, W., 1968a. Mechanism of the Rat Island earthquake sequence of February 4, 1965, with relation to island arcs and sea-floor spreading. *J. Geophys. Res.*, 73: 3847-3858.
- Stauder, W., 1968b. Tensional character of earthquake foci beneath the Aleutian trench and relation to sea-floor spreading. *J. Geophys. Res.*, 73: 7693-7702.
- Stauder, W. and Bollinger, G. A., 1966a. The focal mechanism of the Alaska earthquake and its aftershocks. *J. Geophys. Res.*, 71: 5283-5293.
- Stauder, W. and Bollinger, G. B., 1966b. The S-wave project for focal mechanism studies, earthquakes of 1963. *Bull. seism. Soc. Am.*, 56: 1363-1373.
- Sykes, L. R., Isacks, B. and Oliver, J., 1969. Spatial distribution of deep and shallow earthquakes of small magnitudes in the Fiji-Tonga region. *Bull. seism. Soc. Am.*, 59: 1093-1113.
- Toksöz, M., Sleep, N. and Smith, A., 1973. Evolution of the downgoing lithosphere and the mechanisms of deep focus earthquakes. *Geophys. J. Roy. astr. Soc.*, 35: 285-310.
- Toksöz, M., Minear, J. and Julian, B. R., 1971. Temperature field and geophysical effects of a downgoing slab. *J. Geophys. Res.*, 76: 1113-1138.

- Tucotte, D. L. and Schubert, G., 1971. Structure of the olivine-spinel phase boundary in the descending lithosphere. *J. Geophys. Res.*, 76: 7980-7987.
- Veith, K. F., 1974. The relationship of island arc seismicity to plate tectonics (abstract). *Trans. Am. geophys. Un.*, 55: 349.
- Ward, R. W. and Aki, K., 1975. Synthesis of teleseismic P-waves from sources near sinking lithospheric slabs. *J. Geophys. Res.*, (in press).
- Wyss, M., 1973. The thickness of deep seismic zones. *Nature*, 242: 255-256.

TABLE I

ARC PARAMETERS

CURVATURE

	CURVATURE		REFERENCE	
	Center	Radius (deg)	Location	Radius (deg) Ident.
Kuril	58.243N 127.993E	19.9 (trench)	49.358N 154.708E	18.004 Krenitzky Volcano
Aleutian	58.392N 178.565W	8.1 (trench)	51.438N 179.182E	7.089 LONGSHOT
Alaska	8.379N 102.392E	90.0 (volcanic arc)	60.487N 152.732W	90.000 Redoubt Volcano

TABLE II
EARTHQUAKES STUDIED

<u>Relocated</u>	Date	Origin Time	Latitude	Longitude	Depth	Magnitude
	d m y	GMT	(deg)	(deg)	(km)	
Kuril	25 07 68	10 50 37.34	45.590N	146.890E	31.0	5.9
	30 03 70	17 46 11.60	52.343	151.606E	661.4	6.6
	05 09 70	07 52 30.34	52.195	151.497E	589.1	5.7
	29 01 71	21 58 06.64	51.640	151.054E	542.3	6.1
	24 11 71	19 35 32.75	52.757	159.371E	114.3	6.3
	22 03 72	10 27 46.64	48.936	153.841E	145.0	6.3
	27 05 72	04 06 54.48	54.954	156.366E	429.1	5.7
	26 06 72	10 06 03.20	51.761	156.317E	190.6	5.6
	21 08 72	06 23 51.34	49.468	147.074E	590.3	5.9
	18 09 71	02 12 41.35	51.887	178.660E	104.6	4.5
Aleutian	06 10 71	11 37 57.33	52.010	178.196E	137.5	4.9
	13 10 71	14 01 49.23	51.651	179.629W	89.9	5.3
	06 12 71	11 04 47.16	52.096	179.748E	168.7	5.0
	08 12 71	13 00 16.76	51.566	178.388E	70.2	5.2
	31 12 71	19 57 21.00	51.612	179.992W	98.8	5.4
	13 02 72	22 40 18.87	59.859	154.339W	158.9	4.8
	02 04 72	13 08 20.71	60.005	153.647W	120.5	4.9
	07 04 72	03 16 25.48	60.031	152.702W	95.6	4.9
	14 06 72	00 52 37.65	60.386	153.473W	142.8	5.0
	18 12 72	02 53 46.40	60.771	153.320W	161.0	5.0
Alaska	18 05 73	18 32 58.47	63.082	150.976W	120.4	4.7
	20 05 73	18 18 20.10	60.875	152.484W	107.8	4.9
For Slip Vectors						
Kuril	28 06 63	21 55 39.0	46.50	153.20E	33	6.7
	20 10 63	00 53 07.0	44.70	150.70E	25	7.5
Aleutian	07 02 65	09 25 51.0	51.40	179.10E	30	7.5
	30 03 64	03 36 12.7	61.05	147.50W	20	8.5

Figure Captions

- Figure 1.1: Kuril Islands earthquakes. In this and subsequent figures circles are earthquakes and triangles are seismograph stations. Bathymetry is in fathoms (1 fathom = 1.83 meters).
- Figure 1.2: Velocity model of Kurils constructed from thermal anomalies with volcanic arc located at position C. Hypocenters and model are projected as surface distance to the center of curvature of the arc.
- Figure 1.3: Station-corrected amplitudes on a \log_2 scale for Kuril event at a depth of 114 km. Projection is equi-distant azimuthal. Lines correspond to rays at 10° distance and 30° azimuth increments on a symmetric earth that have been traced through the plate model for positions A - D.
- Figure 1.4: Central Aleutian earthquakes located using only local data and plate model shown in Figure 5.
- Figure 1.5: Central Aleutian earthquakes located using both local and teleseismic data and plate model shown. Dashed line is hypothetical plate outline.
- Figure 1.6: Central Aleutian earthquakes located using only local data and plate model shown.
- Figure 1.7: Composite focal mechanisms for earthquakes at depths indicated. Projection is equal-area azimuthal on lower hemisphere. P and T refer to pressure and tension axes, respectively.
- Figure 1.8: Alaska earthquakes and local seismograph network.
- Figure 1.9: Alaska earthquakes located using plate model shown.

Figure 1.10: Kuril shallow earthquakes demonstrating effects of plate structure on focal mechanism determinations.

Figure 1.11: 1965 Rat Islands and 1964 Alaskan mainshocks and plate effects on focal mechanism determinations.

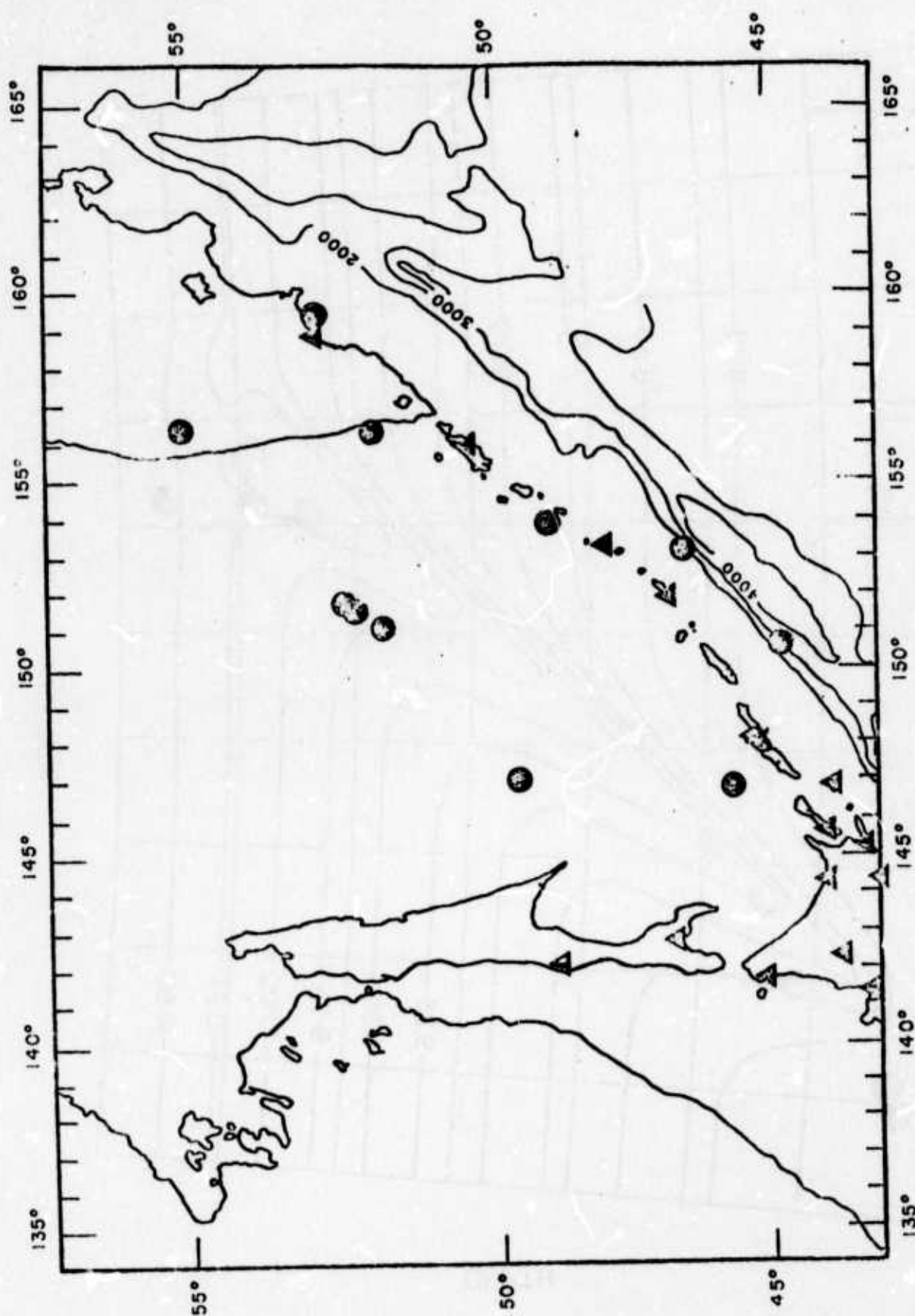


Figure 1.1

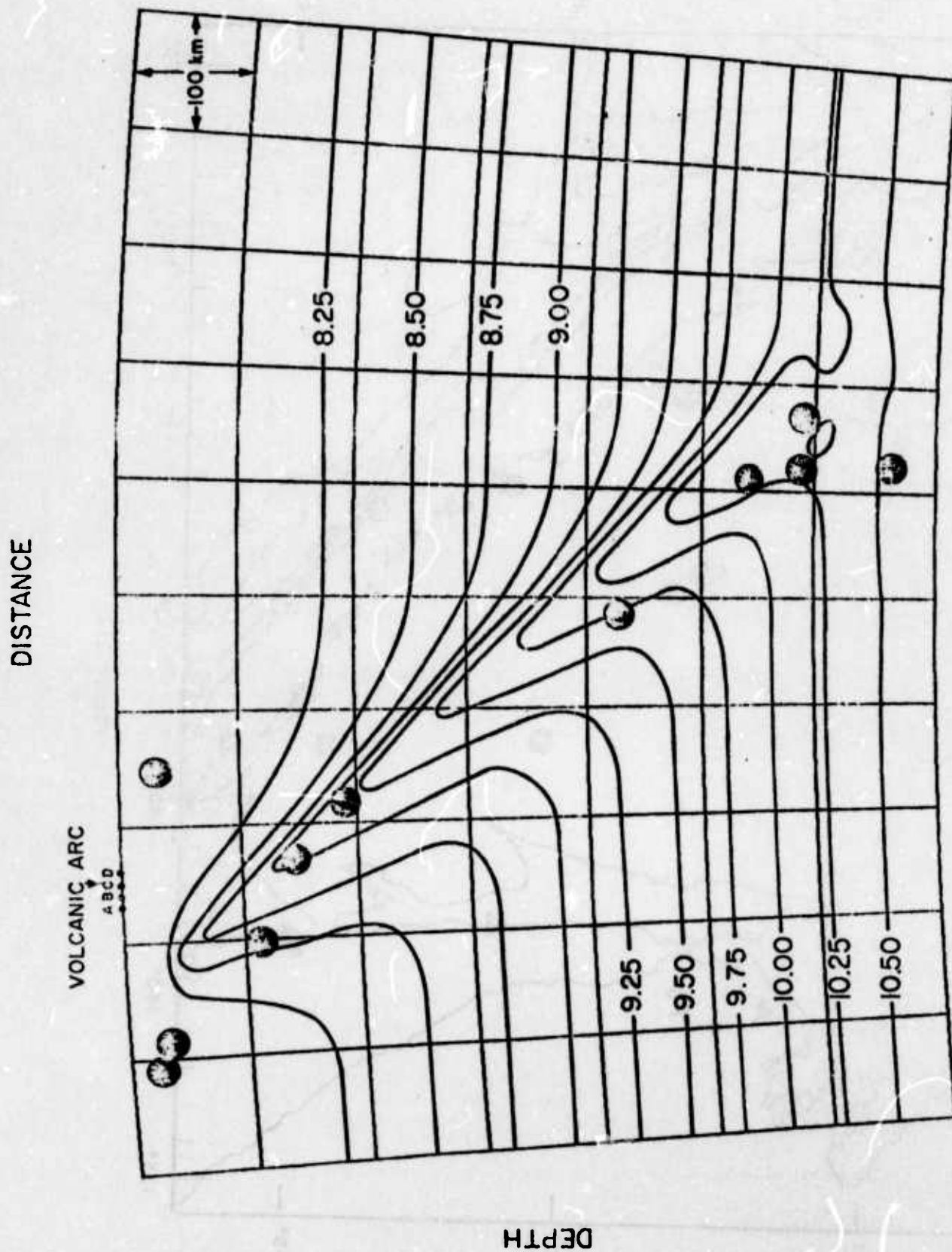


Figure 1.2

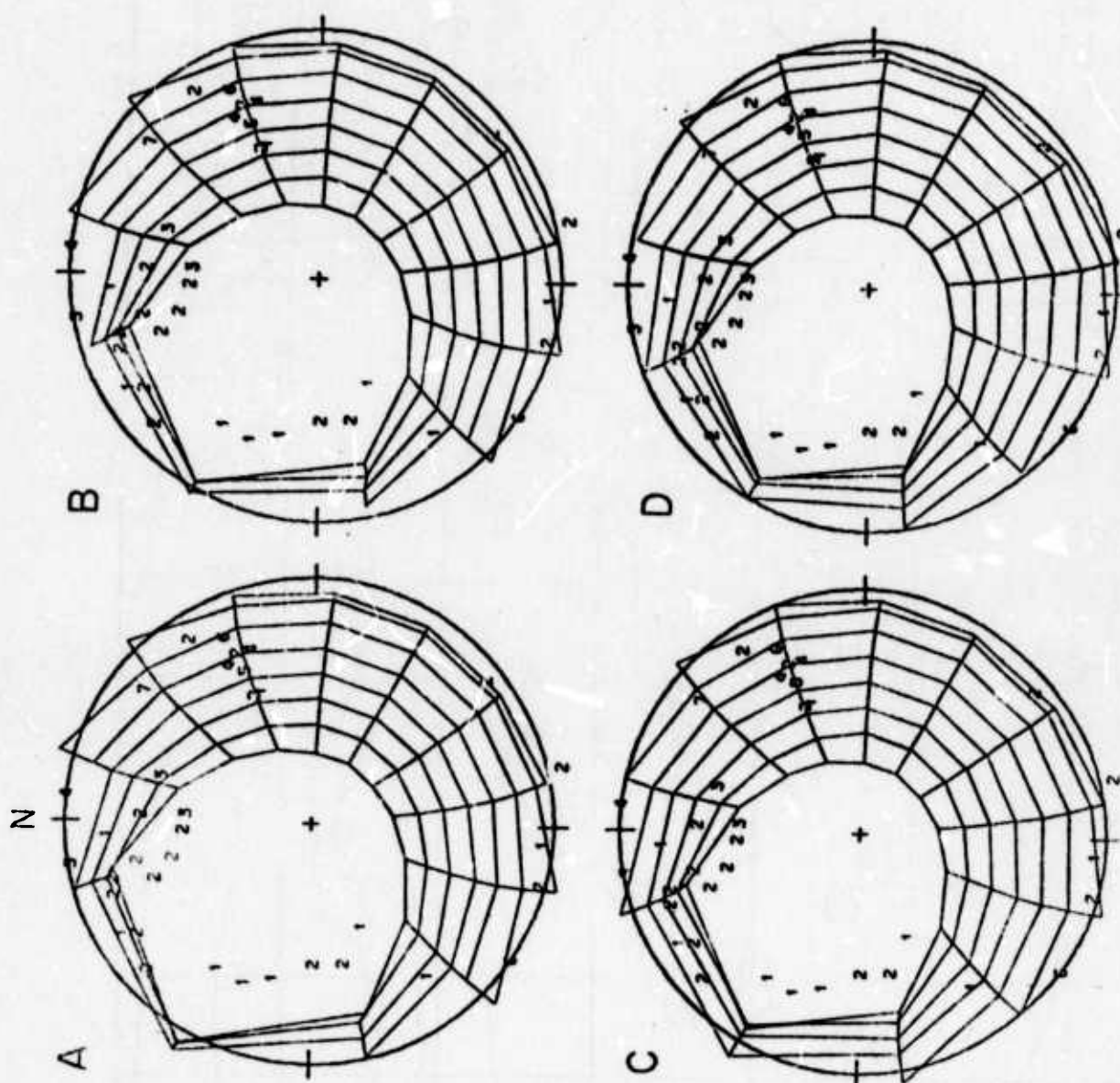


Figure 1.3

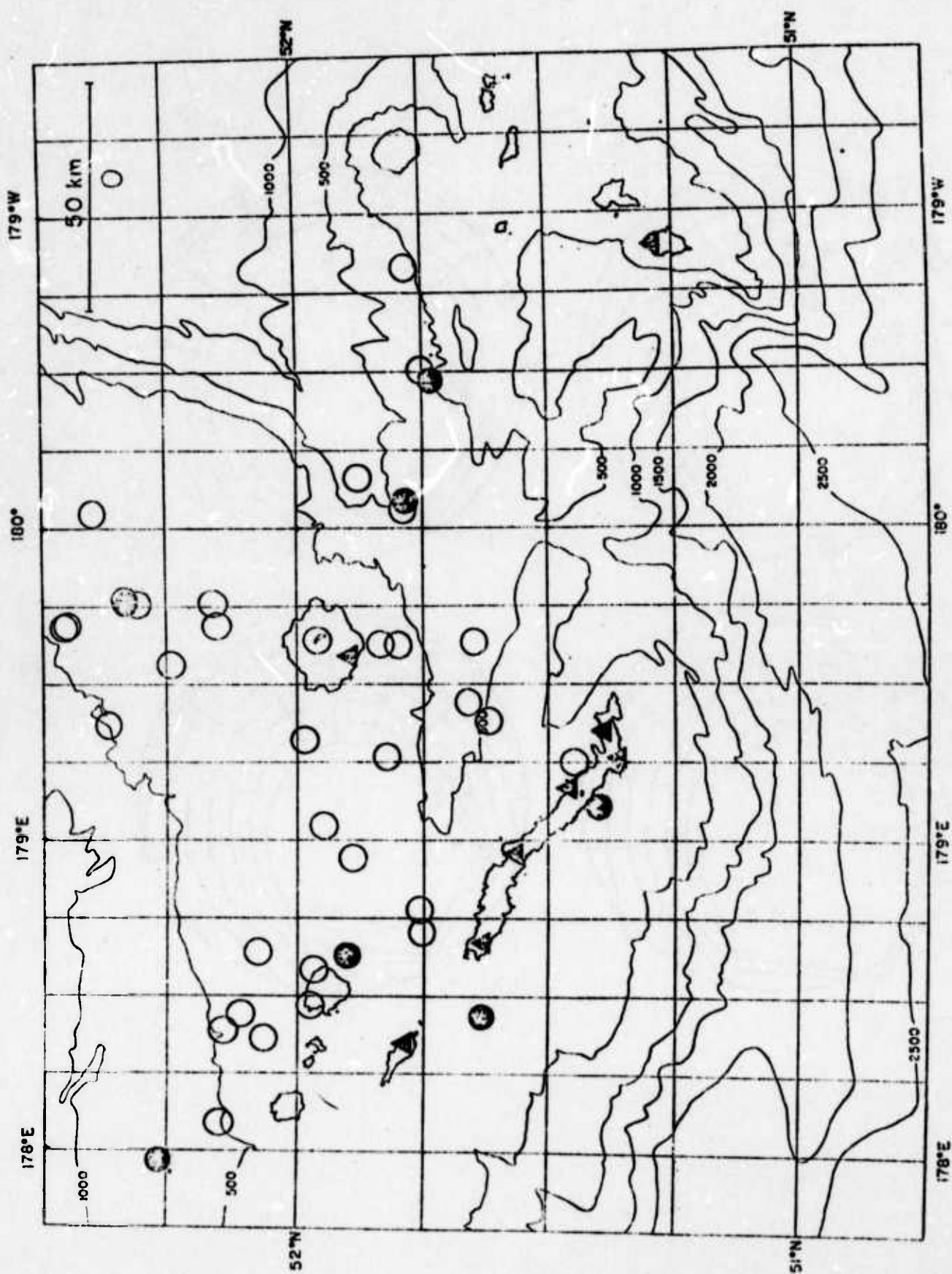


Figure 1.4

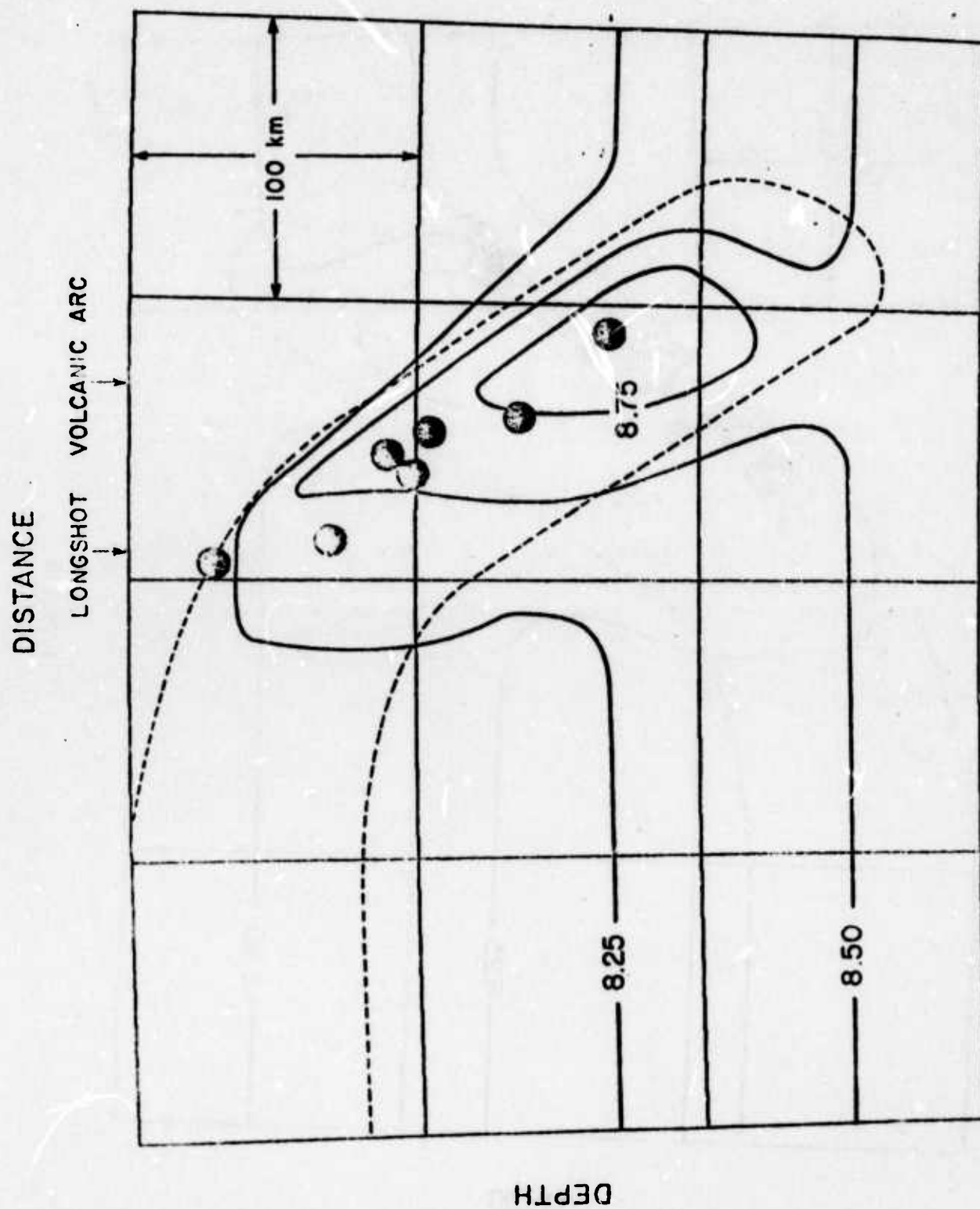


Figure 1.5

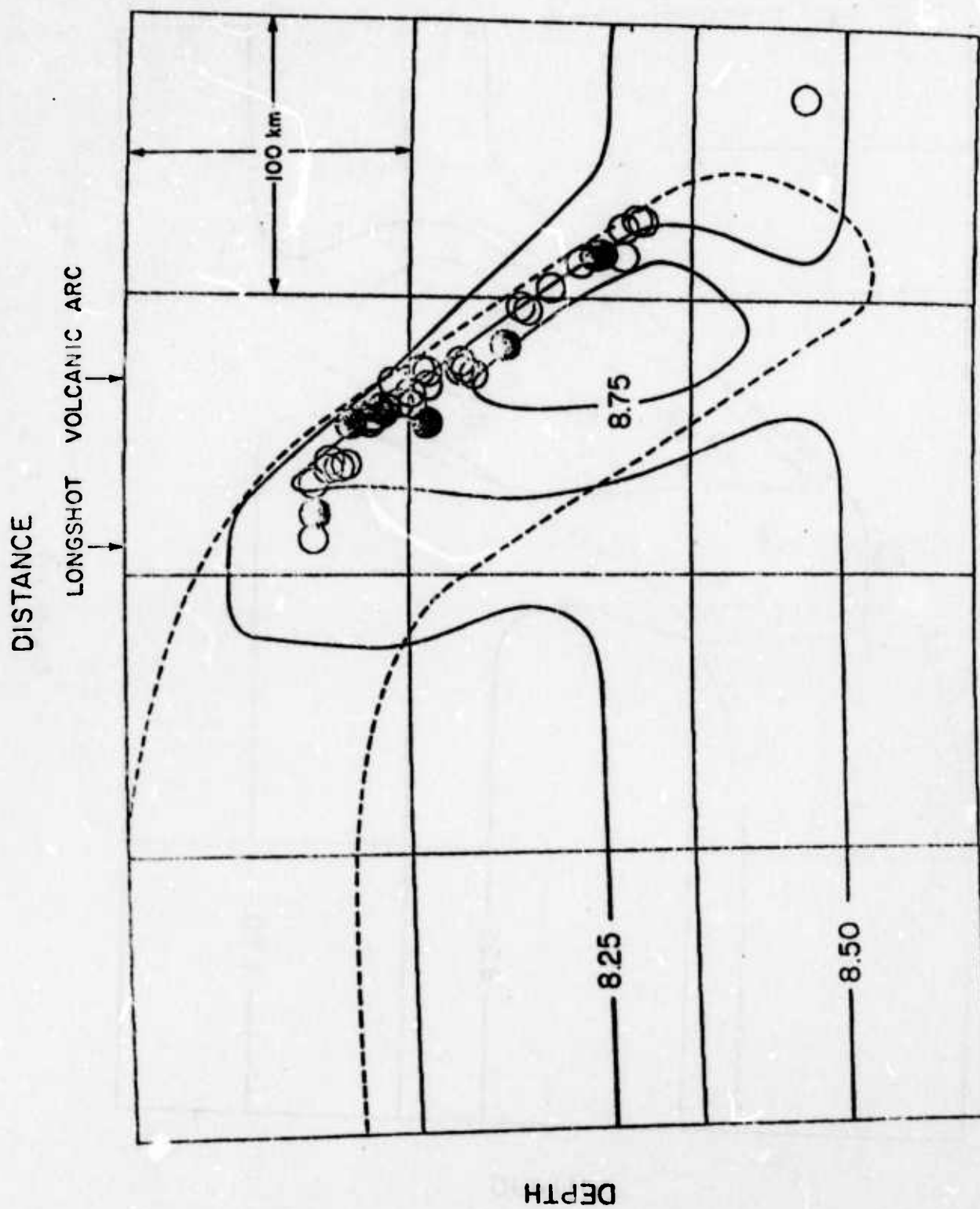
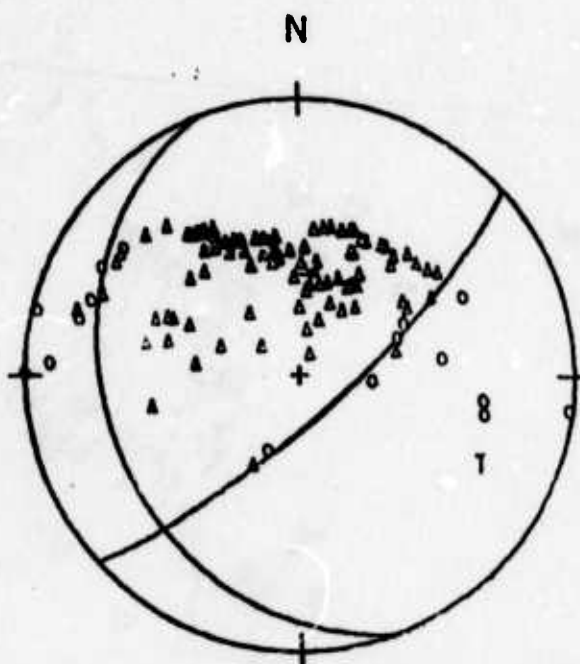


Figure 1.6

ALEUTIAN

a) INTERMEDIATE

66
72
78
86
90
92
101
101
104
106
106
118
118
120
140
151



b) DEEP

123
143
168
169 T
176

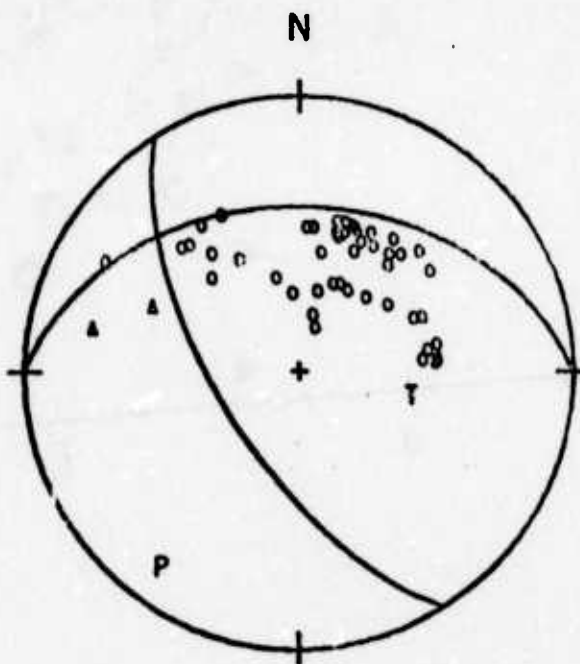


Figure 1.7

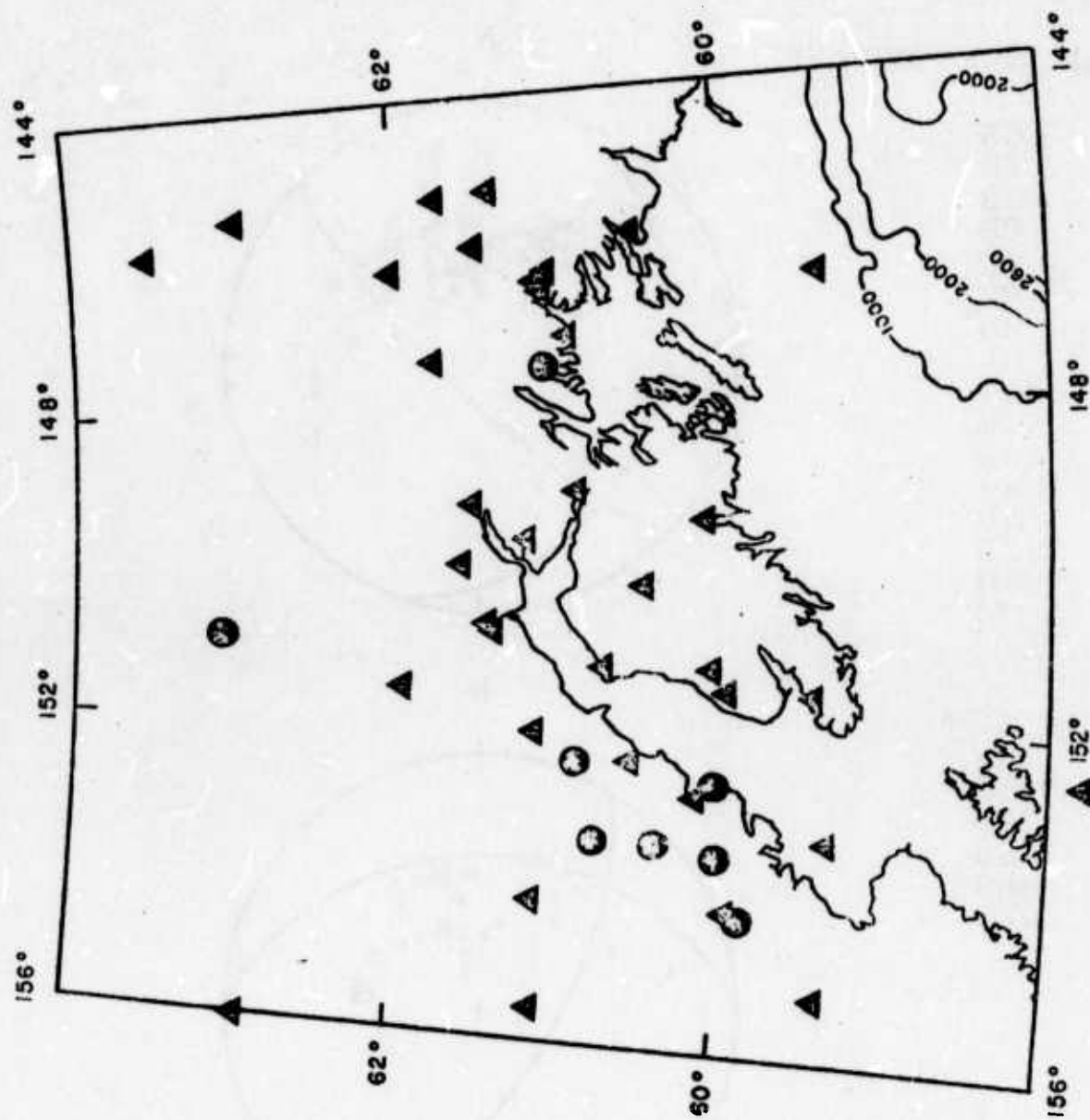


Figure 1.8

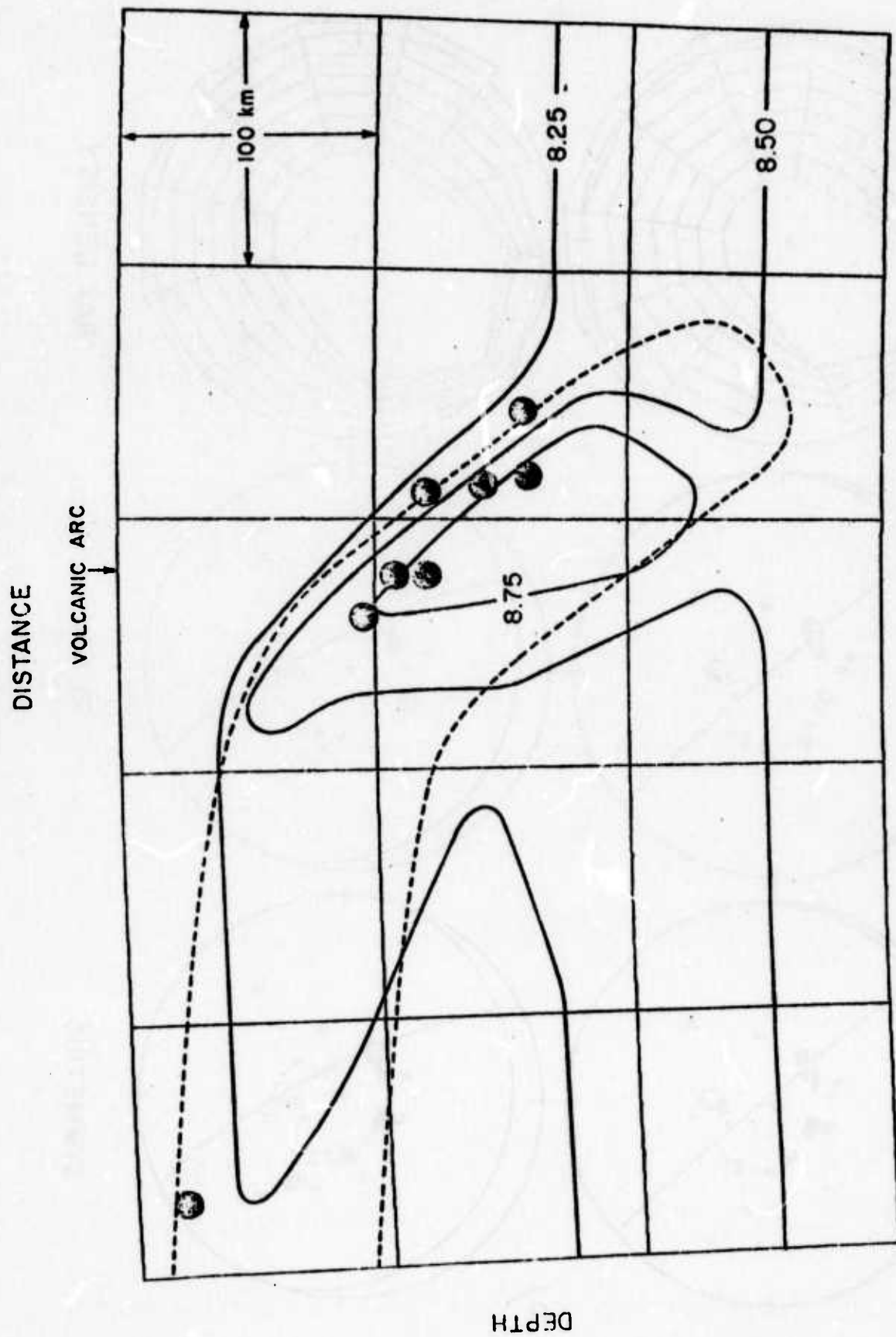


Figure 1.9

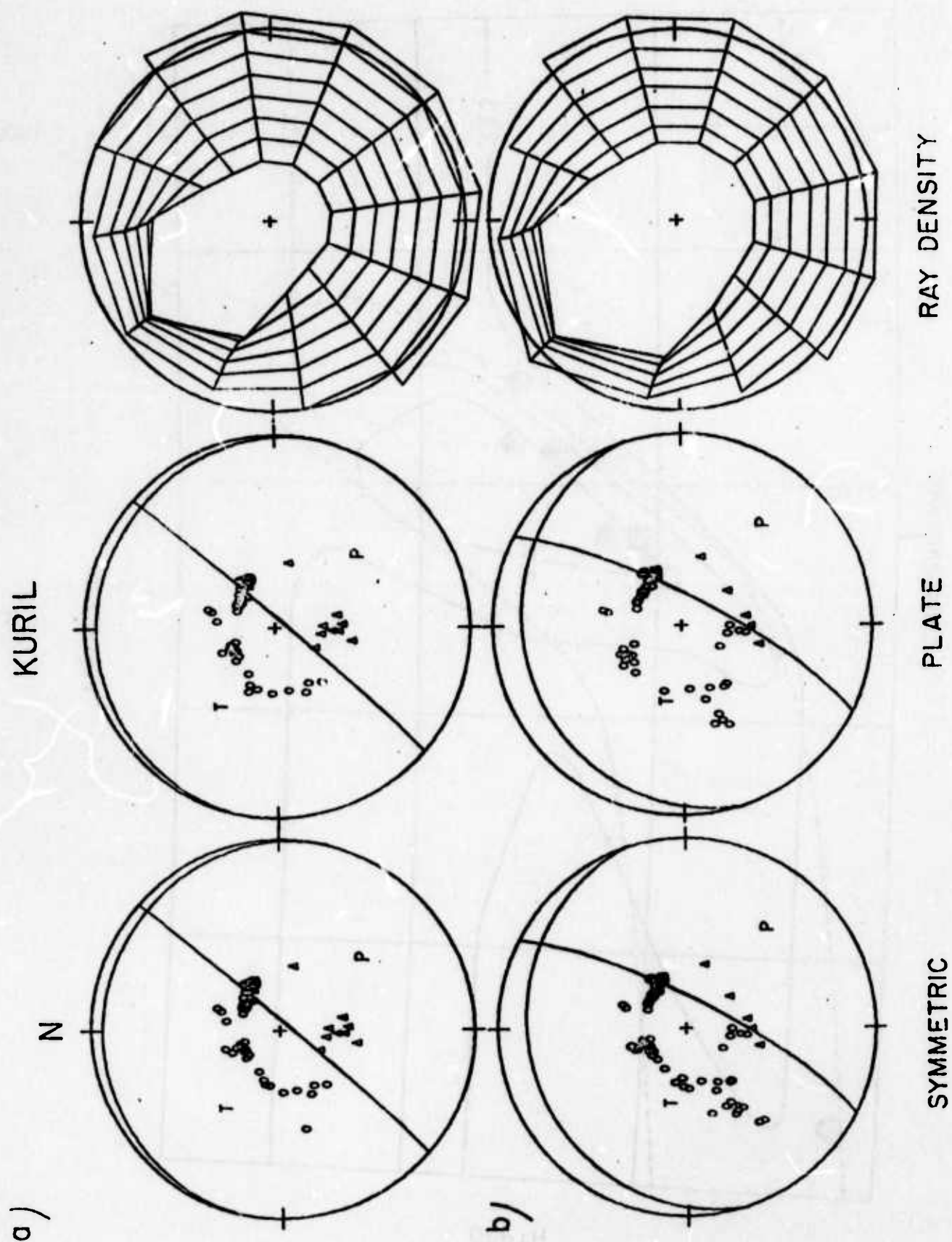


Figure 1.10

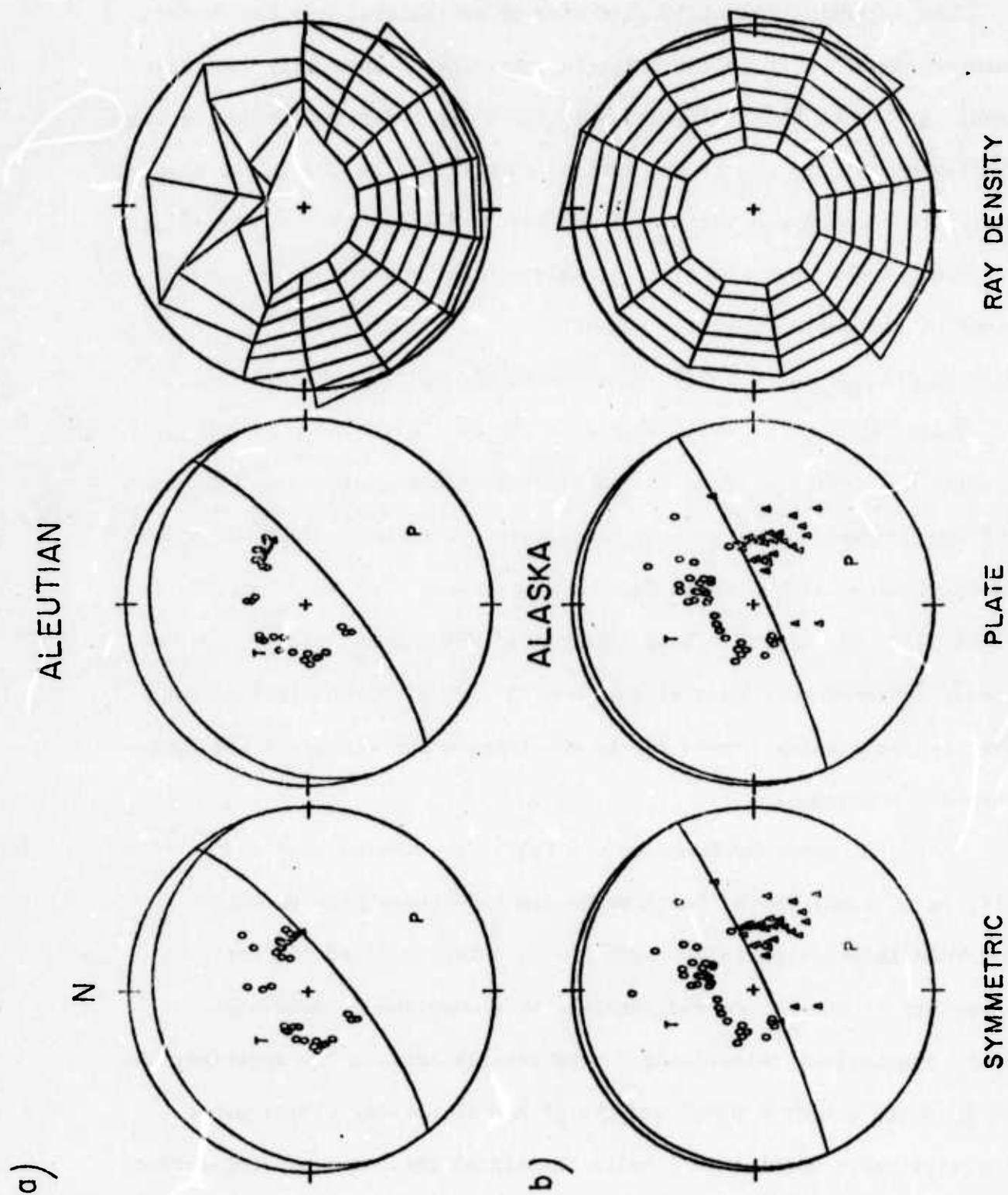


Figure 1.11

2. Focal Depth Determination from the Signal Character of Long Period P Waves

Robert B. Herrmann

Introduction

The determination of focal depths of earthquakes has long been an interesting and difficult problem in seismology, especially for crustal events. Some of the difficulties in focal depth determination for such shallow events are due to the lack of sensitivity in the travel time curves to focal depth variation, inadequate distribution of recording stations, and a poor signal to noise ratio for picking the arrival times of the depth dependent phases.

The use of short-period seismograms yields the required time resolution needed for precise focal depth determination. However, complex scattering effects due to crustal inhomogeneities as well as the earthquake rupture process complicate the record. This makes the identification of the depth determining phases, such as pP and sP, difficult. On the other hand long-period seismograms usually have a clean, coherent body wave signal, but the depth phases are distinct only for subcrustal events due to the integrating effect of the long-period seismograph.

A recent paper by Langston and Helmberger (1975) studied the effects of focal depth, focal mechanism and stress drop upon the recorded long-period teleseismic P wave. They modeled the earth structure at the source and receiver by a homogeneous halfspace. Their synthesized teleseismic P wave signals contain the contributions of just the direct P wave, and the pP and sP phases. Their paper suggests the possibility of using the signal character of long-period P waves as a focal depth discriminant.

The object of the present paper is to test the suitability of using the teleseismic P-wave signal to determine focal depth using more realistic models of the earth structure at the source and receiver than used by Langston and Helberger (1975).

Theory

The predicted seismogram $y(t)$ is determined using the relation

$$y(t) = s(t) * R_{sc}(t) * M(t) * R_{rc}(t) * I(t) \quad (1)$$

where $s(t)$ is the source time function of the double couple without moment force system; $R_{sc}(t)$ is the time history of the teleseismic mantle P wave due to an impulsive source within the layered medium used for the crust and upper mantle; $M(t)$ is the mantle impulse response for P waves; $R_{rc}(t)$ is the response at the surface of the receiver crust for an incident impulsive teleseismic P wave; $I(t)$ is the impulse response of the seismograph system used; and $*$ is the convolution operator.

Usually $s(t)$ is not specified when studying teleseismic P waves. Rather $s'(t)$, the time derivative of $s(t)$, is used since the time history of the far-field body-wave motion is proportional to $s'(t)$ for the double couple without moment source (Keylis-Borok, 1950). In this study $s'(t)$ is taken to be a positive pulse, shaped like an isosceles triangle with a base of 1 seconds and an area numerically equal to the seismic moment, M_0 .

$R_{sc}(t)$ is found using Hudson's (1969) extension of the Haskell (1964) matrix formalism to the generation of teleseismic body waves from a point system of forces acting within a plane-layered model of the upper mantle and crust. $R_{sc}(t)$ is a function of the crustal model, the phase velocity of the teleseismic P wave, the focal depth, and the orientation of the system of forces at the source. A point double-couple without moment source is used in this study.

$N(t)$ represents the impulse response of the mantle transfer function. Following Langston and Helmberger (1975), a reasonable approximation for $N(t)$ in the epicentral distance range of 30° - 80° is

$$N(t) = G(\Delta) Q(t) \quad , \quad (2)$$

where $G(\Delta)$ accounts for the effect of geometrical spreading within the mantle upon the amplitude of the P wave. Δ is the epicentral distance from the source to the receiver. The values of $G(\Delta)$ used in this paper are taken from Langston and Helmberger (1975). $Q(t)$ accounts for the effect of anelastic attenuation in the mantle. In the frequency domain the magnitude of this effect is taken to be

$$|Q(\omega)| = \exp(-\omega T/2Q) \quad (3)$$

where ω is the angular frequency, T is the travel time of the P wave in the mantle, and Q is the average Q factor along the particular path of the P wave. Following Langston and Helmberger (1975), we take $T/Q = 1$ as a reasonable approximation for teleseismic P waves in the epicentral distance range of $\Delta = 30^\circ$ to 80° . This epicentral distance range was chosen to avoid signal complications due to arrivals from other branches of the travel time curve or from deep reflections.

In the present paper $Q(t)$ is taken to be non-causal. This necessarily implies that the source time function $s(t)$, obtained by fitting the observed P wave motion by the theory of equation (1), is not truly representative of the history of the faulting at the source, but rather that $s(t)$ is such that $s(t) * Q(t)$ yields the

appropriate shape of the teleseismic P wave. Because of the nature of $|Q(\omega)|$, the seismic moment determination, the zero frequency level of the Fourier transform of $s'(t)$, as well as corner frequency information will not be affected by the use of a non-causal $Q(t)$ filter. The causal $Q(t)$ function is discussed by Futterman (1962) and Strick (1970).

$R_{rc}(t)$ gives the ground motion at the surface of the layered receiver crust-mantle system for a teleseismic mantle P wave incident at the base of the layered system. The formalism of Haskell (1962) is used. In this paper, $R_{rc}(t)$ is used to generate the vertical component of displacement at the free surface.

The seismograph impulse response $I(t)$ is synthesized for a 15-300 WSSN long period vertical system with a peak magnification of 3000. Hagiwara's (1958) formula for the response of an electromagnetic seismograph is used together with the appropriate system constants given by Chandra (1970).

To gain an insight into the nature of the focal depth information contained in the observed teleseismic P wave signal, the contributions of $R_{sc}(t)$ and $R_{rc}(t)$ to the observed P wave are considered in detail for several earth models.

The earth models used are given in Table 1. Model A is a truncated version of the oceanic model given by Harkrider (1970). Since we are interested in modeling shallow events, only the upper 80 km of Harkrider's (1970) oceanic model is used. Model B is a similarly truncated version of the shield model of Harkrider (1970). Model C

is a simple crustal model with a 30 km thick crust. Model D has the velocities as Model C but it has a 40 km thick crust.

Figure 1a shows the function $R_{ss}^c(t)$ determined by using the source whose parameters are given in Table 2 under the event entitled TEST. Model D of Table 1 was used for the source region structure. The seismograms are for a ray which leaves the source along an azimuth of 0° with a phase velocity of 16 km/sec. Several easily identifiable phases can be identified in the first ten seconds of the record. The first arrival is the P wave which goes downward from the source and becomes the mantle P wave at the crust-mantle boundary. The second phase, denoted as S, leaves the source as S and is converted into a component of the teleseismic P wave by transmission at the crust-mantle interface. The other phases are free surface reflections which are converted to teleseismic P waves at the crust-mantle boundary. It is important to note that the S waves generated by the double-couple source can make a large contribution to the shape of the resultant teleseismic P wave.

Figure 1b shows the vertical component of ground displacement at the surface of the receiver crust for an incident mantle P wave having a phase velocity of $c = 16$ km/sec and a triangular shaped pulse with $\tau = 2.0$ sec. Crustal model D was also used for the earth model. The phase identified as P represents the contribution to the vertical displacement due to the crustal P wave excited by the incident mantle P wave. The S phase represents the contribution due to the mantle P wave to crustal S wave conversion at the crust-

mantle interface. The PPP arrival represents the contribution due to the first reverberation within the crust such that the wave travels as P on all three segments of the ray path. The next arrival on the seismogram trace is due to the simultaneous arrival of the three rays SPP, PSP, and PPS. It is seen that these multiple reflections are large enough to affect the character of the resultant surface displacement up to twenty seconds after the direct P arrival.

The relative time delays between the arrivals is a function of the velocity model within the crust. The partition of amplitudes between the P and S contributions is basically a function of the velocity and density contrasts at the crust-mantle boundary. The crustal model used here has a very pronounced material contrast at the crust-mantle boundary. Thus the P to S and S to P conversions at the crust-mantle boundary may be more efficient for this simple earth model than for a more detailed earth model.

Figure 1c gives the composite effect of both the source and receiver crusts, obtained by convolving the record sections of Figures 1a and 1b. The first ten to twelve seconds of signal following the P arrival of Figure 1c are quite similar to those of Figure 1a since the receiver crust does not perturb the teleseismic P wave signal much in this time frame. However, the receiver crust does affect the nature of the incident teleseismic P wave signal at later times.

Figure 2 shows the effect of focal depth and different crustal modeling upon the observed vertical displacement of the P wave signal. The traces shown are the function $s(t) * R_{sc}(t) * R_{rc}(t)$

for the same source and receiver configuration used in Figure 1.

Figure 2a uses Model C for both the source and receiver crusts,

Figure 2b used Model D, and Figure 2c has Model B for the source and receiver crusts. The synthetic seismograms were generated for focal

depths of 10 and 20 kilometres. The effect of focal depth upon the signal character is quite profound. In Figure 1, it was seen that

the prime contributors to the teleseismic P wave were the P, pP

and sP phases. The time delays of the surface reflected pP and

sP phases relative to the direct P phase are functions of the focal

depth. For shallow events, the time delays are small. For the

particular choice of the source orientation used here, the pP and

sP phases have the same polarity so that they interfere constructively

for the 10 km event to produce a broad arrival following the direct

P contribution. As the focal depth increases, the phase separation

increases and the pP and sP phases appear as distinct arrivals.

The effect of different continental crust models is not as profound as the focal depth effect. Comparing a simple crust with a

crustal thickness of 30 km, Figure 2a, with one with a 40 km thick

crust, Figure 2b, no major difference is seen other than a slight

change in the character of the latter part of the trace. Contrasting

Figure 2c with Figure 2b, the effect of a more detailed crustal model

is a smoothing of waveform shape for arrivals after the direct P

contribution due to the presence of many more crustal multiples in

the record section.

Observations

In Equation 1, we note that many variables affect the shape of the observed seismogram. These factors are the orientation of the earthquake focal mechanism, the source time function, the crustal structures at the source and the receiver, and the focal depth. Usually, a rough estimate of the crustal structure can suffice in modeling the P arrival since we have seen from Figure 2 that the crustal structure does not affect the gross detail of the predicted ground motion very much. On the other hand, the orientation of the focal mechanism, the shape of the source time function, and the focal depth are usually not very well known. Various search techniques or inversion techniques have been used to determine these parameters by finding the best fit between the predicted and observed seismograms at a number of stations. Some useful techniques have been outlined by Mellman et al (1975) and Langston (1975).

Since the object of this paper is to demonstrate the potential of using long period P waves for focal depth resolution, we require that the focal mechanism and source time function as well as focal depth be determined previously. This determination was made by finding the combination of these parameters which gave the best fit to the P wave signal at fifteen selected WWSSN stations. The parameters of the two earthquakes so considered are given in Table 2. The source parameters given are the orientations of the pressure and tension axes, the base length of the isosceles triangle shaped source time function, the seismic moment and the focal depth. All the factors given in Equation

(1) are included in the synthesis of the seismograms.

The first event considered is the Alma-Ata event of June 5, 1970. This event occurred at 04:53:06 with an epicenter 42.5° N and 78.8° E. Figure 3 presents the observed vertical component long-period P-wave signal at CHG, a distance of 29.2° from the source along an azimuth of 138° . Also presented in this figure are the synthesized long-period P wave signals for various focal depths using earth model B for both the source and receiver crusts. At this epicentral distance, the P-wave phase velocity for focal depths between 0 - 50 km is insensitive to focal depth and a value of 11.02 km/sec was used (Herrin et al, 1968). The focal depth range of the synthetic seismograms is between 1 and 51 km. All other source parameters are held constant. The scaling bar represents 1 cm of displacement on a 15-100 WSSN seismograph with a peak magnification of 3000.

The effect of focal depth is exhibited in several ways. As the focal depth increases within the crust, some character is introduced into the first part of the signal due to the increasing pP-P and sP-P time delays. As the focal depth increases so that the source lies in the upper mantle, the direct P wave amplitude decreases because the direct P wave contribution leaves the source near a nodal plane (in other words, since the phase velocity does not change, the takeoff angles are functions of the source layer velocity and hence focal depth). A visual comparison of the observed CHG record with the synthetic records indicates that the focal depth of the event would be bracketed between $H = 1$ km and $H = 21$ km.

To obtain a more quantitative choice of the best fitting focal depth, the following procedure was used. A pair of the twelve traces given in Figure 3 were cross-correlated over a time shift of .14 seconds from the beginning of the trace. When the time shift giving the maximum cross-correlation was found, a correlation coefficient between the shifted traces was determined; a correlation coefficient equal to 1.0 indicates excellent fit between the two traces. The cross-correlation was used because in actuality there is always some doubt as to the exact arrival time of the P pulse and in the initiation of the digitizing process of the observed signal.

Table 3 presents the correlation coefficients obtained by correlating the first 37 seconds of the traces shown. Since the matrix of correlation coefficients is symmetric about the diagonal, only half of the matrix is given in Table 3. Considering the correlations between the various synthetic traces, we see that there is a good correlation greater than 0.900, for focal depths within ± 10 km of the chosen focal depth. On the other hand, the matrix indicates a distinct non-correlation between any two traces whose focal depths are separated by at least 15 km. Comparing the correlations between the observed CHG trace and those for the various focal depths, it is seen that the best fit occurs in the neighborhood of $H = 16$ km, with anything deeper being positively rejected. In order to set confidence limits on the focal depth, a generalized inversion technique would have to be used (Mellman et al, 1975). This event has been assigned focal depths of $H = 20$ km by NOAA and $H = 24$ km by the ISC.

The problem of focal depth determination for events located within an oceanic crust was also considered. The Aleutian Island event of August 7, 1966 was used. The focal mechanism parameters listed in Table 1 are taken from Stauder (1968). The origin time is 02:13:04 and the epicenter is located at 50.6° N and 171.3° W. A truncated version of the oceanic model of Harkrider (1970), Model A of Table 2, was used for the source crust. The continental crust model, Model B was used for the receiver crust at KEV. The seismic moment and source pulse shape were determined in this study. KEV is 59.2° from the source along an azimuth of 352.7° . A phase velocity of 16.092 km/sec was used. The observed KEV P wave signal is given in Figure 4 together with synthetic records for various focal depths. The scaling bar represents 2.5 cm displacement on a 15-100 long-period seismogram with peak magnification of 3000.

A comparison of Figure 4 with Figure 3 points up a profound difference in the character of the theoretical long period P wave signal. This difference is the almost constant period reverberation following the initial P wave motion for the event occurring in the oceanic model. This reverberation is due to the presence of the water layer, with the period of the reverberation being a function of the thickness of the water layer.

The first 30 seconds of the seismograms in Figure 4 were correlated using the same procedure as for the CHC record. The following maximum correlation coefficients were determined between KEV and the various focal depths: 0.926, 0.897, 0.961, 0.967, 0.974, 0.903, 0.821, and

0.484 for focal depths of 6.5, 10, 15, 19.5, 24.5, 27.5, 30, and 35 km, respectively. Even though the $H = 6.5$ km correlation coefficient is quite good, the theoretical P wave break is not as sharp as that observed on the KEV record. On the basis of these correlation coefficients and a visual comparison of the traces, a focal depth in the range of 15 -- 24.5 km would explain the KEV seismogram. Performing this analysis with a number of observed seismograms would provide a tighter control on the focal depth. For comparison, the focal depth of this event was given as $H = 39$ km by the USCGS and $H = 29$ km by the ISC.

Conclusions

The possibility of using the signal character of long-period P waves has been demonstrated, but something must be said about the applicability of this technique. The present study indicates that it is not unreasonable to obtain a resolution of about fifteen kilometers in focal depth. This means that an event could be classified as having occurred in the upper or in the lower crust.

There are some restrictions in obtaining this resolution. First and foremost is the quality of the data available. The events considered here have a relatively high signal to noise ratio. The six-second microseism level may be on the order of several tenths of a centimeter on a typical 15-100 WSSN seismogram with a magnification of 3000. Between the microseism noise level and the width of the seismogram trace, it would be difficult to apply this technique to events with seismic moments less than one-tenth that of the June 5, 1970 event which had an $M_s = 6.3$ and an $m_b = 6.0$.

The P-wave detectability may be improved by using a high-gain long-period seismograph system designed to reject the microseism noise, but the result may be a greater lack of resolution in the depth resolution due to the fact that a longer period seismograph is being used. This aspect of the problem will be covered in a future study.

Since the emphasis of this study was toward focal depth resolution for small events, the problem of a complex three dimensional source was not considered. However, the work of Mellman et al (1975) and Langston (1975) indicates that information concerning depth and rupturing

can be extracted from the long-period teleseismic P wave.

The present study may also be described as semi-quantitative, it would be well to study this problem from the viewpoint of generalized inverse theory in order to be able to set some confidence limits on the focal depths determined.

References

- Chandra, U. (1970). Analysis of body-wave spectra for earthquake energy determination, Bull. Seism. Soc. Am. 60, 539-563.
- Futterman, W. (1962). Dispersive body waves, J. Geophys. Res. 67, 5279-5291.
- Hagiwara, T. (1958). A note on the theory of the electromagnetic seismograph, Bull. Earthquake Res. Inst. 36, 139-164.
- Harkrider, D.G. (1970). Surface waves in a multilayered elastic media Part II. Higher mode spectra and spectral ratios from point sources in plane layered earth models, Bull. Seism. Soc. Am. 60, 1937-1987.
- Haskell, N.A. (1962). Crustal reflection of plane P and SV waves, J. Geophys. Res. 67, 4751-4767.
- Haskell, N.A. (1964). Radiation pattern of surface waves from point sources in a multi-layered medium, Bull. Seism. Soc. Am. 54, 377-393.
- Herrin, E. et al (1968). 1968 seismological tables for P phases, Bull. Seism. Soc. Am. 58, 1193-1225.
- Hudson, J.A. (1969). A quantitative evaluation of seismic signals at teleseismic distances - II. Body waves and surface waves from an extended source, Geophys. J. 18, 353-370.
- Keylis-Borok, V.I. (1950). On the question of determining the dynamic parameters of a focus (in Russian), Trudy Geofiz. Inst., Akad. Nauk SSSR, No. 9 (136), 3-19.

- Langston, C.A. (1975). The relationship between the teleseismic P-wave and near-field strong motion observations for the 9 February 1971, San Fernando earthquake (abstract), Earthquake Notes 46, 39.
- Langston, C.A. and D.V. Helmberger (1975). A procedure for modeling shallow dislocation sources, Geophys. J. 00, 000-000.
- Mellman, G.R., L.J. Burdick and D.V. Helmberger (1975). Determination of source parameters from body wave seismograms (abstract), Earthquake Notes 46, 44.
- Stauder, W. (1968). Tensional character of earthquake foci beneath the Aleutian trench with relation to sea-floor spreading, J. Geophys. Res. 73, 7693-7701.

TABLE 1

EARTH MODELS

A. Oceanic Model (Harkrider, 1970)

Thickness (km)	P wave velocity (km/sec)	S wave velocity (km/sec)	Density (gm/cm ³)
5	1.52	0.10	1.03
1	2.10	1.00	2.10
5	6.41	3.70	3.07
9	8.11	4.61	3.40
5	8.12	4.61	3.40
15	8.12	4.61	3.40
20	8.01	4.56	3.37
20	7.95	4.56	3.37
--	7.71	4.40	3.37

B. Continental Model (Harkrider, 1970)

16.5	6.10	3.54	2.55
5	6.40	3.70	3.08
13.5	6.70	3.92	3.42
25	8.15	4.75	3.42
20	8.21	4.75	3.42
----	8.26	4.75	3.42

C. 30 km crust model

30	6.00	3.50	2.70
--	8.00	4.62	3.30

D. 40 km crust model

40	6.00	3.50	2.70
--	8.00	4.62	3.30

TABLE 2

EVENT PARAMETERS

Event	T-axis		P-axis		τ (sec)	$G(\Delta)$ (km ⁻¹)	M_0 (dyne-cm)	H (km)
	Tr	P1	Tr	P1				
TEST	0°	90°	90°	0°	2.0	1.0	1.0	
Jun 5, 1970	242°	71°	338°	2°	7.4	8.5E-10	5.0E25	13
Aug 7, 1966	331°	64°	200°	18°	6.0	5.6E-10	1.5E26	24.5

TABLE 3

Correlation matrix for CHG record 05 JUN 70

[illegible]

Figure Captions

Figure 2.1. (a) Mantle P-wave due to source crust interaction ;
(b) Vertical displacement at free surface of receiver
crust due to an incident mantle P-wave ; (c). Convolution
of source crust and receiver crust responses.

Figure 2.2. Effect of focal depth and crustal structure
upon the resultant vertical component ground
displacements. (a) earth model C ; (b) earth model D ;
(c) earth model B.

Figure 2.3. Observed P-wave signal at CHG for the June 5, 1970
event compared to synthetics for various focal depths.
The scaling bar , represents 1 cm displacement on a
3K 15-100 WWSSN seismogram.

Figure 2.4. Observed P-wave signal at KEV for the August 7, 1966
event compared to synthetics for various focal depths.
The scaling bar represents 2.5 cm displacement on a
3K 15-100 WWSSN seismogram.

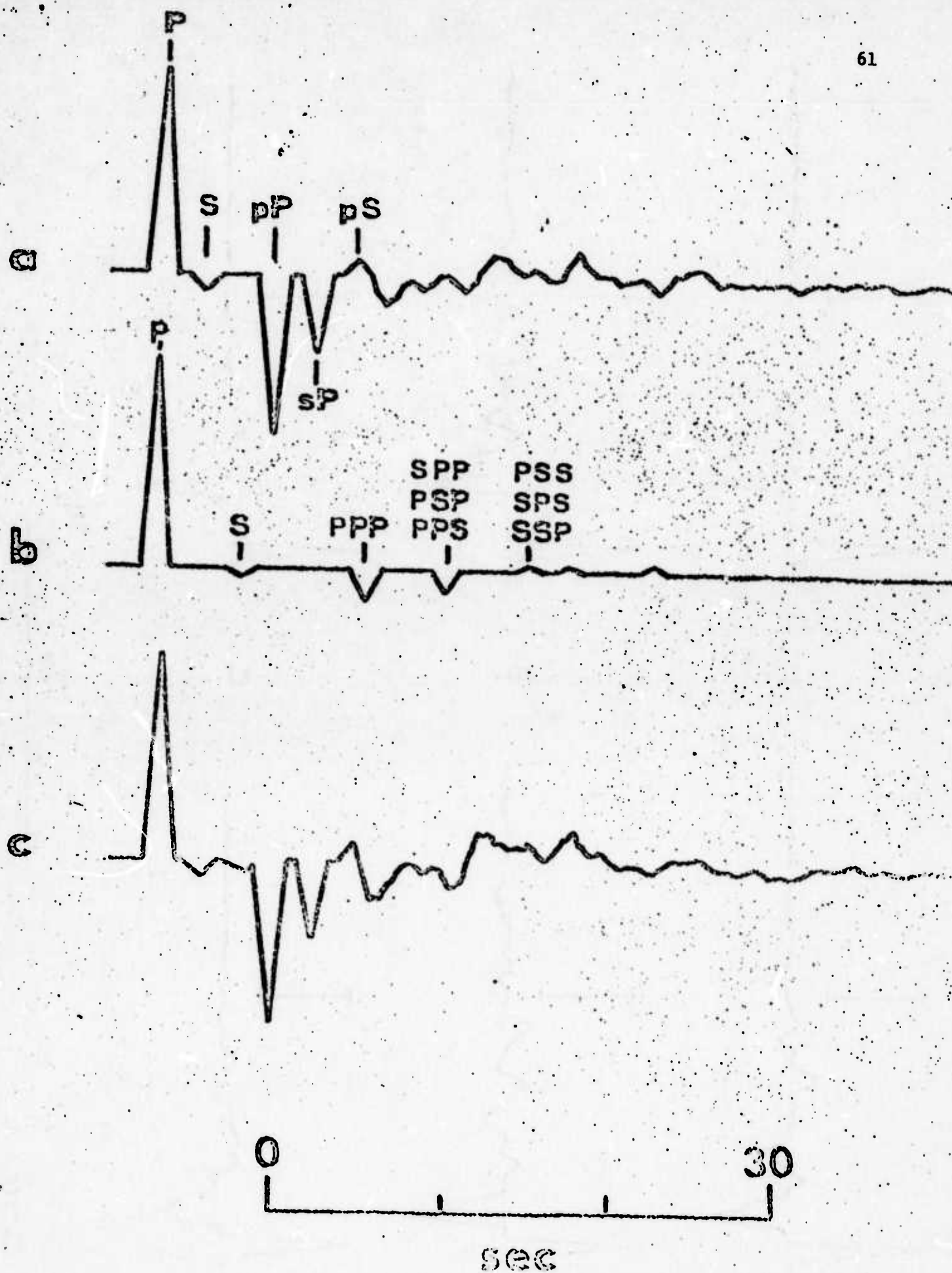
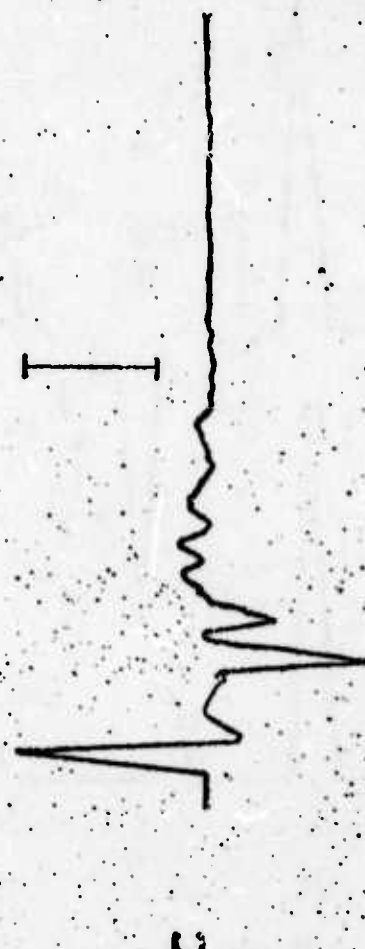
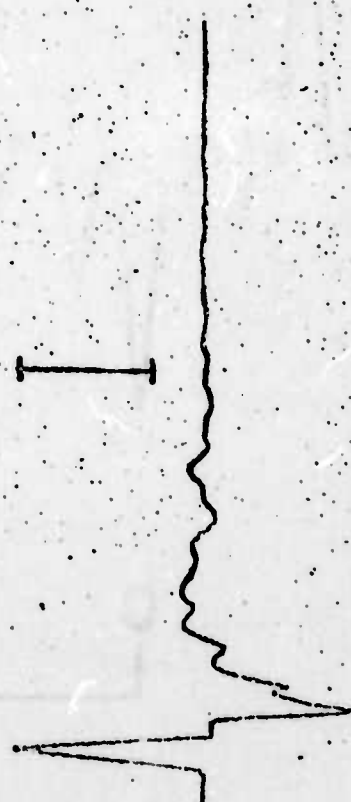
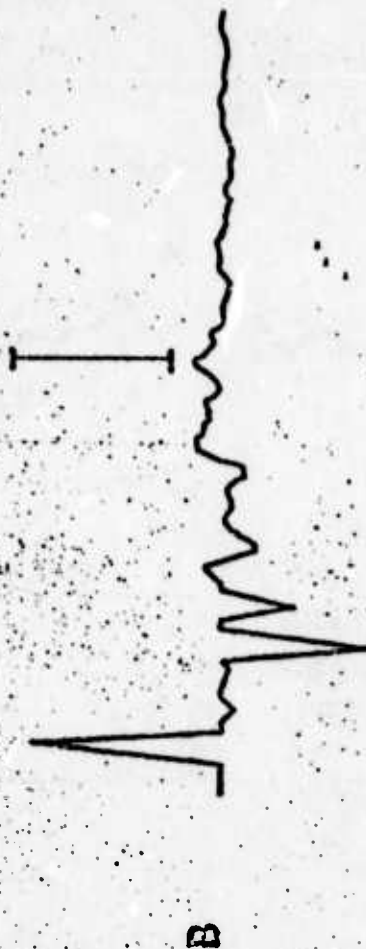
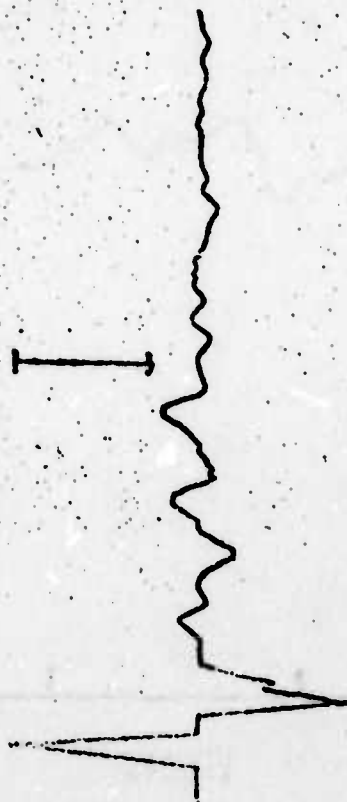
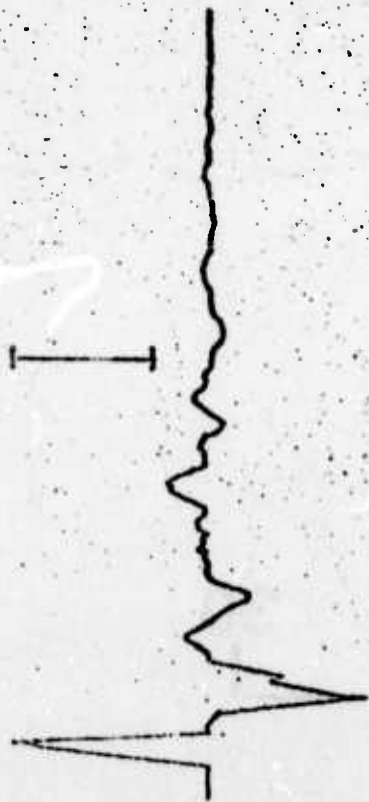


Figure 2.1

H = 10

H = 20



0 30
SEC

Figure 2.2

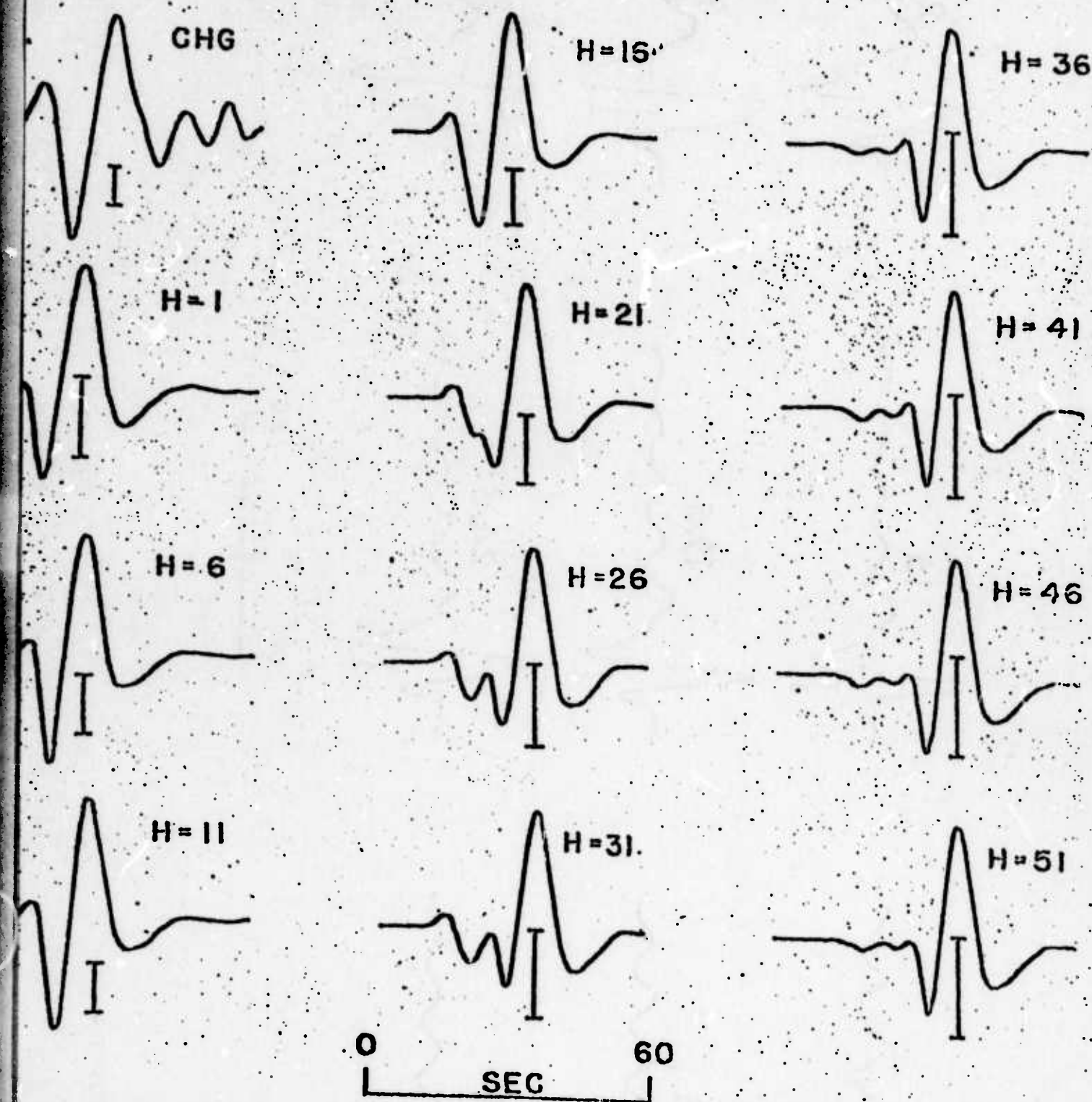


Figure 2.3

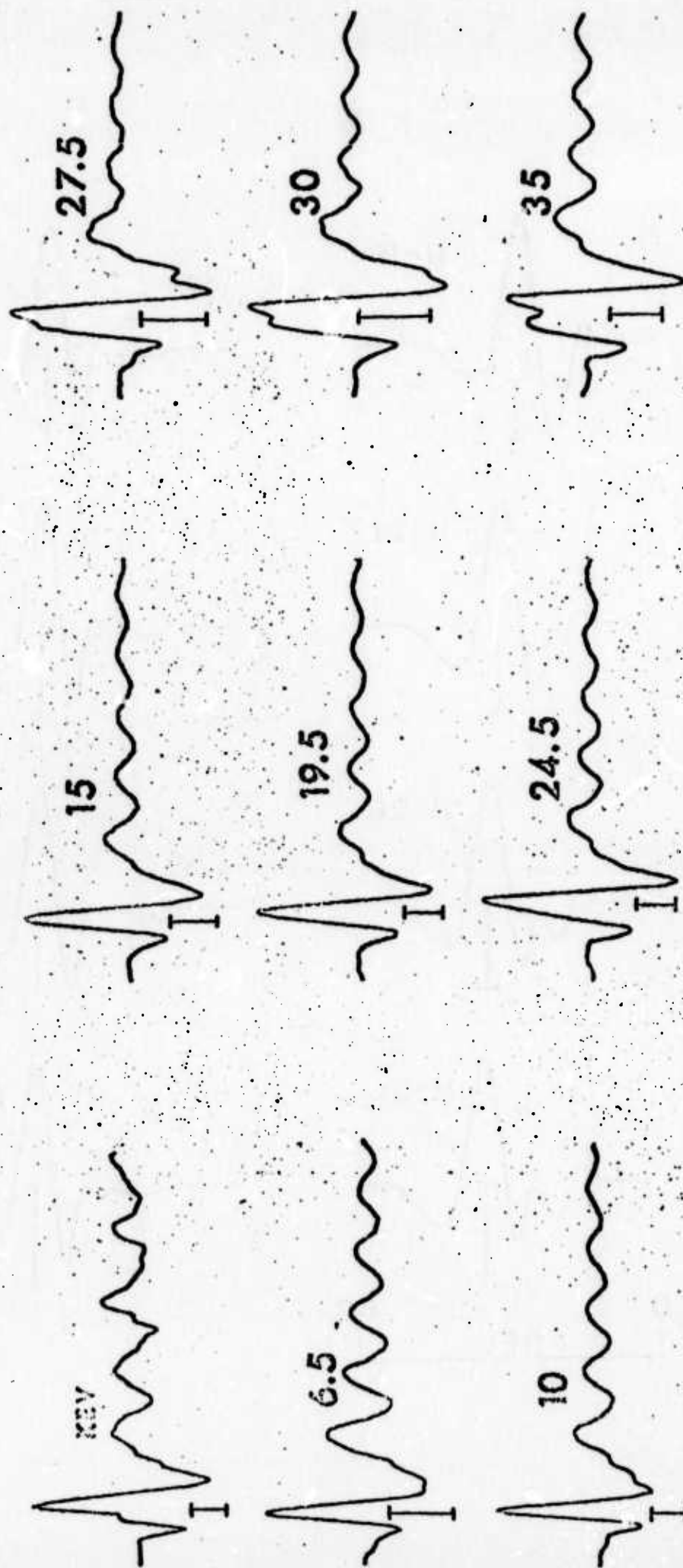


Figure 2.4

3. Source Characteristics from Long Period P Wave Observations

R. B. Herrmann and T. Hewitt

In the previous semi-annual report, we presented a method determining earthquake source parameters from a study of the long-period teleseismic P-wave character. The theoretical discussion in that report has been updated by using the corrected reflection and transmission coefficients for seismic rays in the source region (Bache et al., 1975b). As a further extension of the theory given in the previous semi-annual technical report, we used Hudson's (1969) extension of the Haskell (1962, 1964) formalism to produce synthetic seismograms for teleseismic P waves for source crust and receiver crust models which are more complicated than the single layered constant velocity crust overlying a constant velocity mantle used previously.

The technique used in determining the source parameters of an earthquake is quite simple. Long-period teleseismic P waves from stations located uniformly about the epicenter are compared with theoretical P waves generated for a particular combination of strike, dip, slip, focal depth and source time function. The parameter space of source parameters is searched until a combination is found which provides the best fit to both the amplitude and the shape of the observed P-wave signals.

Twelve earthquakes have been studied. Table I lists the events, e.g., giving the date, origin time, epicentral coordinates, focal depth and magnitudes. The focal depths and magnitudes listed were determined by the CGS or NOAA, the ISC and this study. No depths were determined for events 1 and 2, Aleutian trench, because the search technique is set up for continental events. Events 4, 5, and 12 are too deep to be processed. The focal depths determined from the teleseismic P-wave analysis differ

somewhat from those given by the CGS or NOAA and the ISC. Our depth estimate of the 22 May 1971 Turkish event is the only one which differs substantially from the estimates of the other two sources. We also determined the magnitude of the events together with standard deviations. The number in the parentheses indicates the number of data used in our determinations. In general, our magnitude determinations are somewhat less than those from the other sources, but the other determinations usually fall within our standard deviations.

Table II presents the focal mechanism parameters of the events listed in Table I. Of the 12 events listed, we determined the focal mechanisms of seven events. The P-wave first motion data and S-wave polarization data are presented in Figure 1, together with the focal mechanisms determined from the long period P-wave signal analysis. In these figures, the O's represent compressional arrivals while the deltas represent dilatational arrivals. The X's represent arrivals of near nodal-plane quality. The P and T symbols represent the pressure and tension axes. The event of 12 Nov 1972 was a deep event and readings were available from the pP arrival; the minus's represent dilatations obtained from the pP arrivals after correction for the phase reversal due to the free surface reflection.

The focal mechanism of the 14 Oct 1968 Meckering, Australia agrees relatively well with the observed surface faulting. The surface faulting extended a distance of 30 km in an arcuate trend, striking southeast at the southern end of the fault and northeast at the northern end. The overall trend is north-south. The motion on the fault was a thrust along a plane dipping 30° - 49° at the surface (Gordon, 1971).

Banghar (1974) published focal mechanism solutions for the 11 Feb 1969, 18 Jul 1969 and the 05 Jun 1970, events. His solution for the

11 Feb 1969 event has one nodal plane dipping 70° to the SW with a strike of 38° and the other nodal plane dipping 58° to the SW with a strike of 321° . There is no similarity whatsoever between our solution and his. The solutions for the 05 Jun 1970 events are quite similar. One of his nodal planes dips 50° to the NW with a strike of 68° while the other nodal plane dips 50° to the SE with a strike of 26° . This is very similar to our solution, the difference being a 20° difference in the strike of the nodal planes. This discrepancy is not major since we found the P-wave signal to be relatively insensitive to a rotation of the focal mechanism strikes since amplitudes of the P waves and SV waves are fairly insensitive to a rotation of the solution for the rays making up the teleseismic P wave.

Banghar's (1974) solution for the 18 Jul 1969 northeastern China event has one nodal plane striking along an azimuth of 109° and dipping 70° to the south, and the second nodal plane striking along an azimuth of 22° and dipping 80° to the west. This solution is quite similar to ours. The P-wave signal comparison technique began to break down for this event since this event was large enough that the assumption of a point dislocation source began to break down.

Besides determining the focal depth and nodal plane orientations, we were able to estimate the shape of the body wave source time function. Since we were using teleseismic P waves from a 15 - 100 WSSN seismograph and because of the effect of the earth's Q filter, we lack sensitivity in the fine structure of the source time function which can be obtained only from the high frequency content of the signal. To try to resolve the nature of the high frequency content of the signal, we obtained the shapes of the rectangular and isosceles triangular source pulses which gave the best fit to the data.

Table III presents the results of these determinations. In this table, T_{MAX} is the number of seconds of P-wave signal used in the determination of the best fit; N is the number of stations making up the P-wave data set; H is the focal depth (an asterisk indicates that the focal depth was not determined as part of the search technique); DT_1 , DT_2 and DT_3 represent the time lengths of the positive, zero and negative slopes of a positive trapezoidal source time function. The case $DT_1 = DT_3$ and $DT_2 = 0$ represents an isosceles triangular-shaped source time function while the case $DT_1 = DT_3 = 0$ and $DT_2 \neq 0$ represents a rectangular shaped source pulse. M_0 is the seismic moment in dyne-cm determined for each source time function. r is the correlation coefficient between the observed and predicted P-wave signals for the first T_{MAX} seconds for all N data sets.

In general, the seismic moment determinations are independent of the source time function assumed. This is true so long as the corner frequency associated with the source time function is greater than the minimum frequency resolvable in the P-wave signal. Since the focal depth determination depends on the interference of the primary and reflected body wave contributions to the teleseismic P wave, the focal depth determinations is dependent upon the shape of the input signal as well as the time delays due to focal depth. Hence, the focal depth estimate will be somewhat dependent upon the shape of the source time pulse.

Figure 2 presents a plot of the seismic moments, M_0 , versus the surface wave magnitudes, M_s , determined in this study. The numbers refer to the event number in Tables I and III. The error bars give the standard deviations of the M_s determinations. While standard deviations of the M_0 determinations were not obtained, they are probably on the order of a factor of 2. The dashed line is an extrapolation of seismic moment

versus M_s data for the central United States (Street *et al.*, 1975). The light solid line is the M_0 versus M_s relation based on Aki's (1972) ω^2 model of source spectrum scaling. Aki's model provides a good fit to most of the data. Exceptions are the three Aleutian Trench events of 01 Oct 1965, 02 Jun 1966 and 07 Aug 1966, which have consistently smaller M_s values than indicated by the M_0 versus M_s trend. The next section will show why we attribute this discrepancy to M_s rather than M_0 .

As an attempt at discerning the high frequency character of the source spectrum of these events, we considered the relationship between the spectral amplitude level at 1 Hz and m_b for each of the two source time functions from each event. The amplitude spectrum of a rectangular pulse of duration $DT2$ seconds has a corner frequency at $f_{01} = \pi/DT2$ Hz, which separates the f^0 and f^{-1} trends. For an isosceles triangular shaped source time function with a base of $2 * DT1$ seconds, the spectrum has a corner frequency at $f_{02} = \pi/DT1$ Hz, which separates the f^0 and f^{-2} trends of the spectrum. Obtaining the corner frequency and seismic moment from Table III for each source time function, and knowing the high frequency spectral trend, the spectral amplitude at a frequency of 1 Hz is easily determined. Table IV summarizes these computations. In this table, $T_{01} = 1/f_{01}$ and $T_{02} = 1/f_{02}$.

Figure 3 shows the spectral level at 1 Hz as a function of m_b . In this figure the numbers refer to the events listed in Table IV. The open triangles indicate the spectral level appropriate to a rectangular source pulse while the solid circles indicate the spectral levels obtained from the triangular shaped source pulse. The error limits are the standard deviations on the m_b values listed in Table I. The spectral levels are probably known to within a factor of 2, due to a similar uncertainty in the seismic moment values.

The dashed line represents the extrapolated trend of the 1 Hz spectral level as a function of m_b as determined by Street et al. (1975). It is interesting to note that the best fit to this trend is from an assumed triangular shaped source pulse rather than a rectangular shaped pulse. From this simple comparison, we conclude that the source spectra near 1 Hz approximately have an f^{-2} trend for most of these events. A possible exception might be events 7 and 11 which may have an $f^{-1.5}$ spectral trend near 1 Hz. Events 4 and 5 are deep focus events which indicate that a falloff faster than f^{-2} might be more appropriate. This indicates either that the corner frequency of these two events are probably not very well known or that a source time function is somewhat smoother than a triangular shaped pulse. Events 1, 2, 3, the Aleutian Trench events, fit the trend nicely with a triangular shaped pulse. This indicates that the M_0 value is fairly good and that the discrepancy in Figure 2 is due to M_s .

In conclusion, the following observations are made concerning the use of long-period teleseismic P waves for source characterizations.

a) The capability of focal mechanism determination is quite good since the observed long period P-waves train is composed of samples of both P and SV waves generated by the source.

b) Focal depth discrimination is good. This topic is covered elsewhere in this report.

c) The shape of the source spectrum, estimated from the solution of the P-wave signal problem agrees well with spectral scaling relations. From the source spectrum scaling of 1 Hz with m_b , we concluded that the triangular shaped source pulse is a better solution than a rectangular pulse. Note that we had to use m_b to be able to make this distinction.

Recent programming changes have made the method of determining source characteristics simpler to use, and more economical of computer time. The optimization of computer codes has been achieved by using the fact that (all other source parameters fixed) the seismograms, and hence their correlation coefficients and seismic moments, are linear functions of the amplitudes of the four source rays (2P and 2SV), which are determined by focal mechanism. Because of these changes computing efficiency has been improved by a factor of five to 100 times for various parameters. This improvement in computing efficiency has allowed most of the search for source parameters to be done automatically, and hence total time to process an event is now reduced to only two days, instead of two weeks.

Future studies should encompass the following:

- a) Estimation of the lower magnitude threshold for the application of this technique;
- b) Study of the 1 Hz spectral character from short period P waves to test the validity of our conclusions of the shape of the source pulse for these events;
- c) Investigation of the cause of the relatively low M_s value for the Aleutian Trench events.

References

- Aki, K. (1972). Scaling law of Earthquake Source Time-Function, Geophys. J. 31: 3-25.
- Bache, T. C., J. T. Cherry, K. G. Hamilton, J. F. Masso, and J. M. Savino (1975). Application of Advanced Methods for Identification and Detection of Nuclear Explosions from the Asian Continents, Science, Systems, Software, Report, AFOSR Contract Number F44620-74-C-0063, May, 1975.
- Banghar, A. R. (1974). Mechanism of Earthquakes in Albania, China, Mongolia, Afghanistan and Burma-India region, Earthquake Notes XLV: 13-25.
- Gordon, F. R. (1971). Faulting during the earthquake at Meckering, Western Australia: 14 October 1968, in "Recent Crustal Movements", Roy. Soc. N. Zealand Bull. 9: 85-93.
- Haskell, N. A. (1962). Crustal reflection of P and SV waves, J. Geophys. Res. 67: 4751-4767.
- Haskell, N. A. (1964). Radiation pattern of surface waves from point sources in a multi-layered medium, Bull. Seism. Soc. Am. 54: 377-393.
- Hudson, J. A. (1969). A quantitative evaluation of seismic signals at teleseismic distances—I. Body waves and surface waves from an extended source, Geophys. J. 18: 353-370.
- Stauder, W. (1968). Tensional character of earthquake foci beneath the Aleutian trench with relation to sea-floor spreading, J. Geophys. Res. 73: 7693-7701.

Stauder, W. (1973). Mechanism and spatial distribution of Chilean earthquakes with relation to subduction of the oceanic plate, J. Geophys. Res. 78: 5033-5061.

Stauder, W. (1975). Subduction of the Nazca plate under Peru as evidenced by focal mechanism and seismicity, J. Geophys. Res. 80: 1053-1064.

Street, R. L., R. B. Herrmann and O. W. Nuttli (1975). Spectral characteristics of the Lg wave generated by Central United States earthquakes, Geophys. J. 41: 51-63.

TABLE I
EVENT PARAMETERS

Event	Date	Origin Time	Lat (°)	Lon (°)	H(km)	M_s	m_b	Source
1.	01 Oct 65	08 52 04.4	50.1 N	178.2 E	23 5	6.0 ± 0.2 (21)	6.3 6.2 6.0 ± 0.3 (20)	CGS ISC *
2.	02 Jun 66	03 27 50.0	51.1 N	176.0 E	41 48	5.1 ± 0.2 (40)	6.0 5.8 ± 0.4 (25)	CGS ISC *
3.	07 Aug 66	02 13 04.4	50.6 N	171.3 W	39 29 22	6.2 ± 0.3 (21)	6.2 6.3 6.2 ± 0.3 (19)	CGS ISC *
4.	15 Feb 67	16 11 11.5	9.1 S	71.4 W	597 598		6.1 6.1 6.0 ± 0.4 (18)	CGS ISC *
5.	09 Sep 67	10 06 44.1	27.7 S	63.1 W	578 577		5.8 5.9 6.0 ± 0.4	CGS ISC *
6.	14 Oct 68	02 58 47.8	31.5 S	117.0 E	1 0 75	6.4 ± 0.4 (18)	6 5.8 ± 0.3 (19)	CGS ISC *
7.	11 Feb 69	22 08 54.7	41.4 N	79.3 E	33 3 14	6.2 ± 0.4 (13)	5.8 5.6 ± 0.4 (20)	CGS ISC *
8.	18 Jul 69	05 24 48.0	38.3 N	119.4 E	33 6 15	6.7 ± 0.4 (17)	6.2 5.9 6.0 ± 0.3 (20)	CGS ISC *
9.	05 Jun 70	04 53 06.4	42.5 N	78.8 E	20 24 16	6.6	5.9 6.0 ± 0.3 (20)	NOAA ISC *

TABLE I (cont)

Event	Date	Origin Time	Lat (°)	Lon (°)	H(km)	M _s	m _b	Source
10.	22 May 71	16 43 58.7	58.8 N	40.5 E	37 45 11	6.7 6.6 ± 0.3 (19)	6.0 6.0 ± 0.3 (19)	NOAA ISC *
11.	03 Sep 72	16 48 28.3	36.0 N	73.4 E	3 12	6.2 5.9 ± 0.3 (16)	6.3 6.2 6.2 ± 0.4 (18)	NOAA ISC *
12.	12 Nov 72	17 56 44.4	38.4 N	73.3 E	33 111		6.0 5.9 5.7 ± 0.4	NOAA ISC *

Source *This study

TABLE II
FOCAL MECHANISM PARAMETERS

<u>Event</u>	<u>Date</u>	<u>T Axis</u>		<u>P Axis</u>		<u>Ref.</u>
		Trend	Plunge	Trend	Plunge	
1.	01 Oct 65	182	12	66	65	Stauder (1968)
2.	02 Jun 66	223	5	353	82	Stauder (1968)
3.	02 Aug 66	331	64	200	18	Stauder (1968)
4.	15 Feb 67	257	10	77	80	
5.	09 Sep 67	263	20	64	69	
6.	14 Oct 68	27	59	271	15	
7.	11 Feb 69	235	69	342	7	Stauder (1975)
8.	18 Jul 69	186	12	91	22	Stander (1975)
9.	05 Jun 70	242	71	338	2	
10.	22 May 71	100	4	190	4	
11.	03 Sep 72	175	83	39	5	
12.	12 Nov 72	236	10	346	62	

TABLE III
GOODNESS OF FIT

Event	Date	TMAX	N	H	DT1	DT2	DT3	M ₀	r
1.	01 Oct 65				2.4	0.0	2.4	8.0 E 25	--
2.	02 Jun 66				1.3	0.0	1.3	6.0 E 24	--
3.	07 Aug 66				3.0	0.0	3.0	1.5 E 26	--
4.	15 Feb 67	30	14	600*	3.6	0.0	3.6	4.2 E 26	.9326
					0.0	5.5	0.0	4.4 E 26	.9315
5.	09 Sep 67	30	12	598*	2.0	0.0	2.0	1.8 E 26	.9078
					0.0	3.5	0.0	1.9 E 26	.9003
6.	14 Oct 68	20	15	7.5	3.0	0.0	3.0	6.0 E 25	.8812
				7.5	0.0	3.75	0.0	4.5 E 25	.8630
7.	11 Feb 69	30	14	14.0	3.1	0.0	3.1	2.2 E 25	.8600
				10.0	0.0	4.75	0.0	2.2 E 25	.8465
8.	18 Jul 69	15	15	14.0	4.1	0.0	4.1	2.0 E 26	.8886
				16.0	0.0	6.0	0.0	2.0 E 26	.8819
9.	05 Jun 70	30	16	13.0	3.7	0.0	3.7	6.0 E 26	.9041
				13.0	0.0	6.0	0.0	6.0 E 26	.8947
10.	22 May 71	15	12	9.5	3.0	0.0	3.0	1.2 E 26	.9125
				9.5	0.0	4.0	0.0	1.2 E 26	.8867
11.	03 Sep 72	30	14	11.0	2.0	0.0	2.0	1.7 E 25	.8728
				11.0	0.0	3.0	0.0	1.7 E 25	.8971
12.	12 Nov 72	15	13	125*	1.8	0.0	1.8	5.0 E 25	.9233
					0.0	3.0	0.0	5.0 E 25	.9293

TABLE IV

S (1 Hz) SPECTRAL ESTIMATES

Event	Date	<u>Triangular Impulse</u>			<u>Rectangular Impulse</u>		
		M ₀ dyne-cm	T ₀₂ sec.	S (1 Hz)	M ₀ dyne-cm	T ₀₂ sec.	S (1 Hz)
1.	01 Oct 65	8.0 E 25	7.5	1.4 E 24			
2.	02 Jun 66	6.0 E 24	4.1	3.6 E 23			
3.	07 Aug 66	1.5 E 26	9.4	1.7 E 24			
4.	15 Feb 67	4.2 E 26	11.3	3.3 E 24	4.4 E 26	17.3	2.5 E 25
5.	09 Sep 67	1.8 E 26	6.3	4.5 E 24	1.9 E 26	11.0	1.7 E 25
6.	14 Oct 68	5.0 E 25	9.4	5.7 E 23	4.5 E 25	11.8	3.8 E 24
7.	11 Feb 69	2.2 E 25	9.7	2.3 E 23	2.2 E 25	14.9	1.5 E 24
8.	18 Jul 69	2.0 E 26	12.9	1.2 E 26	2.0 E 26	18.8	1.1 E 25
9.	05 Jun 70	6.0 E 25	11.6	4.4 E 23	6.0 E 26	18.8	3.2 E 24
10.	22 May 71	1.2 E 26	9.4	1.4 E 24	1.2 E 26	12.6	9.5 E 24
11.	03 Sep 72	1.7 E 25	6.3	4.3 E 23	1.7 E 25	9.4	1.8 E 24
12.	12 Nov 72	6.0 E 25	5.7	1.9 E 24	6.0 E 25	9.4	6.4 E 24

Figure Captions

Figure 3.1: Focal mechanism solutions made as part of this study. The source parameters are given in Tables I and II.

Figure 3.2: Plot of seismic moment M_0 versus m_b . The numbers refer to the event list of Tables I and III. The standard deviations on the M_s values are also given.

Figure 3.3: Plot of spectral level at 1 Hz versus m_b for two assumptions of the shape of the source pulse for body waves--rectangular (open triangles) and isosceles triangular (closed circles). Standard deviations on m_b also are given.

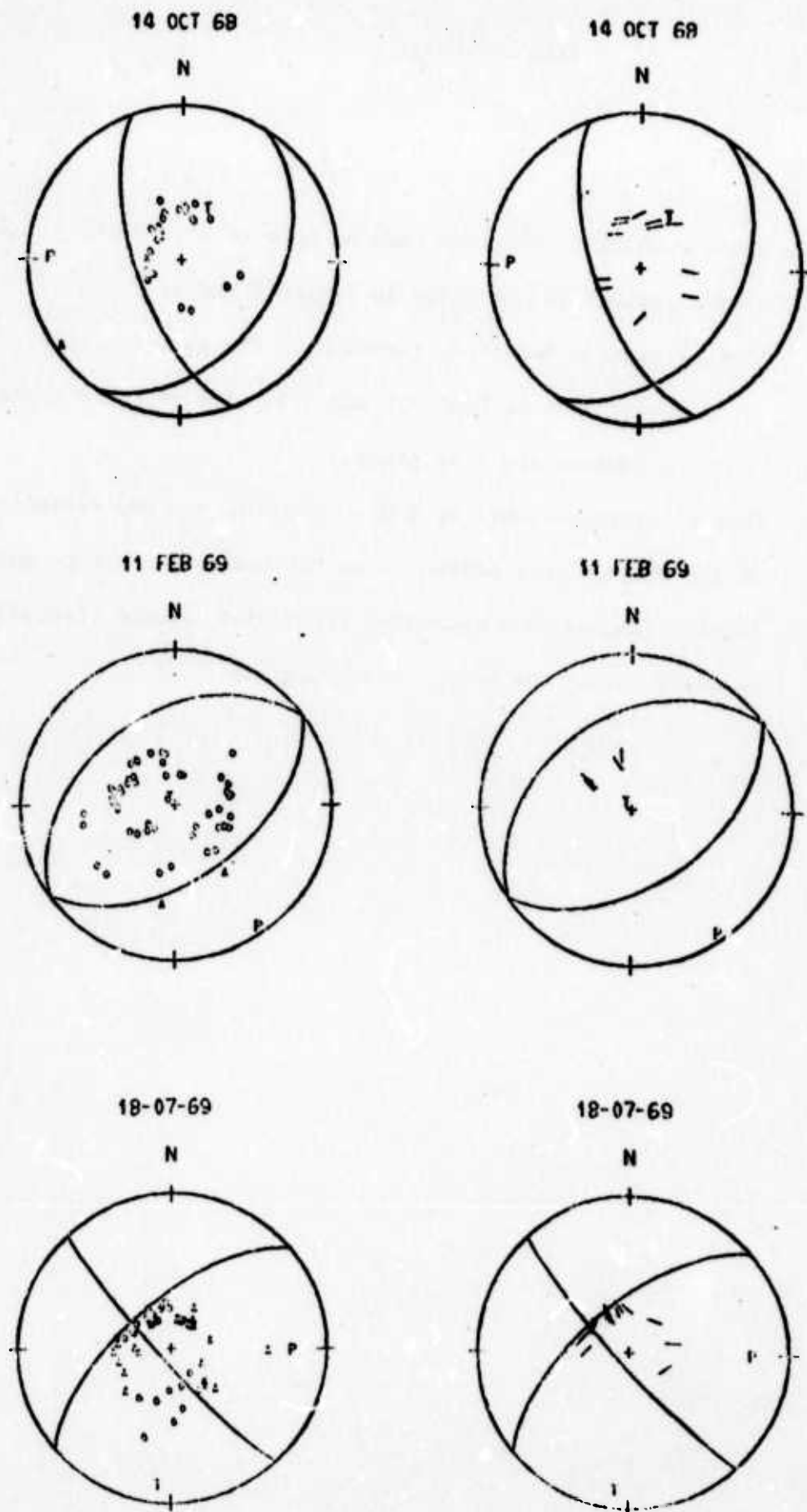


Figure 3.1

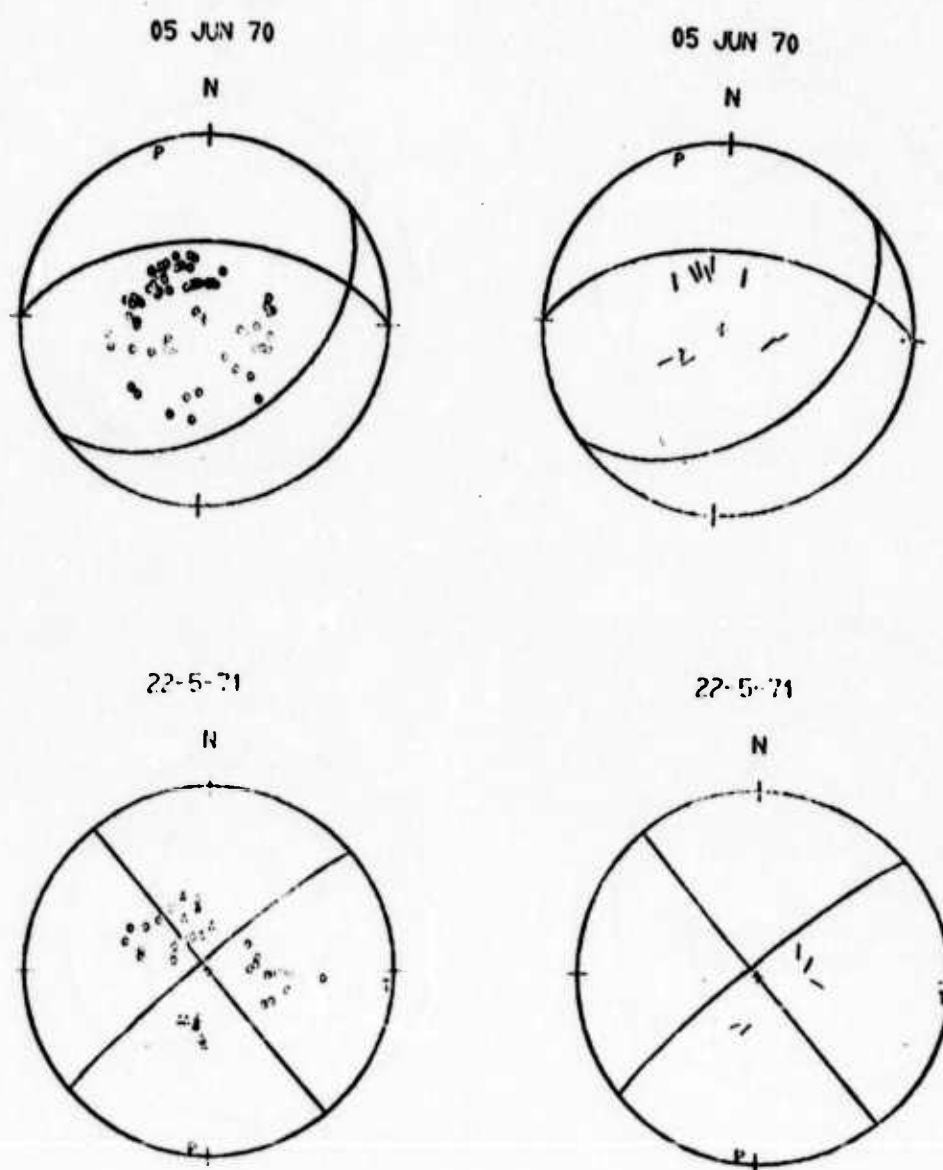


Figure 3.1

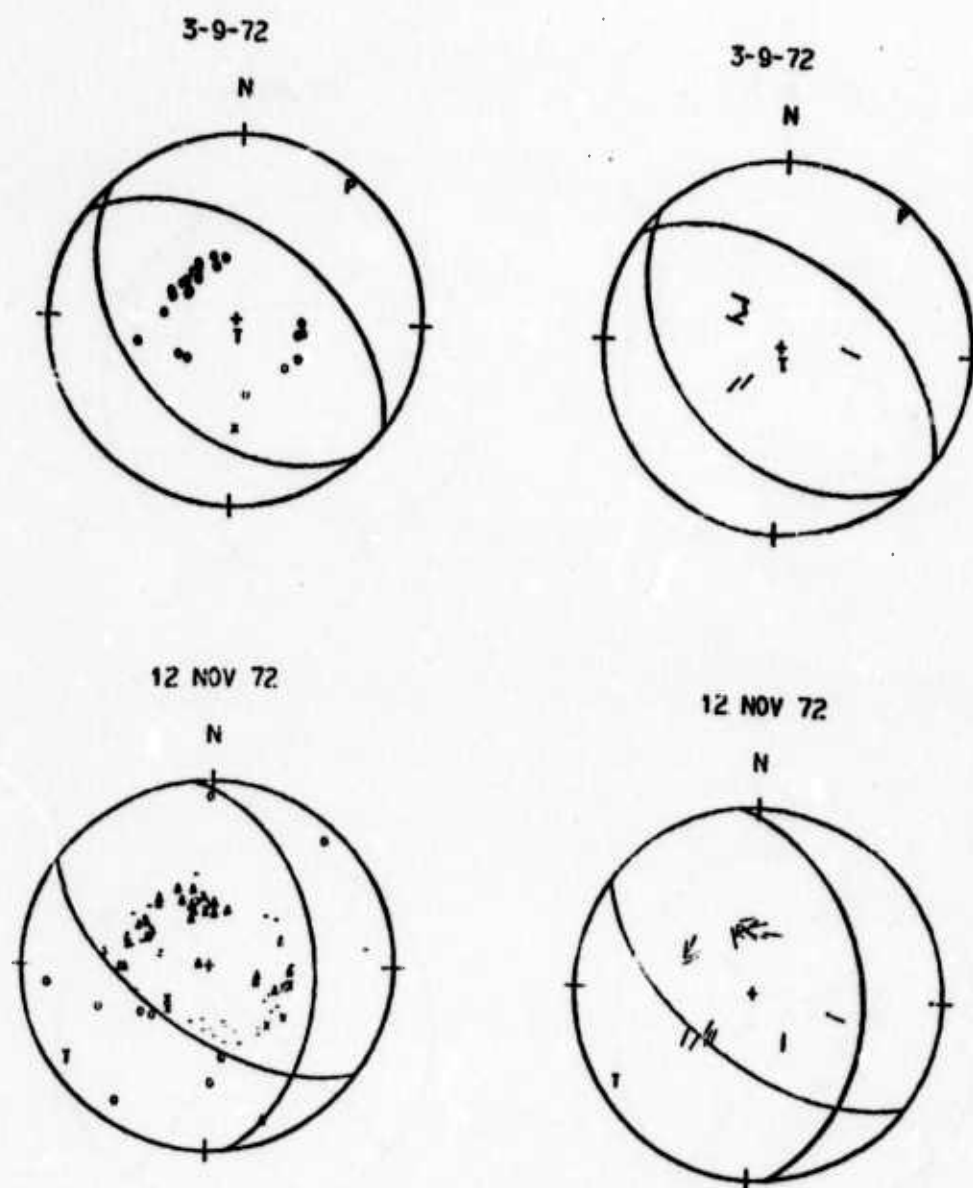


Figure 3.1

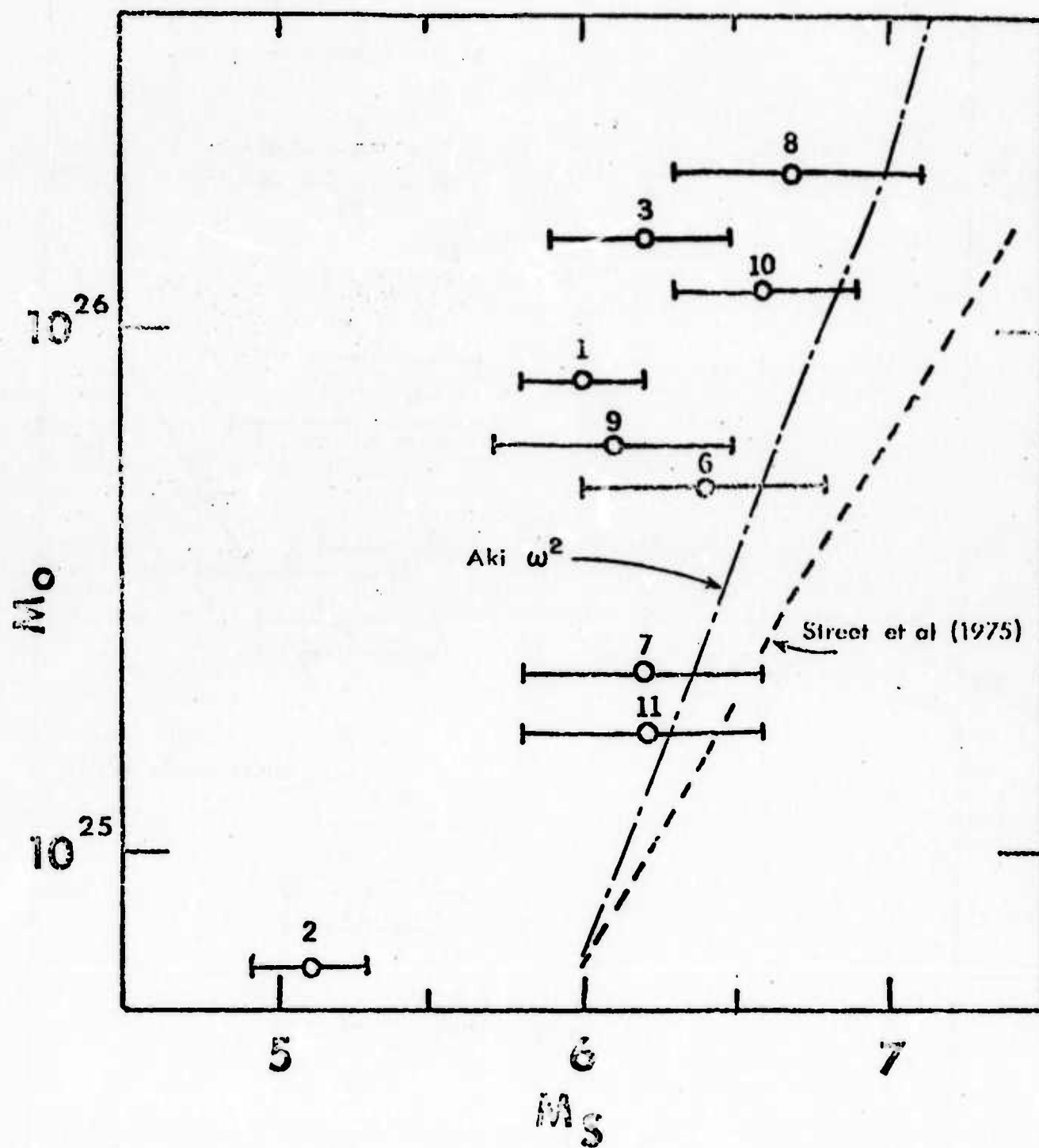


Figure 3.2

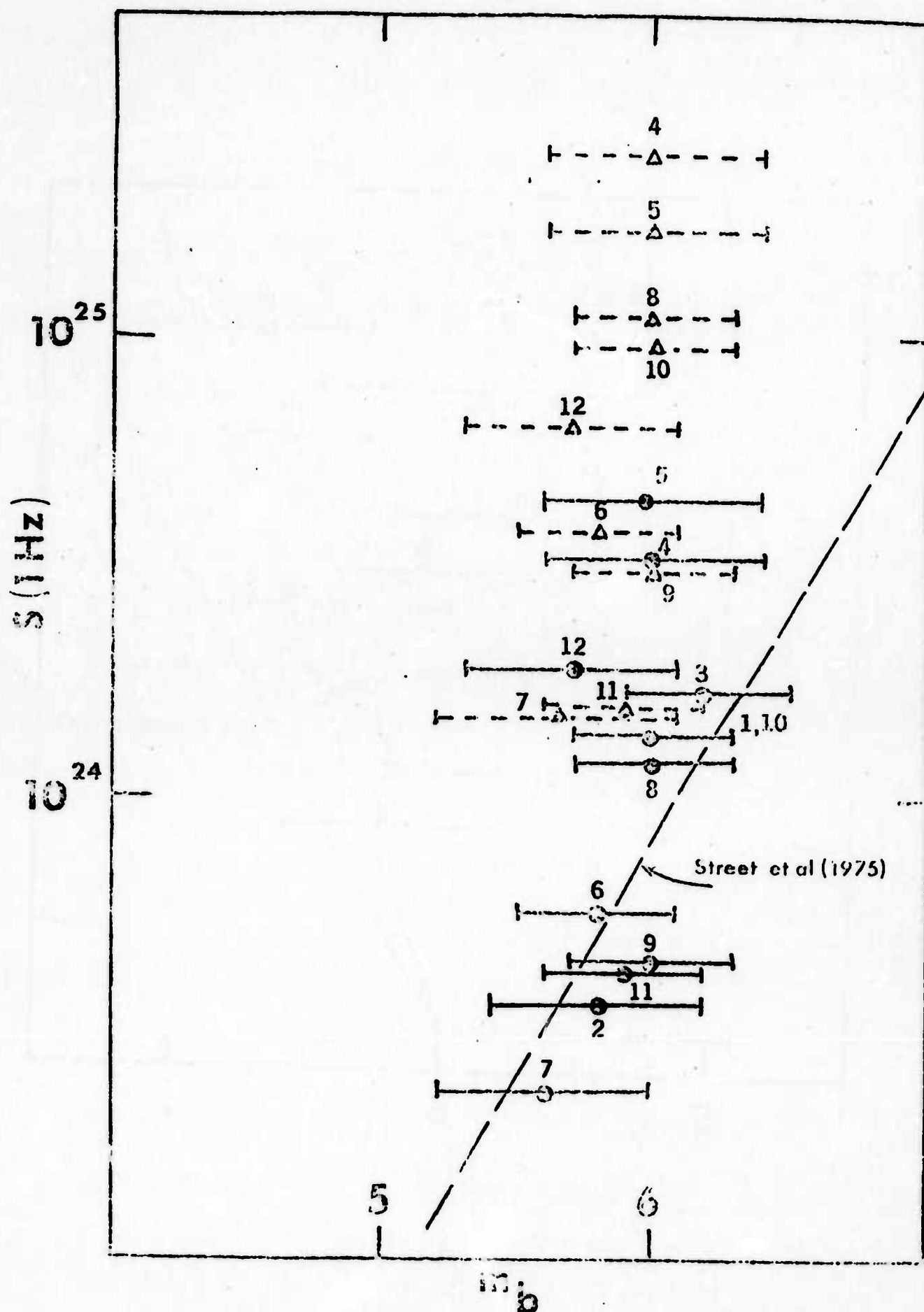


Figure 3.3

4. Computation of the Source Spectrum from a Crustal Earthquake

Gary Lundquist

Introduction

We showed in the last semi-annual technical report that estimation of the power spectrum by taking the Fourier Transform of the autocorrelation was less noisy and therefore a more desirable estimation than direct application of the FFT algorithm. We continue that analysis here with the objective of formulating a practical algorithm for computing seismic source spectra.

This study is divided into two parts. In the first part, we extend the autocorrelation technique for power spectral estimation to the estimation of seismogram amplitude spectra. In particular, we examine windowing techniques which smooth the spectrum.

In the second part, we review geophysical corrections to the seismogram spectrum. In part, the objective is to understand the inherent difficulties in dealing with crustal events for which surface reflections and multiple crustal reverberations are part of the P or S wave. We also examine anelastic attenuation, because the final spectrum depends critically upon the model used.

Practical Application of the Autocorrelation Technique to Estimation of Seismogram Spectra

Power spectral estimation from the autospectrum requires specification of the following values.

1. Total data length
 - a. Choice of first and last points
 - b. Choice of sample interval
 - c. Method of truncating the raw data

2. Total autocorrelation length

- a. Number of autocorrelation lags to be used in transform
- b. Method of truncating the autocorrelation

We will test various choices of these parameters on the filtered δ_k sequence and on seismograms for the Tien Shan earthquake of June 5, 1970. The tests will be conducted in the context of the general flow diagram for autospectral estimation given in Figure 4.1.

Data Length Tests

We will commence the estimation of autospectra with raw data consisting of nonuniformly sampled seismograms. The specification of first and last points must be based upon the geophysics, and will not be discussed here. Yet, given a set of points to be analyzed, we must consider how we remove those points from the rest of the data sequence.

A simple test verifies that truncating the data sequence off the zero line introduces high frequency noise into the autospectrum, and a sharper truncation creates a greater increase in high frequency. Since we can decrease the high frequency content by increasing record length, this behavior is certainly related to truncation and not to data length.

We cannot apply a smooth data window to the raw data without seriously distorting, for instance, an impulsive P wave; so we use the following method. Given a start time, we search back in time for the first zero crossing and interpolate a point at zero amplitude. That point, then, is the first point of the sequence to be transformed, and we may interpolate a uniformly sampled sequence considering the zero crossing to be at time zero. The end of the truncated sequence may be specified by desired time length or by end time. In either case, we can apply a taper to the last few points rather than searching for another

zero crossing. Testing shows that a Gaussian taper applied to the last ten points of the interpolated sequence effectively eliminates the effect of truncating off the zero line. To summarize, we apply a rectangular data window from a point interpolated at a zero crossing to a point a specified length away, then we taper the end of the data smoothly to zero, leaving the data virtually undistorted.

We specify the sample interval, Δt , according to the frequencies we want to resolve. Sample theorem gives

$$f_{\text{Nyquist}} = \frac{1}{2\Delta t}$$

where the Nyquist frequency is the highest frequency of interest. For the case of seismograms, the choice of frequencies has been made for us in the design of the seismograph systems. The systems are bandpass filters with half power points (0.707 amplitude) at 1.1 and 2.5 Hz for WSSN short period and 0.035 to 0.19 Hz for long period (15 - 100 system). A more conservative bandwidth for the choice of sample interval is the 0.1 amplitude point, 0.5 to 7.5 Hz for short period and 0.009 to 1.0 Hz for long period. Thus sample intervals of 0.067 and 0.5 sec are adequate.

We note that the only result of oversampling is the extension of the Nyquist frequency. We get no more detail in the pass band of the instrument, but halving the sample interval doubles the number of frequencies in the spectrum, and all of the extra points sample frequencies which are above the old Nyquist frequency. Thus oversampling costs money to produce points in frequency which we would ignore anyway for being well outside the passband of the instrument.

Lag Window Comparisons

Standard methods of spectral estimation from the autocorrelation use a window to limit the number of autocorrelation lags used in the Fourier transform. Given a specific autocorrelation, we have two parameters to vary: the window length and the shape of the window. Of course the autospectrum and the periodogram are identical if we use the maximum autocorrelation lag length; so we must show that the spectrum is improved by windowing.

We will consider five lag windows defined as follows:

$$\text{Rectangular} \quad g_r(k) = \begin{cases} 1, & |k| \leq \frac{L}{2} \\ 0, & |k| > \frac{L}{2} \end{cases}$$

where L is the window length.

$$\text{Hanning (or Tukey)} \quad g_H(k) = \begin{cases} \frac{1}{2} + \frac{1}{2} \cos \frac{2\pi k}{L}, & |k| \leq \frac{L}{2} \\ 0, & |k| > \frac{L}{2} \end{cases}$$

$$\text{Hamming} \quad g_h(k) = \begin{cases} 0.54 + 0.46 \cos \frac{2\pi k}{L}, & |k| \leq \frac{L}{2} \\ 0, & |k| > \frac{L}{2} \end{cases}$$

$$\text{Bartlett} \quad g_b(k) = \begin{cases} 1 - \frac{2|k|}{L}, & |k| \leq \frac{L}{2} \\ 0, & |k| > \frac{L}{2} \end{cases}$$

$$\text{Gaussian} \quad g_g(k) = \begin{cases} \exp - \frac{k^2 \tan^2(\frac{\omega}{2})}{2}, & |k| \leq \frac{L}{2} \\ 0, & |k| > \frac{L}{2} \end{cases}$$

The rectangular and Gaussian windows are endforms of a series of windows obtained by convolving the rectangular window with itself. The Bartlett or triangular window results from one convolution, and a Parzen window can be defined as the result of four convolutions. As the number of convolutions increases, the central limit theorem requires the resulting curves to approach the Normal or Gaussian curve.

The transform of the rectangular window is a function of the form $\sin x/x$, sometimes called a sinc function or the Dirichlet kernel. The transform of the Hanning window is a linear sum of shifted Dirichlet kernels because modulation by a cosine function is equivalent to a frequency shift.

$$K_N^H(\omega) = \frac{1}{2} D_N(\omega) + \frac{1}{4} D_N\left(\omega - \frac{\pi}{L}\right) + \frac{1}{4} D_N\left(\omega + \frac{\pi}{L}\right)$$

where $D_N(\omega)$ is the Dirichlet kernel of an $N = L - 1$ point sequence. The Blackman window adds a term in $\cos \frac{4\pi k}{L}$, and a generalized Dirichlet combination may be formed as

$$g_m(k) = \sum_{n=0}^m A_n \cos \frac{2\pi nk}{L}, \quad |k| \leq L$$

Figure 4.2 compares the various window shapes tested for this study.

The truncation of the autocorrelation in time by a window is equivalent to convolution in the frequency domain of the complete autospectrum with the transform of the window function. A desirable window is one which truncates the autocorrelation function smoothly and provides adequate noise reduction in the autospectrum.

The rectangular window has a frequency domain character which depends upon the window length relative to a power of two. To an FFT algorithm a rectangular window of length equal to a power of two looks like an infinite sequence of 1's, and the transform is correspondingly a spike at zero frequency. The effect is no smoothing and a noisy auto-spectrum. If the length is one less than a power of two, the window appears to be the sum of a constant and a spike of amplitude minus one. The result in frequency is the sum of a spike at D.C. and a constant amplitude spectrum. For any other length, the rectangular window transforms to a sinc function as predicted by continuous transform theory. Depending upon the window length and the smoothness of the true spectrum, the odd length, one less than a power of two, is likely to give a rectangular window frequency response much better than other lengths which give a sinc function response.

The Hanning window also transforms differently for different lengths. In particular, the Hanning window is optimized if the lag length is one less than a power of two. For that case, only the first two frequency domain points have any power, as all other samples have amplitudes below 10^{-26} . Considering the symmetry of the Fourier transform, we see that this means the Hanning smoothing is a 3 point weighted running average. In terms of application, this suggests we compute the autocorrelation to lag length equal to a power of two. Then upon folding (see Figure 4.1), we have a length one less than the next power of 2 and we get the optimum Hanning response.

The Hamming window is very similar to the Hanning except for the special length cases. In general, it shows higher resolution but a slower decay rate. For the length one less than a power of two, the Hamming response is similar to that of a rectangular window in that it attains a finite value and remains constant.

The response for the Bartlett window has been examined and does not have any particular advantages.

The Gaussian window differs from the Hanning type in that it has no reference to window length in its formula and that it depends on a parameter ω which relates to the width of the window. The Hanning window for 256 points is just a scaled up version of the 64 point Hanning window. The Gaussian window, on the other hand, uses exactly the same amplitudes in each window (for constant ω) as far as the lengths allow. Thus, by going 96 points beyond the 32 point cutoff for a 64 point window, the 256 point Gaussian window ($\omega = 0.07$) attains amplitudes as low as 0.00005 and smooths the last 40 points quite severely. Obviously the "width" parameter, ω , must be varied with the lag length to get equivalent responses for different window lengths. For ω very small (0.067 for $L = 64$) the Gaussian window approximates a rectangular window, but as ω increases, the window becomes narrower and more bell shaped.

The next step in evaluating the windows is to apply them to a signal with a known spectrum, in this case the frequency response of a Butterworth lowpass filter. The theoretical spectrum (periodogram) is characterized by a continuous and rapid rolloff beyond the cutoff frequency at 0.2 Hz. Each of the autospectra, however, shows a lower limit to the decay. In this context, a good window is one which yields an autospectrum which is a

close approximation to the theoretical spectrum. Such a window minimizes the amplitude of the noise which interrupts the high frequency rolloff and one which gives the theoretical decay rate down to its noise limit.

Both the periodogram and the Dirichlet smoothed autospectrum decay to 10^{-5} at 0.3 Hz, so the second criterion is satisfied. However, the decay fails to continue after 0.32 Hz, and the final level at 0.5 Hz is 3×10^{-7} . Applying a Hanning window maintains the character of the rolloff to 0.4 Hz, and gives a final level of 8×10^{-10} , or 2 1/2 orders of magnitude better. The Hamming gives a higher noise level than the Hanning, and is only slightly better than the rectangular window for window length equal to a power of two.

For a fixed window length, the Gaussian smoothed autospectra depend on ω . For small ω the response is that given by a rectangular window, with correct rolloff but high noise level. As ω increases, the noise level decreases, but the rolloff is distorted. Thus, at $\omega = 0.32$, the noise level is lower than that for the Hanning window, but the level 10^{-5} is not reached until after 0.32 Hz, and for ω larger than 0.2, the distortion of the slope is unacceptably poor.

The Bartlett window has an unacceptably high noise level.

The observations made so far apply to an extremely simple ideal spectrum, and we found the Hanning window to be the best. We now form a window comparison test for earthquake seismograms. Figure 4.3 shows the smoothed levels of the autospectra relative to the periodogram for BAG LPZ and BAG SPZ for the event of June 5, 1970. The conclusion for the long period test is obvious. The Hanning window has the lowest noise

level and its slope follows the periodogram nicely. Also, though not shown in this figure, the Hanning smoothed autospectrum has the definite appearance of a spectrum, while the rectangular and Hamming spectra are dominated by window noise. The Gaussian spectra ($\omega = 0.101$) is smoother than the Hanning, but it does not have the correct slope in the range 0.15 - 0.3 Hz.

The short period comparison is not so easily analyzed. The Hanning, Hamming, Gaussian ($\omega = 0.081$) and Bartlett windows all give nearly equivalent responses. The Hanning spectrum has a more nearly correct decay rate, while the Hamming has slightly more resolution. Since the long period data so clearly favors the Hanning window, we will use the Hanning window in all further tests.

Window Closing Tests

We can define the bandwidth of a lag window in several ways. In terms of filter theory, the bandwidth is the distance between half power points. In statistical applications, the bandwidth may be defined as the width of a rectangular window with the same variance. But whatever definition we use, there is an inverse relationship between window length in time and bandwidth in frequency. In a window closing test, we compute smoothed spectral estimates for increasingly wide time-domain windows, effectively closing the frequency-domain window. If we visualize the convolution process in frequency as a weighted running average, then it is obvious that a narrower bandwidth will resolve more of the detail in the original spectrum. Thus, as we increase the number of lags used, we improve the resolution in frequency until, in the limit, we obtain the

periodogram. Looking at it another way, as the bandwidth decreases, the spectral estimate is a polynomial of increasingly high degree in $\cos 2\pi f$, so it is easy to produce spurious peaks.

The question we must answer here is when to stop the process of narrowing the bandwidth. The answer will depend upon experience, the amount of detail desired, and personal preference. Sometimes the spectrum may be stable, in which case all of the detail will appear and decreasing bandwidth will resolve nothing more. But more often the spectrum will become unstable and noise will begin to mask significant detail. The theoretical filter response (a filtered δ_k sequence) is a member of the first class, and seismograms belong to the second class.

In Figure 4.4 we show the window closing experiment for our BAG SPZ seismogram in terms of amplitude spectra. The number of lags varies from 5% of the sequence length at the bottom to 25% at the top. The Fourier amplitude spectrum is shown at the top for comparison. An overlay would show that the slope and levels are defined for the 5% case, and further lag length only adds detail to the spectrum. As mentioned, the amount of detail (or noise) which is desirable is a matter of personal preference. We find 20% of the sequence length to be a maximum and 10% to be preferable. For shorter time sequences, though, a longer transform length contributes to the smoothness of the spectrum, so we will compromise. For short period seismograms we will use 15% of the complete autocorrelation length in computation of the autospectrum.

Figure 4.5 shows the amplitude autospectra of the window closing experiment on BAG LPZ. Once again, a 20% lag length provides the basic spectral shape for the frequencies above 1 Hz, but for the frequencies below 1 Hz, we must consider the autospectrum technique in more detail.

The autocorrelation function has the following properties: it is real and has even symmetry; its maximum occurs at zero lag; it contains no information on phase relationships; and it contains the same amplitude information as the original signal. If a periodicity is present in the time sequence, it is present with the same amplitude but zero phase in the autocorrelation. This last property implies that resolution of long periods requires a long length of autocorrelation. Resolution of a 30 sec periodicity requires 30 sec of lag.

Going back to the long period window closing test, we note that the 20% lag length resolves a maximum periodicity of 19.2 sec, or 0.052 Hz, for a data length of 320 points, while the 40% lag length resolves 47 sec. Thus the apparent improvement in resolution of the peaked character is real, and very important. We must compromise between the smoothness of the spectrum and resolution of low frequencies. In our opinion, no significant detail is resolved for lag lengths greater than 40%, and the noise level is still acceptable at 40% for this particular earthquake. However, an unavoidable conclusion is that the best seismic spectra will require a window closing experiment for the long period autospectra of each individual earthquake.

Discussion

We have examined the practical problems of estimating seismic source spectra up to the point of applying instrument response and attenuation corrections. We have chosen a rectangular data window with a short taper at the end, and we found the Hanning window to be the best of the lag windows. The long and short period sample intervals should be less than 0.5 and 0.06 sec, respectively, and the lag length should be near

40% of the data length for long period records and 15% for short period records. Finally, although we cannot specify the data lengths, experience has shown us that we need short-period data lengths of 15 to 60 sec and long-period data lengths of 40 to 180 sec.

The flow diagram in Figure 4.1 gives the steps required to obtain power autospectra. The amplitude autospectra are obtained by simply taking the square root of each frequency sample multiplied by the number of samples in the autocorrelation, then multiplying by the sample interval.

The results of our tests demonstrate that we can obtain less noisy and thus more reliably interpreted seismic spectra using the autocorrelation technique.

Geophysical Corrections to Seismogram Spectra

The computation of a seismic source spectrum from the estimates of seismogram spectra at several stations requires that a number of corrections be applied. We shall refer to a spectrum which has been corrected for instrument response as a station spectrum. The corrections which must be applied to station spectra to obtain a source spectrum are intended to invert the transmission filter in the Earth. As a first approximation, we may write the station spectrum of a body wave as the product in frequency of independent effects of the source spectrum $F(\omega)$ with transfer functions of the source directivity function, or radiation pattern, $R(\theta)$, source crustal response, $C_s(i_o, \omega)$, geometric spreading, $G(\Delta)$, anelastic attenuation, $Q(\Delta, \omega)$, and receiver crustal response, $C_R(i_h, \omega)$. Here Δ is distance measured in degrees of central angle subtended by the ray; θ is azimuth, i_o is take-off angle from the source, and i_h is incident angle at the base of the receiver crust. That is

$$D(\omega, \Delta, \theta) = F(\omega) \cdot R(\theta) \cdot C_s(i_o, \omega) \cdot G(\Delta) \cdot Q(\Delta, \omega) \cdot C_R(i_h, \omega) \quad (B1)$$

where D is the station spectrum or ground displacement spectrum. Since the object is the source spectrum F , we must consider correcting for each of the contributions to the Earth filter.

Source Crust

We will find the evaluation of the source crustal response to be simpler if we consider constructing a synthetic seismogram from the multiple contributions of waves reflected internally in the crust, rather than trying to decompose an observed seismogram. A critical point in this entire study is that we are dealing with crustal events for which the

observed P wave is not isolated from surface reflections or multiple reverberations in the source crust.

In a separate part of this study, Herrmann (1975) succeeded in synthesizing long-period P-wave seismograms of crustal events. To do so, he used the four basic waves which can contribute to the teleseismic P wave and added 31 additional waves from crustal reverberations near the source. In Figure 4.6 we show the shapes and relative amplitudes of the contributions of those four waves and their individual reverberations to the synthetic seismogram of a purely strike-slip source at a station with relative azimuth of 40° and distance of 45° . The downgoing P, or direct P wave is reflected at the crust-mantle boundary, producing upgoing P and SV waves. Each of those are reflected at the surface with twofold conversion, and so on. The signal pictured in Figure 4.6 is the contribution at the receiver of this sequence of waves. Similarly, the contributions from upgoing P wave (pP) and up and downgoing SV (sP and S_mP) are presented.

The obvious feature is the much larger amplitude of sP relative to P. If the source radiated equal P and SV energy, theoretical reflection and transmission coefficients would give a P amplitude at this particular receiver more than three times as large as the sP amplitude. The observed amplitude ratio results from the efficiency of a shear dislocation in radiating shear energy. Of course the observed amplitude ratio will vary from zero to infinity depending upon station location and focal mechanism. But over most of the focal sphere the contribution to the P-wave seismogram of a crustal event from the upgoing SV will be greater than or equal to the contribution from the direct P. In other words, if we ignore the interference phenomenon for a moment, the response of the source crust is

to increase the apparent spectral level, by a factor depending upon focal mechanism, over the level we would measure for an isolated P-wave.

The question we must answer is whether we can correct for the source crustal response. This leads us to consider the interference of the four wave types. Interference depends upon relative time delays which are functions of crustal thickness and source depths, rather than focal mechanisms.

The contribution of each wave type may be written as a sum of reflected and refracted components

$$f(t) = \sum_{i=1}^N a_i f_a(t - \tau_i) \quad (1)$$

where $f_a(t)$ is the source-time function for the particular wave type being modelled; the a_i are amplitudes determined by reflection and refraction coefficients and by the radiation pattern, and the τ_i are delay time associated with the individual components. We can sum over the four wave types and compute the spectrum of the total. That is, if

$$f(\omega) = \int_{-\infty}^{\infty} f(t) e^{-j\omega t} dt$$

then

$$F_T(\omega) = \int_{-\infty}^{\infty} \left\{ \sum_{i=1}^{N_a} a_i f_a(t - \tau_i) + \sum_{k=1}^{N_b} b_k f_b(t - \tau_k) + \sum_{\ell=1}^{N_c} c_\ell f_c(t - \tau_\ell) + \sum_{m=1}^{N_d} d_m f_d(t - \tau_m) \right\} e^{-j\omega t} dt \quad (2)$$

where $f_a(t)$ is the source-time function for downgoing P waves; f_b corresponds to upgoing P waves, and f_c and f_d to upgoing and downgoing S waves, respectively. We may simplify (2) by making assumptions about these source time functions. If we neglect rupture effects, then we may assume $f_a(t) = f_b(t) = f_p(t)$, and $f_c(t) = f_d(t) = f_s(t)$. Further, if we model the source as a double couple point source, then $f_p(t) = f_s(t) = f(t)$. In that case

$$\begin{aligned}
 F_T(\omega) &= \int_{-\infty}^{\infty} \sum_n a_n f(t - \tau_n) e^{-i\omega t} dt \\
 &= \sum_n a_n \int_{-\infty}^{\infty} f(t - \tau_n) e^{-i\omega t} dt \\
 &= F(\omega) \sum_n a_n e^{i\omega \tau_n}
 \end{aligned} \tag{3}$$

where the range of n includes all of the possible contributions.

We can see from (3) that the long-period ($\omega=0$) level of the total spectrum is just the sum of the levels of the spectra of the individual contributions. Thus the computation of seismic moment is seriously affected if we can actually estimate the DC term in the spectrum. For any other frequency, the spectral level depends upon the interference of the sinusoidal modulation caused by the delay. Thus we cannot remove the effect of the source crust in any simple manner. The only technique which seems possible is Herrmann's method of modelling the P wave in the time domain as a sum of waves. Once a fit has been achieved, then one possible form of the contribution of any individual wave is known.

It is appropriate to note here that we should not arbitrarily assume that P and S wave source-time functions are the same. If they differ, then the total DC level still varies as a sum of DC levels. However, if P and S corner frequencies differ, then a corner frequency of the total spectrum should reflect that difference, for a crustal event, by being more rounded or perhaps two cornered, rather than being a single sharp bend.

To summarize briefly, we should expect the spectrum of a P wave generated by a crustal source to have a higher long period level than that generated by the same focal mechanism at depth. We should expect such a spectrum to show the interference of all of the crustal reverberations and in particular, of the direct P and the sP. This effect is to apply a sinusoidal modulation to the sum of the separate spectra and is an effect not simply removed. And finally, if the source time functions of the various contributions are all identical, we should expect any corners in the spectrum to be sharp and well resolved. If such corners are rounded or poorly resolved, it may be evidence that the source does not appear exactly the same to an S wave as it does to a P wave.

Radiation Pattern

In the last section we showed that the contribution from the four wave types could not be separated by decomposition of observed teleseismic ground motion due to a crustal earthquake. Thus the question of application of a radiation pattern correction to such a record reduces to the question of whether or not we may apply one correction for all contributions to the P wave. The answer is obviously no. In general the downgoing P and the upgoing SV will sample different radiation patterns, and we cannot expect to correct the entire teleseismic P wave

by radiation pattern computed for P alone.

We can partially correct for radiation pattern by averaging, but even a perfect average of a radiation pattern of maximum amplitude of one is not equal to one. If we assume a perfect average, then we should correct the P wave by $1/0.424$ and the S wave by $1/0.593$.

Attenuation

We can separate amplitude loss along the transmission path into a frequency dependent part, the anelastic attenuation, and a frequency independent part, the geometric attenuation, or spreading. In the computation of earthquake magnitudes we use Gutenberg and Richter's (1956) \bar{Q} to correct for both types of attenuation, assuming no frequency dependence. For the correction of spectra, however, we must apply separate factors.

We take our geometric attenuation correction from Duda (1971). He notes that a basic failing of strictly empirical attenuation factors is the inability to relate amplitudes of earthquakes from different depths. He then evaluates Bullen's (1953) equation for amplitude as a function of distance in a spherically symmetric Earth. The travel path is defined by ray theory and by the velocity structure of Herrin et al. (1968). In this model, no velocity inversions are allowed, and the resulting corrections for distance and depth are much smoother than Richter's. Nuttli (1972) computed geometric attenuation empirically, using nuclear explosion sources. In his comparisons, Nuttli found his and Duda's curves to be very similar in the distance range $25^\circ - 95^\circ$, and concluded both curves were preferable to Richter's \bar{Q} for magnitude determination.

The model for anelastic attenuation is more involved. In a linear, perfectly elastic medium, the amplitude of a propagating stress wave is

$$Ae^{i(kr - \omega t)} \quad (4)$$

where A is amplitude and r is distance from the source. If the medium is linear, but viscoelastic, then the wave number, k , may be considered complex. Thus, while there is no absorption in an elastic medium, the amplitude in a viscoelastic medium damps according to

$$Ae^{-\gamma r + i(kr - \omega t)}$$

where k is the real part and γ the imaginary part, respectively of the complex wave number. γ is called the spatial attenuation coefficient and is defined by (Nuttli, 1973)

$$\gamma = \frac{\pi}{QVP} = \frac{\pi f}{QV} = \frac{\omega}{2QV} \quad (5)$$

where Q is the dimensionless quality factor which describes the fractional elastic energy dissipated per cycle, V is the wave velocity, f is frequency and P is period. A region of high Q is a region of low attenuation, and a low Q region absorbs relatively more energy from the passing wave.

Since Q is a per cycle characterization of absorption, it is convenient to integrate Q along the ray path, C .

$$\begin{aligned} \int_C \gamma dC &= \int_C \frac{\omega}{2QV} dC \\ &= \frac{\omega}{2} \int_C \frac{1}{Q} \frac{dt}{dC} dC \\ &= \frac{\omega}{2} \int_{\text{travel time}} \frac{1}{Q} dt \end{aligned} \quad (6)$$

Then the total Q -type attenuation along the ray path is given by

$$e^{-\omega \int \frac{dt}{2Q}} = e^{-\frac{\omega T}{2Q_{\text{eff}}}} \quad (7)$$

The numerical integration requires a velocity model to obtain the travel time, T , and a Q model to obtain the effective Q , Q_{eff} . We have also assumed Q to be independent of frequency. That is, the integration is performed by finding the number of cycles (using travel-time and velocity), and then summing the same Q for each cycle, regardless of wavelength or frequency.

Currently used Q models show a zone of high Q , the lithosphere, overlying a region of low Q , the asthenosphere, which in turn overlies the rest of the mantle which is also a high Q region. Most of the attenuation of seismic waves appears to take place in the asthenosphere. The result of the absorption being concentrated in a thin zone is that total absorption as a function of distance is nearly constant because for all teleseismic distances, all rays spend nearly equal times in the asthenosphere. The mantle below the asthenosphere is approximately non-absorbing, with Q large and increasing with depth. This accounts for the observation that the ratio T/Q_{eff} is nearly constant with respect to epicentral distance, though travel time and effective Q increase. The commonly observed ratio for P waves is $T/Q_{\text{eff}} = 1.0$, and Anderson et al. (1965) show that the ratio of Q for S waves to Q for P waves should be 2.25, by requiring density to be real and by ignoring losses due to imperfect inertia.

Solomon (1971) has reviewed and supplemented a large body of evidence for lateral variation of Q , and moreover, he presents evidence in

favor of a Q model which depends upon frequency. This is in agreement with Tsai and Aki (1969) who found a Q model derived from surface waves to be unacceptable for correcting high frequency ($f > .1$ Hz) waves.

The mechanism proposed by Solomon for anelastic attenuation is viscous damping in thin films of fluid in a partially molten asthenosphere. We can visualize such a medium as a concentration of dislocations, each capable of moving under an applied stress. In such a medium, the shear modulus is also a function of frequency. Very little energy is required to force long period relative motions of particles when the grains are lubricated by a partial melt. That is, the shear modulus is very low and little energy is absorbed by the medium. At very high frequencies, the viscosity is such that the medium absorbs very little energy because the effective stiffness is very high. At some intermediate frequency, the energy absorption is a maximum, and we can refer to the behavior in the neighborhood of this frequency as a relaxation. That is, the medium achieves a new equilibrium under an applied stress in a relaxation time, τ , characteristic of the medium. When $\tau = 1/\omega$, then the energy absorbed by the medium is maximum, and Q is a minimum. Since the loss is in shear, this model agrees with the relatively larger attenuation of S waves versus P waves.

The functional dependence of Q on frequency caused by a particular relaxation phenomenon is given by

$$\frac{1}{Q} = \frac{\Delta\mu}{(1 - \Delta\mu)^{1/2}} \frac{\omega \tau}{1 + (\omega\tau)^2} \quad (8)$$

where $\Delta\mu$ is the change in the shear modulus. A graph of this function is a bell shaped curve with $1/Q$ a maximum at $\omega\tau = 1$. Liu and Archambeau (1975) found a Solomon type model to be the best of those tested against observed attenuation of free oscillation data.

We can rewrite our definition of γ with a frequency dependent Q ,

$$\gamma = -\omega \int \frac{dt}{2Q(t, f)} \quad (9)$$

The prospect of computing a separate Q_{eff} for each frequency at each distance is not pleasant and we propose the following simplification

$$\frac{1}{Q(z, f)} = \frac{1}{Q(z)} R(f)$$

Then the attenuation exponent is

$$\gamma = -\frac{\omega T}{2Q_{\text{eff}}} R(f) \quad (10)$$

In other words, under this assumption we may still use constant T/Q_{eff} ratios and simply modulate the exponent with Solomon's relaxation function.

$$\gamma = -\frac{\omega T}{2Q_{\text{eff}}} \frac{\Delta\mu}{(1 - \Delta\mu)^{1/2}} \frac{\omega\tau}{1 + (\omega\tau)^2} \quad (11)$$

Here the dependence on $\Delta\mu$ becomes a scale factor on the ratio T/Q_{eff} . Since the last factor has a maximum value $1/2$ at $\omega\tau = 1$, we let the scale factor equal 2.0. Any other choice of scale factor is equivalent to changing the T/Q_{eff} ratio.

We will attempt to choose a Q function on the basis of observed spectra. In this choice, we require only that the spectrum exhibit some sort of corner beyond which the high frequency decay approaches $1/f^3$ dependence asymptotically. The choice of $1/f^3$ dependence agree with $m_s - m_b$ data and energy finiteness arguments. By specifying

that we see a $1/f^3$ dependence within the passbands of our instruments, we are assuming a moderately high to high rupture velocity.

Figure 4.7 shows a few representative modulations of the total frequency dependent anelastic attenuation factor as a function of the relaxation time, τ . Note that as τ increases, the peak of the relaxation function moves to lower frequencies, causing reduction in the amount of attenuation implied for higher frequencies. Indeed, if we plotted the curve for $\tau = 2$ sec, which Liu and Archambeau used, we would observe almost no attenuation at all. Their requirements were for modulation at very low frequencies, and their data had no resolution at periods less than 20 sec.

Figure 4.8 displays the effect of the relaxation modulation on the average P-wave spectrum for the Tien Shan event of February 2, 1969. At the top is the spectrum corrected with an unmodulated $T/Q_{\text{eff}} = 1.0$. For $\tau = 0.2$ sec, the short and long period decay rates are equal, giving a well defined corner at .1 Hz. For $0.2 < \tau$ the peak of the relaxation curve occurs at frequencies below .8 Hz, and the spectrum shows two distinct corners. That is, if a relaxation phenomenon with τ in this range controls the anelastic attenuation, then the true two-corner character of an earthquake spectrum would be masked by the transmission filter. As τ increases beyond 0.25, the corners on the spectrum slowly converge. At the same time, the spectrum approaches the station spectrum, and indeed the station spectrum has the desired $1/f^3$ slope. However, the amount of total attenuation predicted when τ is larger than 0.5 is unrealistically small at high frequencies. For the purposes of this report, we will chose $\tau = 0.3$ as the appropriate parameter for the relaxation model.

Further modelling is required to test the physical significance of this choice. We have chosen a T/Q_{eff} ratio which is constant with distance. This implies, of course, an increasing Q with depth. The modulation, however probably applies only to the asthenosphere because of the physics of the relaxation model, and is constant with distance only because all teleseismic body wave spend nearly the same time in the asthenosphere.

Solomon tested models with more than one relaxation peak, and the real Earth probably is a multiple relaxation medium. Additional tests will be run to relate the physical properties of the relaxations to the expected characteristics of our seismic source spectra.

Receiver Crust

Ben-Menahem, Smith and Teng (1965) implemented Haskell's layer matrix technique for six varied crustal models. Their computed vertical P-wave crustal amplitude responses show gains of 2.0 - 2.6 for all but one model (incident angles about 30° and incident waves in the period range 1 sec - 40 sec). Over a period range 1 - 100 sec, we can approximate the receiver crustal response by a gain of 2.3 with a maximum error of .7 at low frequencies which tend to see the layered system as a half space.

A refinement which should be considered for this study is application of receiver crustal corrections for each station. The result of Ben-Menahem et al. show that the various crustal models tested give similar responses for periods greater than 10 sec but that the high frequency responses vary. Since such corrections are not available, we apply a straight-line correction and assume the average spectrum will not be distorted by individual errors.

Summary

We have found each of the corrections implied by equation B1 to be complicated functions of various combinations of the parameters epicentral distance, source depth, station azimuth, the Earth's velocity and Q structures, and frequency.

We determined that the source crust tends to increase the long period level of the spectrum but that the interference of various waveforms could not be undone for the spectrum as a whole. The source crustal response also depends upon orientation of the focal mechanism, and our inability to correct for crustal response means that we also cannot correct for radiation pattern because the various contributions do not always come from similar radiation patterns. Rather than compute an intricate and perhaps wrong correction factor, we hope to minimize the maximum error by setting $C_s(i, \omega) = 1 = R(0) = 1$ and averaging over several stations. The average over a perfectly sampled radiation pattern, however gives .494 for P or .593 for S . Thus we divide the average P or S wave spectra by the appropriate number on the assumption that our average value is lower than the maximum of the dominant radiation pattern.

The geometric attenuation, or spreading correction given by Duda was chosen. A typical value for epicentral distance of 45° is $(\sim 5 \times 10^6)$. The anelastic attenuation turns out to be a difficult function to estimate from the spectra themselves. We examined a relaxation modulation on a constant T/Q_{eff} ratio and decided that $\tau = 0.3$ sec was an appropriate relaxation time. Whatever the model, the correction at low frequencies is always near 1.2.

Finally we examined the receiver crustal response and assumed an average gain of 2.3 for the vertical component of the P waves and 2.5 for SH curves.

Then at the long periods appropriate for estimating seismic moment, the total correction is of the order of the geometric attenuation correction ($\sim 5 \times 10^6$), with the other corrections dividing out. At high frequencies, the Q correction adds a factor of up to 20 (for P waves) to the gain which must be applied to the station spectrum to get a source spectrum.

References

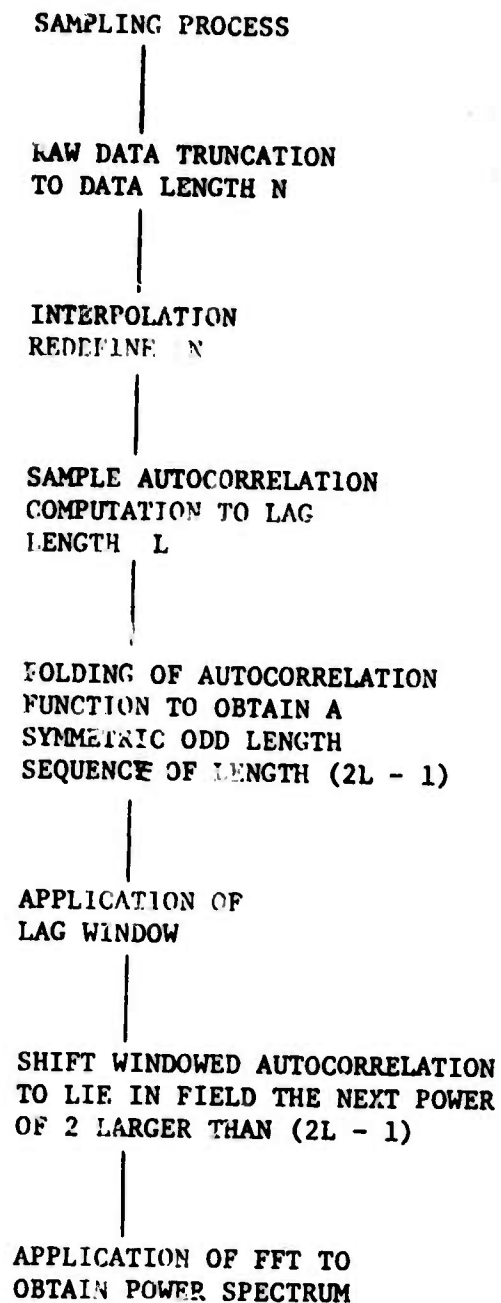
- Anderson, D. L., Ben-Menahem, A., and Archambeau, C. B. (1965). Attenuation of seismic energy in the upper mantle, J. Geophys. Res., 70, 1441-1448.
- Ben-Menahem, A., Smith, S. W., and Teng, T. L. (1965). A procedure for source studies from spectrums of long-period seismic body waves, Bull. Seism. Soc. Am., 55, 203-235.
- Duda, S. J. (1971). Travel times and body wave magnitude, Pure and Applied Geophysics, 87, 13-27.
- Gutenberg, B., and Richter, C. F. (1956). Earthquake magnitude, intensity, energy, and acceleration, Bull. Seism. Soc. Am., 46, 105-143.
- Herrmann, R. B. (1975). Source characteristics from long period P-wave observations, Semi-Annual Technical Report No. 1, ARPA Order No. 1827.
- Liu, H. P. and Archambeau, C. B. (1975). The effect of anelasticity on periods of the Earth's free oscillations (Toroidal modes), Geophys. J. Roy. Astron. Soc., in press.
- Nuttli, O. W. (1972). The amplitudes of teleseismic P waves, Bull. Seism. Soc. Am., 67, 343-356.
- Nuttli, O. W. (1973). Seismic wave attenuation and magnitude relation for eastern North America, J. Geophys. Res., 78, 876-885.
- Solomon, S. C. (1971). Seismic-Wave Attenuation and the State of the Upper Mantle, Ph.D. Thesis, Massachusetts Institute of Technology.
- Tsai, Y. B. and Aki, K. (1969). Simultaneous determination of seismic moment and attenuation of seismic surface waves, Bull. Seism. Soc. Am., 59, 275-287.

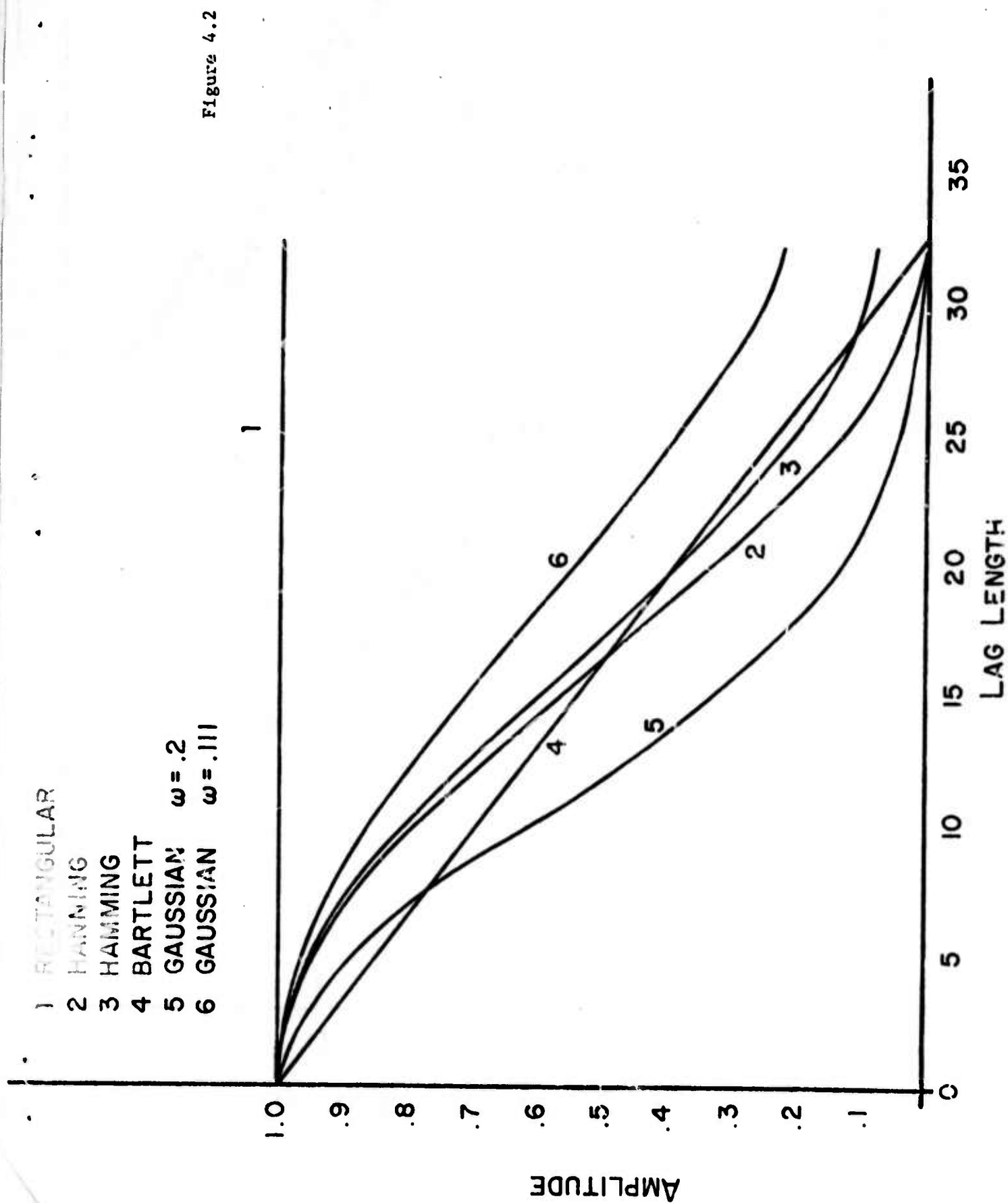
FIGURE CAPTIONS

- Figure 4.1: General flow diagram for autospectral estimation of seismogram spectra.
- Figure 4.2: Autocorrelation lag windows. Curve 1 is the rectangular window; 2 is a Hanning window; 3 is a Hamming window; 4 is a Bartlett window; 5 is a Gaussian window with $\omega = 0.2$; and 6 is another Gaussian window with $\omega = 0.111$.
- Figure 4.3: Average autopowerspectral levels compared to the periodogram for BAG SPZ (top) and BAG LPZ (bottom).
- Figure 4.4: Window closing experiment for BAG SPZ. The number of lags varies from 5% of sequence length at the bottom to 25% at the top. The Fourier amplitude spectrum estimated by direct application of the FFT algorithm is shown at the top for comparison.
- Figure 4.5: Window closing experiment for BAG LPZ. The number of lags varies from 10% of sequences length at the bottom to 50% of sequence length at the top. The Fourier amplitude spectrum estimated by direct application of an FFT algorithm is shown at the top for comparison.
- Figure 4.6: Shapes and relative amplitudes of the four waves which contribute to the teleseismic P wave from a crustal source. The station is at 45° distance, 40° relative azimuth from a vertical strike-slip source with due North slip at 20 km depth in a 30 km thick crust.
- Figure 4.7: Total P-wave anelastic attenuation. The highest attenuation is given by an unmodulated constant T/Q_{eff} ratio. The modulated attenuation curves are tangent to the unmodulated curve at the relaxation frequency.

Figure 4.8: Average P-wave source spectra corrected with various Q models: top curve corrected by constant T/Q_{eff} ratio; other curves corrected by a relaxation model.

Figure 4.1





LOG SMOOTHED SEISMOGRAM POWER SPECTRAL ESTIMATE

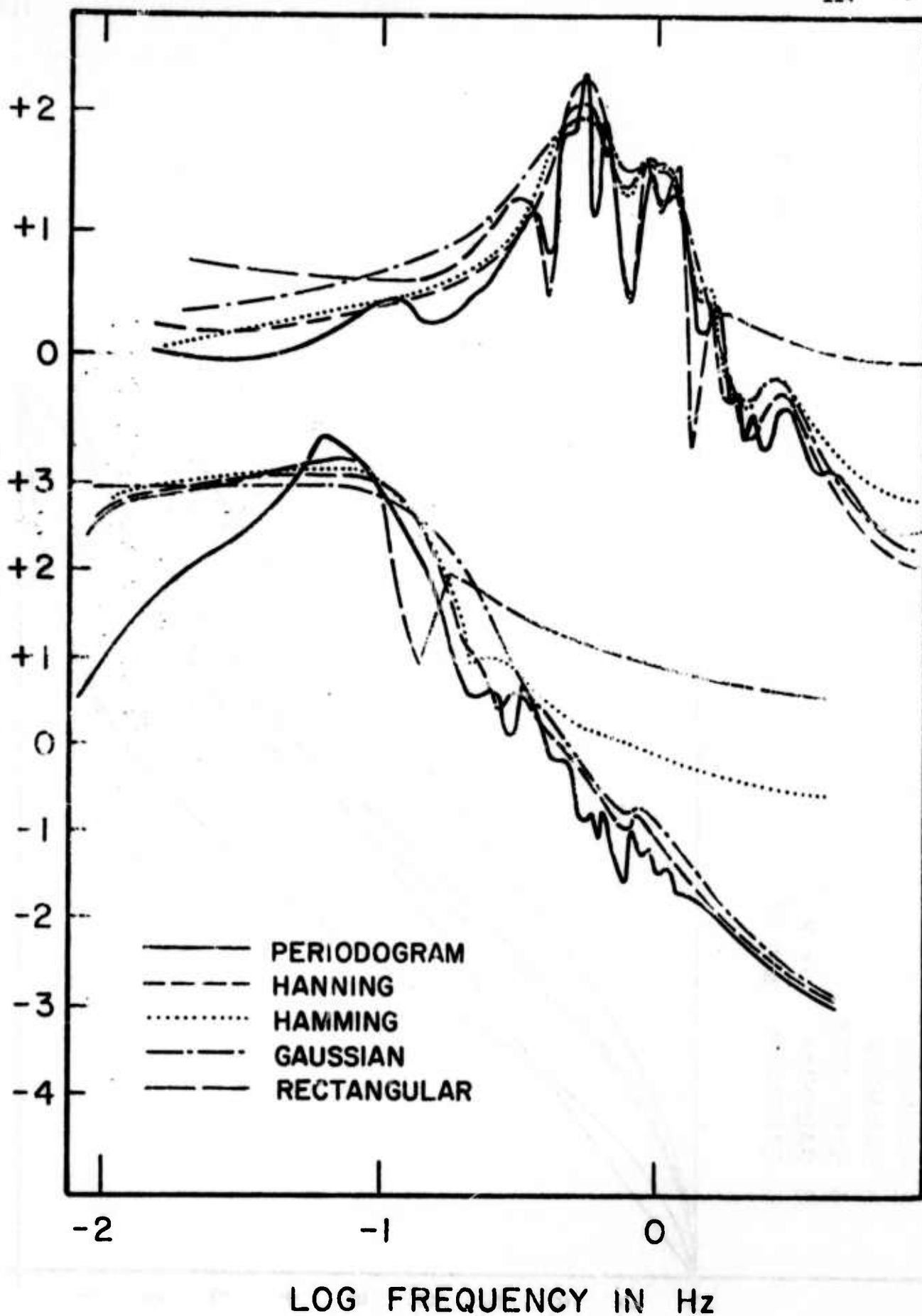


Figure 4.3

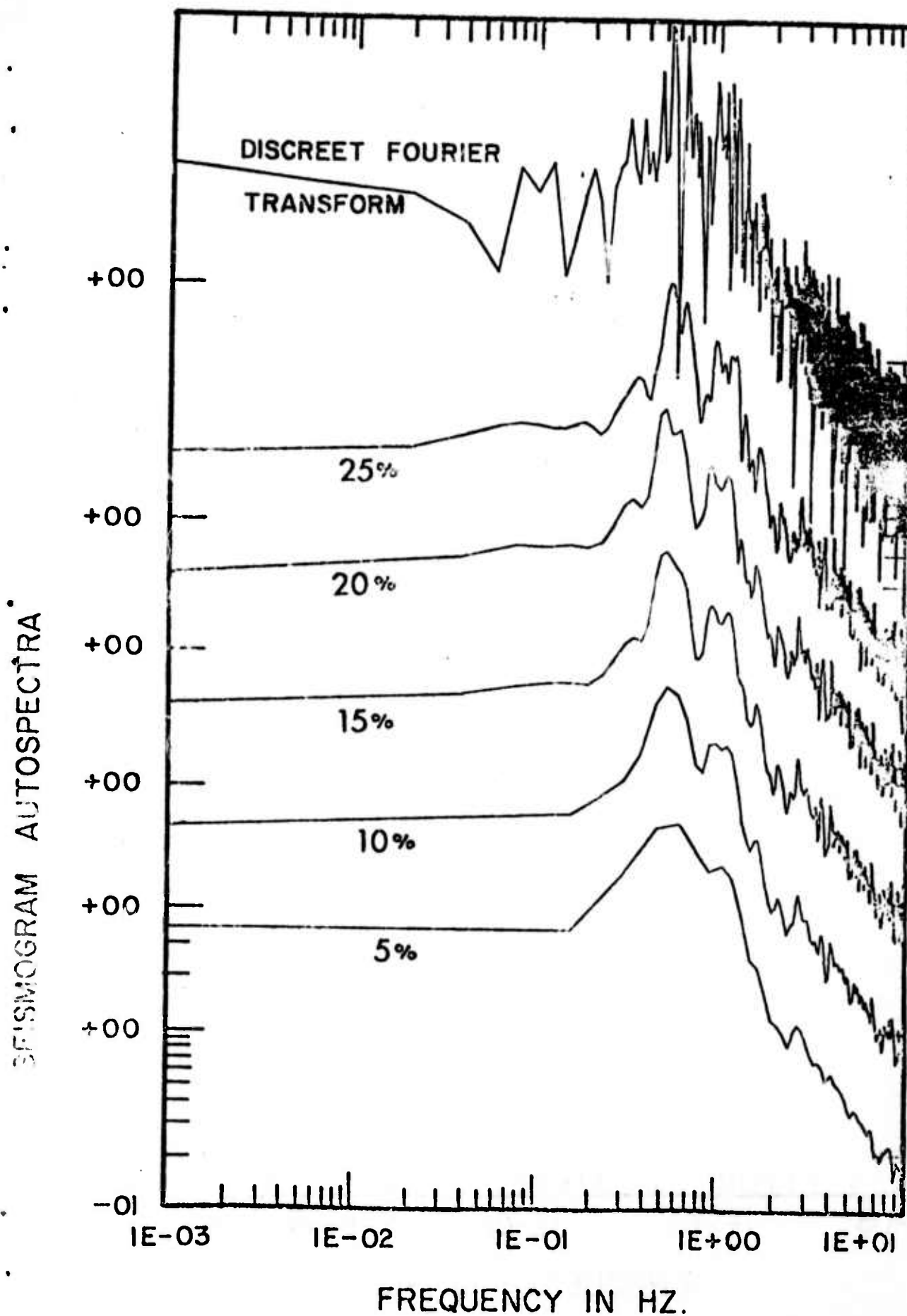


Figure 4.4

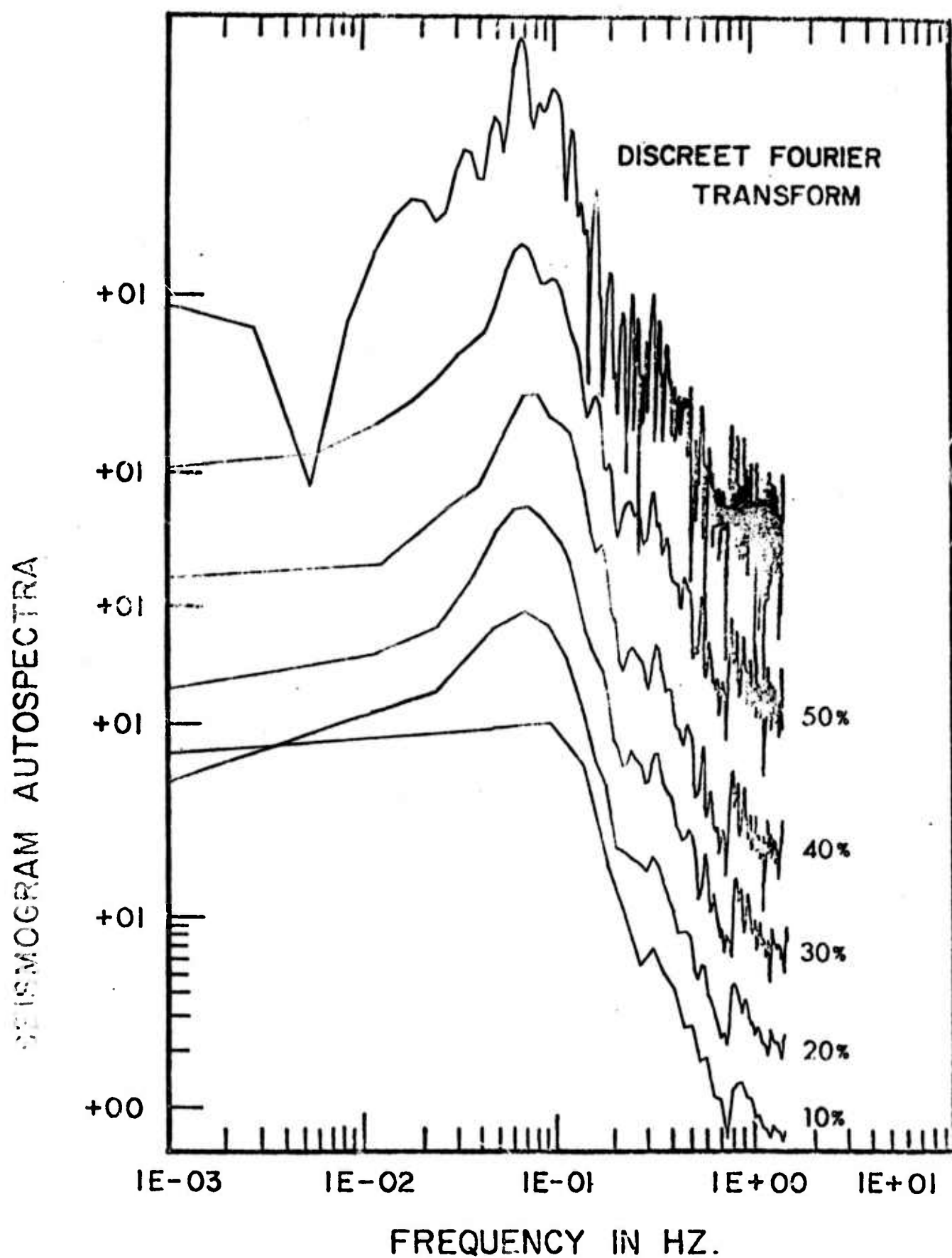


Figure 4.5

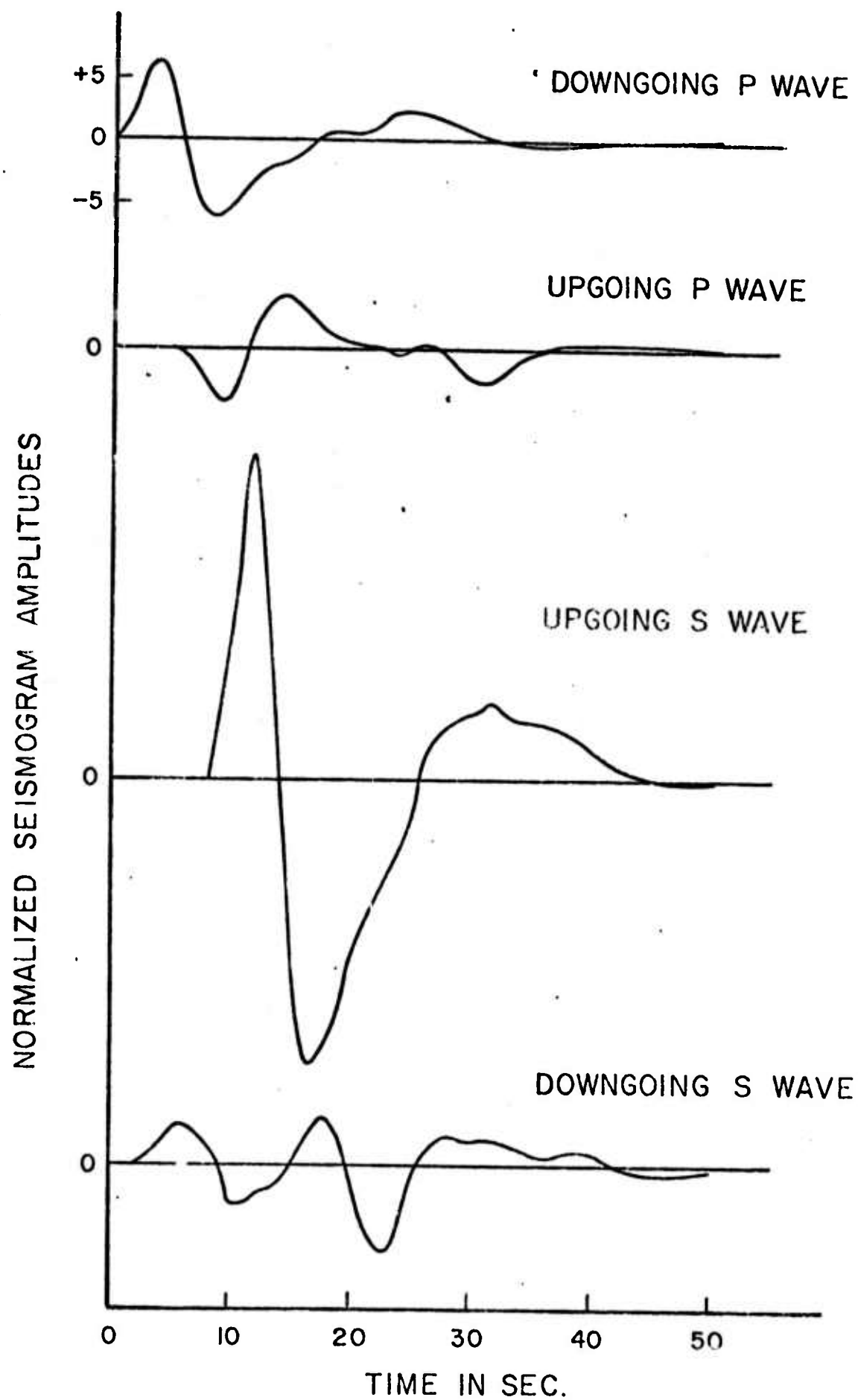


Figure 4.6

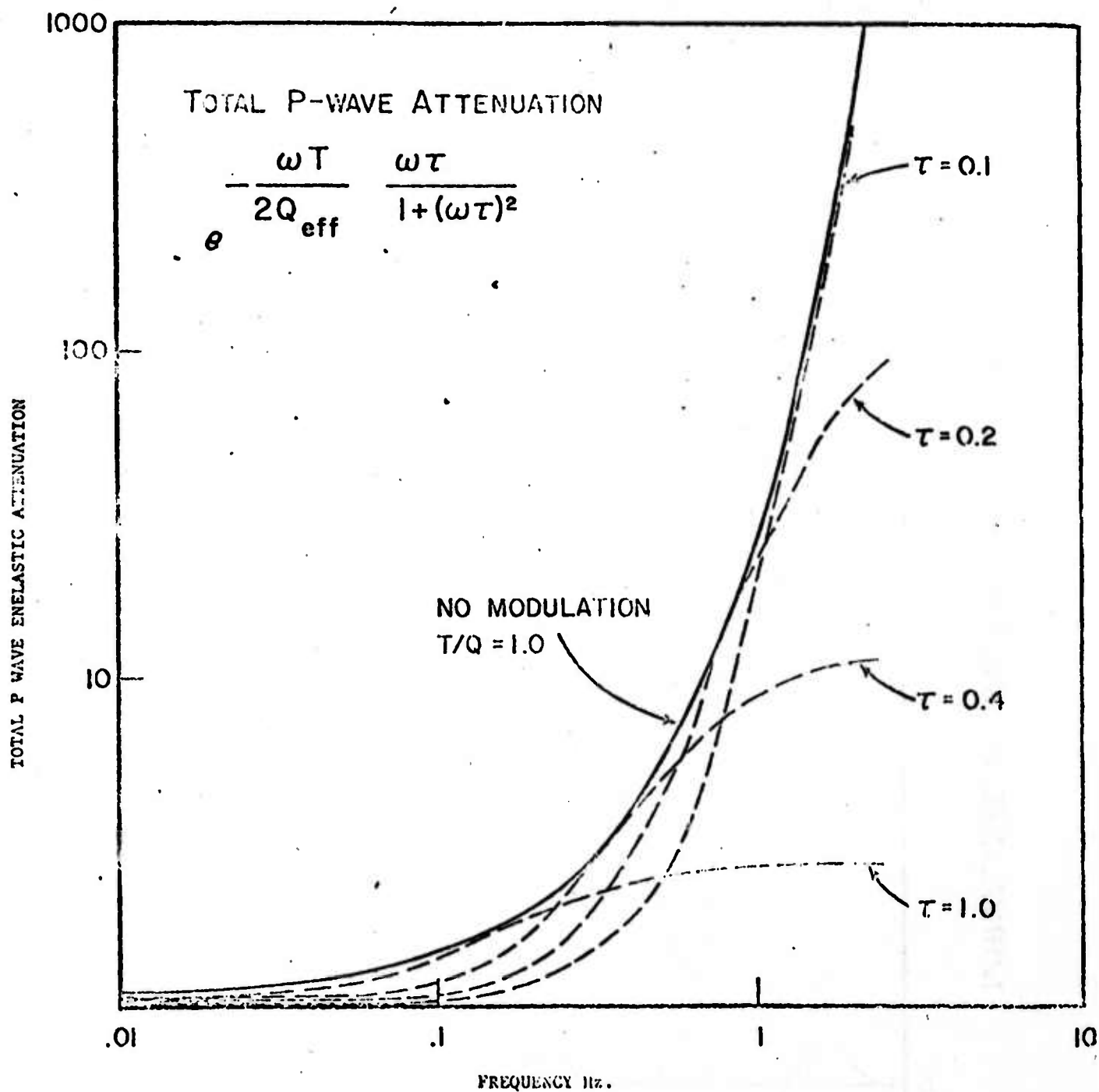


Figure 4.7

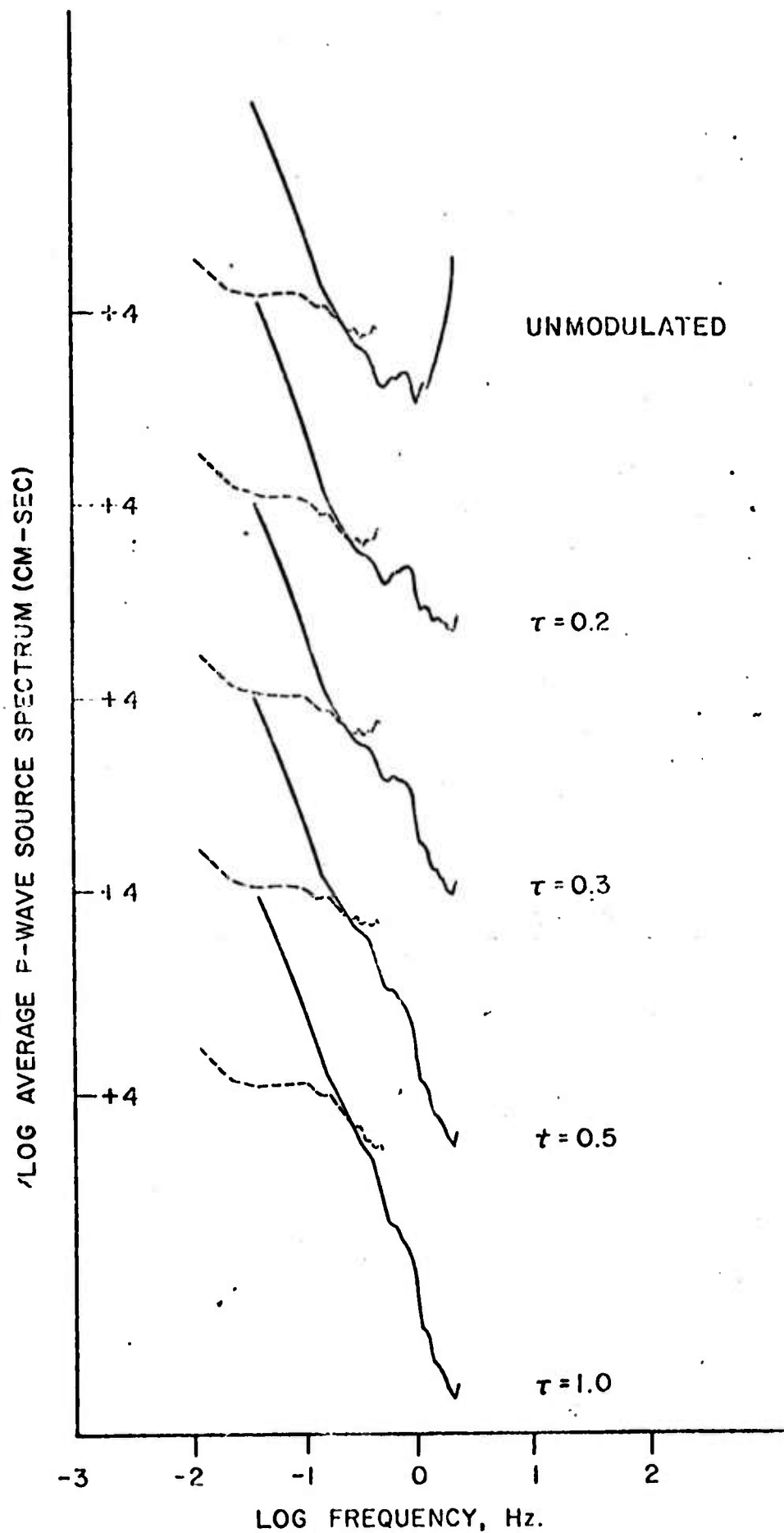


Figure 4.8

5. Rupture Velocity and Radiation Efficiency

Moujahed I. Hussein and M. J. Randall

ABSTRACT

If the specific fracture energy associated with an earthquake rupture is non-zero, then the rupture velocity cannot exceed the Rayleigh wave velocity, C_R , for the inplane shear mode of extension or the shear wave velocity, β , for the antiplane shear mode of extension. The radiation efficiency, η_R , which is the fraction of the available energy that is radiated, depends on the rupture history. The radiation efficiency is zero if the crack grows quasi-statically and improves with increasing rupture velocity. The radiation efficiency approaches unity if the rupture runs at C_R for the inplane shear mode and at β for the antiplane shear mode.

If a semi-infinite, antiplane shear crack tip accelerates rapidly to a terminal velocity v and runs at this velocity until it is arrested abruptly by a fracture energy barrier, then the specific surface energy γ_0 (ergs cm^{-2}) will be,

$$\gamma_0 = \frac{LT_0^2}{\mu\pi} \sqrt{\frac{\beta - v}{\beta + v}}$$

where L is the length of the rupture (cm), T_0 is the traction (dyne cm^{-2}) and μ is the rigidity of the material (dyne cm^{-2}). Thus the formula for the specific fracture energy, associated with the "seismic gap" model of fracture arrest (Hussein et al., 1975)

$$\gamma_0 = \frac{LT_0^2}{2\mu\pi}$$

will still be valid (to within a factor of two for v/β between 0^+ and 0.9) regardless of the arrest mechanism.

Submitted to the Bulletin of the Seismological Society of America.